

**Alma Mater Studiorum – Università di Bologna**

**DOTTORATO DI RICERCA IN  
MECCANICA E SCIENZE AVANZATE DELL'INGEGNERIA**

**Ciclo 34**

**Settore Concorsuale:** 09/A1 - INGEGNERIA AERONAUTICA, AEROSPAZIALE E NAVALE

**Settore Scientifico Disciplinare:** ING-IND/05 - IMPIANTI E SISTEMI AEROSPAZIALI

**SIMULATION OF OPTICAL OBSERVABLES FOR  
SPACE MISSIONS TO SMALL BODIES**

**Presentata da:** Francesco Fiori

**Coordinatore dottorato**

Lorenzo Donati

**Supervisore**

Paolo Tortora

**Co-supervisore**

Marco Zannoni

**Esame finale anno 2023**



# Abstract

## **Introduction and purpose**

The navigation of deep space spacecraft is characterized by many challenging problems, such as the accurate measurement of the probe’s state in terms of position and velocity with respect to Earth and to the bodies these missions are targeting, such as planets, satellites, comets, or asteroids. Nowadays, many radiometric techniques are available for this purpose, such as ranging, Doppler, and Delta-DOR, which are capable to assess the state of the spacecraft with good accuracy even at very large distances. However, when targeting a far object whose ephemerides are known with little accuracy, other observables are required to properly reduce the uncertainty in the relative position and attitude of the target body and the spacecraft. Typically, the measurements used for this purpose are the optical observables, which are extracted from the processing of images collected by the onboard cameras. Other than for navigation, optical observables can provide information about the characteristics of the target bodies for scientific analysis. In this study, we analyze the effect that simulated optical observables have on the expected performance of the orbit determination problem in the case of the ESA’s Hera mission. To this extent, many observables are fed to an ad-hoc dynamical model, and a certain number of solve-for parameters are estimated based on the availability and overall quality of the input measurements. The noise introduced in the output optical observables by the image processing is quantified and used as a metric to assess the quality of the considered observables.

## **Case study: the Hera mission**

Hera is an ESA mission that is meant to be launched in 2024, aiming to study the binary asteroid system of Didymos and Dimorphos. In September 2022, the NASA’s mission DART was intentionally crashed onto the surface of Dimorphos, the smallest of the two asteroids, to assess the feasibility of an innovative planetary defence technique called “kinetic impactor”, which consists in transferring momentum from the spacecraft to the target small body to deviate its trajectory. The Hera mission will study the precise effects that the impact of DART had on the trajectories of the system, while collecting precious information about the geomorphology of the asteroids.

## **Optical observables simulation method**

Typically, optical observables are the pixel sample and line coordinates of a landmark, which is a specific feature on the surface of a body. A standard approach when using optical observables within orbit determination simulations consists in using white gaussian noise with a fixed standard deviation for the observed (simulated) sample and line measurements. However, during the real mission, the optical observables extracted from pictures are often subject to biases and correlated error sources, which may affect the accuracy of the estimated parameters of the system. Therefore, for this study we adapted the full pipeline that was used for the navigation of the Rosetta spacecraft, another ESA mission towards a comet, from which we generate the optical observables in a way that is much closer to reality. The process starts with the creation of the images captured by the onboard camera, computed by means of a shape model and a photometric function. Then, using a stereophotoclinometry technique on the simulated images, we create a series of maplets, which represent the reconstructed 3D geometry of the regions around the landmarks. These maplets allow for the extraction of the pixel positions of the landmarks (the sample and line coordinates) by matching them to the original images taken from the onboard camera after applying a photometric model and a reprojection. In this way, the whole pipeline introduces naturally the image processing noise, which is present even in the simplest case, without applying any other error source to them.

## **Data selection and orbit determination**

The quality of the extracted optical observables, also called observed observables, is affected by many variables inherent to the method used for the extraction process. In the specific case of the maplets, the parameters which are considered having an effect during the maplet matching are the maplet dimension, the correlation value of a maplet with its corresponding reprojected region in the picture, and the occupation factor, related to the amount of good quality pixels available for the correlation step. All these parameters affect the final quality of the observables and their total number, which is correlated to the processing time. Therefore, we perform a sensitivity analysis to evaluate how these parameters affect the quality of the orbit determination solution. The observed observables are fed to the orbit determination setup, to quantify the noise introduced by the image processing pipeline and to assess how reliable the stereophotoclinometry and maplet matching method is with the considered parameters. The metrics used for quantification of the noise are expressed as the root mean square of the residuals, which are the differences between the observed observables with the computed observables, corresponding to the ground truth. Thanks to this metric, the parameters can be fine-tuned to find a sweet spot in terms of number of outliers and overall standard deviation of the residuals, so that we can find the best compromise in terms of residual error. In particular, the results show that the best parameters are related to small maplets (since they have a higher

resolution with respect to larger ones), when the maplet matching correlation coefficient and occupation factor are really high.



# Acknowledgements

I would like to express my gratitude to my advisors Paolo Tortora and co-advisor Marco Zannoni, for helping me along this path and mostly for the beautiful environment which they have slowly built in the past years within the Radio Science and Planetary Exploration Laboratory, in a continuous effort of providing great opportunities for all the people that orbited around the Lab. I express my gratitude to the reviewers, Dustin R. Buccino and Fabio Ferrari, who provided useful suggestions to improve the quality of this work. Another thank goes to all the people involved, such as Klaas Vantournhout, who patiently and continuously helped me, and the other people from the FD Team at ESOC whom unfortunately I could meet only *en passant* and remotely (David Antal-Wokes, Pedro Santana Camprubi, Sabine Kielbassa, Ulrich Herfort, Vicente Companys). I would also like to thank Riccardo Lasagni Manghi and Edoardo Gramigna, for the huge help provided, together with all the people who are part of the different research teams in the Tecnopolo/CIRI Aeronautica facility, who have always demonstrated great inclusiveness and friendship in the joyful and difficult moments during these years spent together. I finally thank my parents, for always being supportive, my friends that during these years shared part of their life with me, together with all the people that supported me.

*A single sunbeam is enough to drive away many shadows.*



# Contents

<b>Acronyms</b>	<b>ix</b>
<b>1 Introduction</b>	<b>1</b>
1.1 The Orbit Determination Problem . . . . .	4
1.2 Observable types . . . . .	8
1.2.1 Radiometric observables . . . . .	9
1.2.2 Optical observables . . . . .	12
1.2.3 Noise sources . . . . .	13
1.3 The Hera Mission . . . . .	15
1.3.1 The spacecraft . . . . .	18
1.3.2 Mission timeline overview . . . . .	19
1.3.3 Hera Radio Science Experiment . . . . .	20
1.3.4 Hera Asteroid Framing Camera . . . . .	20
1.4 The Dynamical model . . . . .	21
1.4.1 Reference frames . . . . .	22
1.4.2 Asteroid's rotational models . . . . .	23
1.4.3 Gravitational accelerations . . . . .	25
1.4.4 Non-gravitational accelerations . . . . .	25
<b>2 Optical observables generation</b>	<b>29</b>
2.1 Landmarks selection . . . . .	31
2.2 Images simulation . . . . .	38
2.2.1 Timeline extraction . . . . .	40
2.2.2 Photometric model . . . . .	46
2.2.3 Simulation output . . . . .	50
2.3 Maplets creation . . . . .	51
2.3.1 Visibility constraints . . . . .	53
2.3.2 Maplet initialization . . . . .	63
2.3.3 Image rectification . . . . .	63
2.3.4 Slopes estimation . . . . .	65
2.3.5 Height constraints . . . . .	67

2.3.6	Height integration . . . . .	68
2.4	Observables extraction through maplet matching . . . . .	70
<b>3</b>	<b>Results</b>	<b>75</b>
3.1	Maplet dimension . . . . .	77
3.2	Maplet matching minimum correlation . . . . .	83
3.3	Maplet matching minimum occupation . . . . .	88
<b>4</b>	<b>Conclusions</b>	<b>93</b>
	<b>Appendix</b>	<b>97</b>
	Residuals at different maplet dimensions . . . . .	97
	Camera distances and maplet dimensions . . . . .	102
	Residuals at different minimum correlation for maplet matching . . . . .	108
	Residuals at different minimum occupation for maplet matching . . . . .	113
	<b>Open-source software used</b>	<b>117</b>
	<b>List of Figures</b>	<b>122</b>
	<b>List of Tables</b>	<b>123</b>
	<b>Bibliography</b>	<b>134</b>

# Acronyms

AFC	Asteroid Framing Camera
AIDA	Asteroid Impact and Deflection Assessment
AIM	Asteroid Impact Mission
BRIEF	Binary Robust Independent Elementary Features
BRISK	Binary Robust Invariant Scalable Keypoints
C/A	Closest Approach
CMOS	Complementary Metal Oxide Semiconductor
CONOPS	Concept Of Operations
DART	Double Asteroid Redirection Test
Delta-DOR	Delta Differential One-way Ranging
DRM	Didymos Reference Model
DU	Digital Units
EME	Earth Mean Equator
EMO	Earth Mean Orbit
ESA	European Space Agency
ETTR	Expose To The Right
ET	Ephemeris Time
FITS	Flexible Image Transport System
FOV	Field Of View
HGA	High-Gain Antenna
IFOV	Instantaneous Field Of View
ISL	Inter-satellite Link
JPL	Jet Propulsion Laboratory
LIDAR	Light Detection And Ranging
LGA	Low-Gain Antenna
LOS	Line Of Sight
MONTE	Mission-analysis and Operations Navigation Toolkit Environment
NASA	National Aeronautics and Space Administration

continued on next page

continued from previous page

NAC	Narrow Angle Camera
NEA	Near-Earth Asteroid
NEO	Near-Earth Object
OD	Orbit Determination
ORB	Oriented FAST and Rotated BRIEF
OWLT	One-Way Light Time
PHA	Potentially Hazardous Asteroid
RMS	Root Mean Square
RU	Range Unit
RTLT	Round-Trip Light Time
S/C	Spacecraft
SD	Standard Deviation
SIFT	Scale-Invariant Feature Transform
SNR	Signal-to-Noise Ratio
SRP	Solar Radiation Pressure
SURF	Speeded-Up Robust Features
SVD	Singular Value Decomposition
VLBI	Very Long Baseline Interferometry

# Chapter 1

## Introduction

The Hera mission [1] is composed of a main spacecraft and two CubeSats, Juventas and Milani. Considering the current schedule, it will be launched in 2024, aiming to reach the binary asteroid system composed of Didymos and Dimorphos at the beginning of 2027. Prior to this mission, NASA's Double Asteroid Redirection Test (DART) spacecraft intentionally impacted with the secondary body, Dimorphos, to validate a planetary defense technique called *kinetic impactor* (KI), related to the momentum transfer to deflect a small body. This maneuver led to a change in the momentum of Dimorphos, whose value is required to be assessed with higher accuracy with respect to what can be achieved from ground-based measurements only. Therefore, the Hera mission will provide a detailed characterization of the aftermath of the DART impact. At the same time, it will collect precious information about the geomorphology of the asteroids, their inner structure, gravity field, and surface characteristics.

The navigation in deep space requires accurate measurements of the spacecraft's state and of the bodies these missions are targeting, such as planets, satellites, comets, or asteroids. In addition to the classical radiometric techniques, such as ranging, Doppler and Delta-Differential One-way Ranging (DOR), which can assess the state of the spacecraft with good accuracy even at very large distances, optical observables can also be used. These provide crucial information about the relative trajectory and attitude between the spacecraft and far objects, whose ephemerides are known with little accuracy.

The aim of this thesis is to **simulate realistic optical observables** in the orbit determination (OD) process within ESA's Hera mission, to provide better insight about the estimation of parameters of the Didymos binary asteroid system in an OD solution and to generally improve the fidelity of the OD simulations.

The core piece of information that an optical observable provides is the inertial direction from the camera to a generic element, such as a star, the centroid of a body or the position of a given surface feature [2], thus requiring different image processing techniques depending on the observed target. When an object is small in the field of view, such that

its dimension on the camera sensor frame is in the order of a few pixels, it is possible to extract an observable related to its center of brightness. For example, the star trackers use centroiding algorithms (such as fitting of gaussians) to provide attitude information by comparing a slightly defocused picture of stars with an accurate stellar database. A similar approach may be used during the far approach of planets, asteroids, or comets, where optical observables can be extracted even when the reprojections of the targets are as small as one pixel [3]. When the target appears larger in the field of view, the overall shape can be addressed. Considering ellipsoidal-shaped bodies, it is possible to estimate the shape's center of figure [4] through level of brightness of the images [5], [6], or by using the terminator line and the best fit of limb pixels through an ellipsoidal shape [7], [8].

However, these techniques are not providing the best knowledge that a single picture taken at a closer distance contains, where it is possible to use features for navigation. The tracking of features may be based on crater detection through image processing of edges [9], [10], or on generic elements between subsequent frames using algorithms such as Scale-Invariant Feature Transform (SIFT [11]), Speeded-Up Robust Features (SURF [12]), or other related descriptors such as Binary Robust Independent Elementary Features (BRIEF [13]), Oriented FAST and Rotated BRIEF (ORB [14]), Binary Robust Invariant Scalable Keypoints (BRISK [15]). In more modern solutions, also artificial intelligence is used for the recognition of craters on top of the target's surface [16].

In the Hera case, the rapidly changing illumination conditions and the extreme contrast of the asteroids provide features that are difficult to be tracked with these types of descriptors. For our purposes, a method based on the geometry extraction of the asteroids' surface from multiple images with different shading information was selected, providing a robust pipeline when the simple feature extraction algorithms would fail. The optical observables are extracted from images captured by the Hera cameras, and they consist of pixel coordinates (in terms of sample and line) of a target feature of the framed body, which we will call landmark from now on. These optical observables can be simulated as the expected sample and line positions of the considered landmark, by means of an observational model comprising of a function which converts a pixel direction to a direction in the body fixed frame of the camera.

To these simulated values, it is possible to add controlled noise sources, thus providing the final simulated version of the optical observables with added noise. However, since this procedure lacks all the image capturing and processing pipeline, the observables are not necessarily fully adherent to reality.

To provide a more accurate reproduction of the real pipeline, starting from the moment a picture is captured by the spacecraft camera up to the measure of the sample and line of a landmark, a full setup which comprises image simulation and observable extraction is required. To this extent, we will adapt the code used for Rosetta, an ESA mission towards the comet 67P / Churyumov-Gerasimenko, to the case of the Hera mission. At the be-

gining of the process, images will be simulated considering a photometric model applied to the high-resolution polyhedral model of our target, Didymos. The created image files have similar characteristics of real mission products, both in terms of data content (as geometric reprojection of the Didymos model on the camera sensor) and structure (as realistic values of bit depth and brightness values). In this way a database of pictures related to the entire mission can be created.

The images with the desired landmarks can be selected from this database, and then processed to extract the final optical observables. The method used is a stereophotoclinometry technique, which exploits differently lit images of the same region to create a matrix of heights that describes locally the surface of the body, which we call maplet. The maplets are then used as the basis for image correlation, whose output provides the sample and line positions of the landmark they are referring to.

Then, when all the optical observables are available, they are provided to the OD setup, which also uses other radiometric observables, to simulate a realistic scenario during the Hera mission. This OD step will provide quantitative information about the noise introduced by the image processing and tells how reliable the stereophotoclinometry is by changing the parameters that describe its performance, such as the correlation value, occupation factor and maplet dimension during the optical observable extraction from simulated images. In this analysis, the residuals, which are computed as the difference between the extracted observables and the ground truth, provide a quick indicator about the validity of the extracted observables, since they are created starting from the same dynamical model.

To this extent, a first introduction about the dynamical model used for the simulation is presented in chapter 1; then, the stereophotoclinometry technique used for the extraction of optical observables is described in chapter 2, starting from images that have been simulated; finally, the results of the analysis in terms of variation of the characteristic parameters of the stereophotoclinometry technique are presented in chapter 3.

## 1.1 The Orbit Determination Problem

The purpose of orbit determination (OD) is to estimate a set of physical parameters, which uniquely define the trajectory of the spacecraft and of target celestial bodies using as input the information provided by measurements collected by the spacecraft or from Earth observations.

The core method of OD is an iterative general-purpose estimation method for the values of unknown parameters (solve-for parameters), given a series of collected measurements. In a high-level description, the solution to the OD problem is found by properly processing the residuals, which are the difference between the measured observables (also called observed observables) and the computed observables, which are generated from an observation model, using the integrated spacecraft trajectories as input [17].

For the estimation of the solve-for parameters, the residuals are inserted in an iterative procedure (see Figure 1.1) of a minimization problem in a weighted linear least-squares sense [18], where the method provides a solution characterized by minimum residuals variance if the weights assigned to the measurements are the inverse of their error covariance. The computed correction to the state of the parameters is obtained from a linearized version of the dynamical model and it can be iterated up to convergence to a stable value. At the end of the process, a new estimated value of the multiple solve-for parameters is provided, together with a covariance matrix containing the values of the solution's formal uncertainty.

The dynamical model should be a replica of the universe in which the measured observables are collected. This means that it should contain all the forces and interactions expected to influence the dynamics of the considered bodies, together with the initial conditions for the propagation of the trajectories extracted from the best knowledge available at that time.

If the dynamical model is representative of the real world, the values of the computed observables generated from the mathematical model should match the observed ones with sufficient accuracy. In an ideal scenario in which the knowledge of the dynamical model is exact, the difference between the computed and observed measurements should be a pure gaussian white noise characterized by zero mean.

However, the gaussian distribution of residuals can be easily affected by many error sources, both in the external measurement part and in the internal mathematical model. In real-life scenarios, signatures in the residuals may appear, such as bias values, outliers, discontinuities or drifting of values, providing information about unconsidered effects or mismodelling.

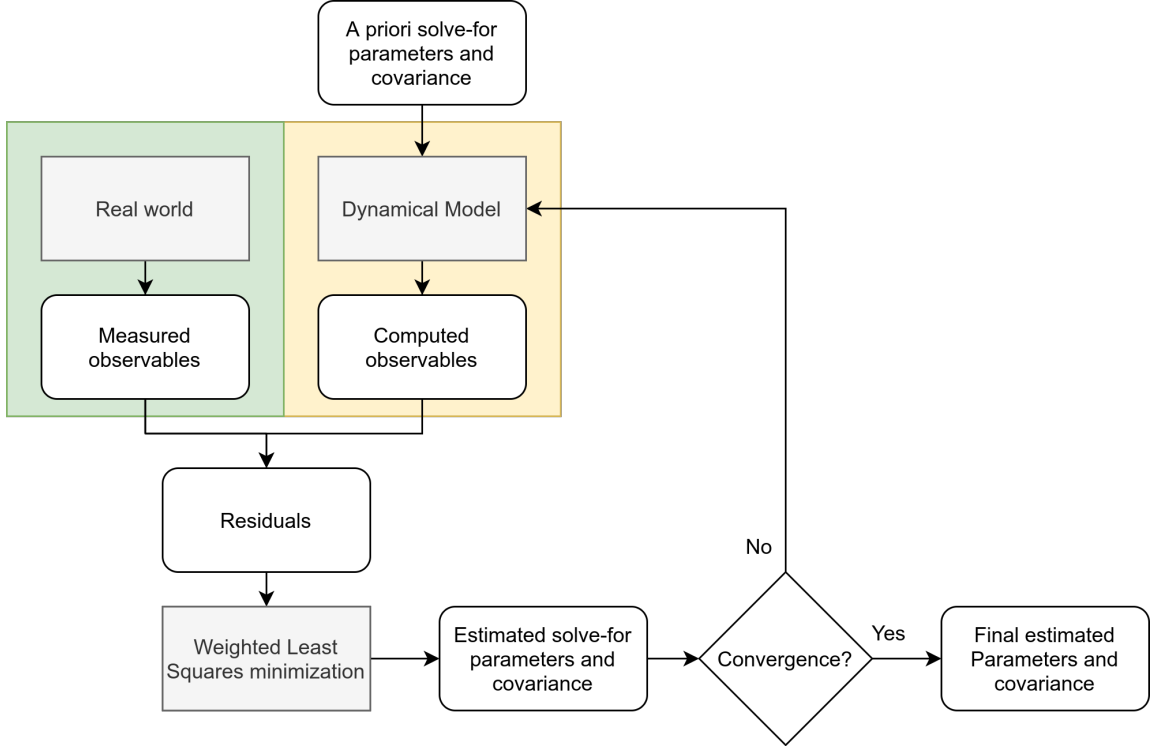


Figure 1.1: Iterative orbit determination process.

The OD problem can be mathematically described as the solution of the differential equation (1.1) shown below [19]. In this expression,  $\mathbf{x}$  represents an  $n \times 1$  vector of solve-for parameters, while the function  $f(\mathbf{x}, t)$  represents the non-linear dynamical model describing the system:

$$\begin{cases} \frac{d\mathbf{x}}{dt} = f(\mathbf{x}, t) \\ \mathbf{x}(t_0) = \mathbf{x}_0 \end{cases} \quad (1.1)$$

The measured observables are stored in a vector  $\mathbf{z}$  of size  $m \times 1$ , which may be mathematically described with an observable model that links the observables to the state vector  $\mathbf{x}$ :

$$\mathbf{z}_i = g_i(\mathbf{x}(t_i), t_i), \quad i \in [1, \dots, m] \quad (1.2)$$

All the measurements that provide even some indirect information linked to the parameters of the state vector are collected in the observable vector  $\mathbf{z}$ . In general, the measured observables  $\mathbf{z}$  may be the direct outcome of different types of sensors and instruments (for example, laser altimeters or accelerometers), or values derived from an adequate post-processing methodology of a raw measurement, such as the position of an object in a picture extracted with image processing techniques. The computed observables  $\hat{\mathbf{z}}$  are computed from the observable model, and they can be compared with the measured observables  $\mathbf{z}$ , with the purpose of minimizing the cost function described by their squared

difference:

$$J = \sum_{i=1}^m (\mathbf{z}_i - \hat{\mathbf{z}}_i)^2 \quad (1.3)$$

Where the residuals are found as the difference between measured and computed observables:

$$\delta \hat{\mathbf{z}} = \mathbf{z} - \hat{\mathbf{z}}(\hat{\mathbf{x}}) \quad (1.4)$$

It should be noted that an element of the vector  $\mathbf{z}$  may have expected residuals of different orders of magnitude with respect to the other elements of the same vector. Therefore, the cost function is weighted by an uncertainty value  $\sigma$  specific for each measurement type and equal to the standard deviation of its measurement noise. Considering the symmetric matrix of the observable weights:

$$W = \begin{bmatrix} 1/\sigma_{(1,1)0}^2 & \cdots & \\ \vdots & \ddots & \vdots \\ \cdots & \cdots & 1/\sigma_{(m,m)0}^2 \end{bmatrix} \quad (1.5)$$

We have:

$$J = \sum_{i=1}^m \left( \frac{\delta \hat{\mathbf{z}}_i}{\sigma_i} \right)^2 = (\mathbf{z} - \hat{\mathbf{z}}(\hat{\mathbf{x}})) \cdot W \cdot (\mathbf{z} - \hat{\mathbf{z}}(\hat{\mathbf{x}}))^T \quad (1.6)$$

To minimize the cost function, we take the derivative and set it equal to the zero vector:

$$\frac{\partial J}{\partial \hat{\mathbf{x}}} = 2 (\mathbf{z} - \hat{\mathbf{z}}(\hat{\mathbf{x}}))^T \cdot W \cdot \left( -\frac{\partial \hat{\mathbf{z}}(\hat{\mathbf{x}})}{\partial \hat{\mathbf{x}}} \right) = \mathbf{0} \quad (1.7)$$

Since  $W$  is symmetric,  $W = W^T$ , and considering the partial derivative matrix  $A(\hat{\mathbf{x}}) = \frac{\partial \hat{\mathbf{z}}(\hat{\mathbf{x}})}{\partial \hat{\mathbf{x}}}$ , we have:

$$G(\hat{\mathbf{x}}) = A^T \cdot W \cdot (\mathbf{z} - \hat{\mathbf{z}}(\hat{\mathbf{x}})) = \mathbf{0} \quad (1.8)$$

Which can be linearized around a first attempt value  $\hat{\mathbf{x}}_0$ :

$$G(\hat{\mathbf{x}}) \cong G(\hat{\mathbf{x}}_0) + \nabla G(\hat{\mathbf{x}} - \hat{\mathbf{x}}_0) = \mathbf{0} \quad (1.9)$$

So that we can obtain a differential correction for the attempt value:

$$\hat{\mathbf{x}} = \hat{\mathbf{x}}_0 - (\nabla G)^{-1} G(\hat{\mathbf{x}}_0) \quad (1.10)$$

This equation may be expressed in terms of the original partial derivative matrix, considering that:

$$\nabla G(\hat{\mathbf{x}}) = \frac{\partial G(\hat{\mathbf{x}})}{\partial \hat{\mathbf{x}}} = \frac{\partial A^T}{\partial \hat{\mathbf{x}}} \cdot W \cdot (\mathbf{z} - \hat{\mathbf{z}}(\hat{\mathbf{x}})) + A^T \cdot W \cdot (-A) \cong -A^T \cdot W \cdot A \quad (1.11)$$

Where the second order derivative was neglected. Since this is a part of an iterative procedure, neglecting this term will mainly affect the speed of convergence.

$$\hat{\mathbf{x}} = \hat{\mathbf{x}}_0 + (A_0^T \cdot W \cdot A_0)^{-1} A_0^T \cdot W \cdot (\mathbf{z} - \hat{\mathbf{z}}(\hat{\mathbf{x}}_0)) \quad (1.12)$$

Therefore, to minimize the cost function  $J$ , we need to iterate  $\mathbf{x}$  up to convergence, obtaining a new estimate state vector  $\hat{\mathbf{x}}$ , the new computed observables  $\hat{\mathbf{z}}$ , and new partial derivatives. The first part of the correction term is the covariance matrix  $P$ :

$$P_{\delta\mathbf{x}} = (A^T \cdot W \cdot A)^{-1} \quad (1.13)$$

Considering previous knowledge about the *a priori* sigma of the parameters to be estimated, the cost function may also be rewritten as:

$$J = \sum_{i=1}^m \frac{\delta\hat{\mathbf{z}}_i^2}{\sigma_i^2} + \sum_{j=1}^n \frac{(\hat{\mathbf{x}}_j - \hat{\mathbf{x}}_{j0})^2}{\sigma_{j0}^2} \quad (1.14)$$

This description has the advantage of better constraining the estimated sigma value, since it provides to the cost a distance with respect to the initial condition. If considering a new set of elements, such as:

$$\mathbf{z}' = \begin{pmatrix} \mathbf{z} \\ \mathbf{x}_0 \end{pmatrix}, \quad W' = \begin{pmatrix} W & \mathbf{0} \\ \mathbf{0} & P_0^{-1} \end{pmatrix}, \quad A' = \begin{pmatrix} A \\ I \end{pmatrix} \quad (1.15)$$

Where  $P_0$ :

$$P_0 = \begin{bmatrix} \sigma_{(1,1)0}^2 & \cdots & \\ \vdots & \ddots & \vdots \\ & \cdots & \sigma_{(n,n)0}^2 \end{bmatrix} \quad (1.16)$$

It can be demonstrated with analogous calculations that the new correction term may be written as:

$$P'_{\delta\mathbf{x}} = (A'^T \cdot W' \cdot A' + P_0^{-1})^{-1} \quad (1.17)$$

Which contains information about the formal uncertainty and the correlation among the solve-for parameters. Specifically, the diagonal terms represent the square of the uncertainty for the individual solve-for parameters, while the off-diagonal elements are the covariances of the mixed parameters:

$$P_{\delta x}(i, j) : \begin{cases} \sigma_i & \text{if } i = j \\ \rho_{i,j} \sigma_i \sigma_j & \text{if } i \neq j \end{cases} \quad (1.18)$$

Where  $\rho_{i,j}$  is the cross-correlation coefficient for the parameters. It can be noted that the formal uncertainty is affected by multiple error sources, related to the *a priori* values

for the weights adopted, the presence of non-gaussian noise, and errors in the model. Depending on the *a priori* knowledge about the expected noise, it is possible to provide conservative assumptions about the process noise covariance to obtain valid results.

In our particular case, the OD provides an analysis of the expected noise levels, the maximum achievable accuracy, and general predictions of the scenarios that the mission will encounter during its lifespan, such as how the optical observables affect the estimation of the parameters introduced in the dynamical model. To this extent, we need to introduce into the dynamical model of the estimation process all the elements that have an effect on the system. Among all, we can find spherical harmonics of the gravity field of the involved bodies, and external forces, like solar radiation pressure (SRP).

## 1.2 Observable types

An observable is everything that can provide any direct or indirect information about the solve-for parameters considered in the dynamical system. In the case of a generic spacecraft in deep space, different types of measured observables can be collected from onboard instruments but also from external sources, mostly obtained from ground station observations. Information about the distance from other bodies can be directly provided from instruments such as light detection and ranging laser altimeters (LIDAR) [20], radar altimeters [21], or indirectly from pictures collected by navigation or scientific cameras; non-gravitational forces may be measured thanks to onboard accelerometers [22]. To date, the most widely used measurements to estimate the position and velocity of deep-space spacecraft are the so-called radiometric measurements [23], which involve the transmission of microwave carrier signals from the spacecraft to ground stations on Earth. These include:

- **Range**, which provides the one-way light time (OWLT) or round-trip light time (RTLTL) related to the time of flight of a signal. It may be in different configurations which have the spacecraft as transmitter and another station as receiver (one-way), the ground station as transmitter and receiver, while the spacecraft is sending back the incoming signal, usually at a scaled frequency reference (two-way), and a modified two-way version where the signal sent back from the spacecraft is collected from a different station (three-way).
- **Range-rate (or Doppler)**, which is related to the frequency shift of the carrier signal between transmission and reception, and which provides information about the relative velocity of the spacecraft in the line-of-sight of the transmitter/receiver.
- **Delta-Differential One-way Ranging ( $\Delta$ DOR)**, which gives information about

the angle of an incoming spacecraft signal, expressed in local right ascension and declination. It requires at least two widely separated receivers to achieve acceptable accuracy (one-way only).

To this list of radiometric techniques, we can add optical observables [2], which are derived from the pictures acquired by onboard cameras. Depending on the processing involved, the observables may be of different types (e.g., landmarks, or centroids). These observables provide direct information about the distance and/or attitude with respect to the observed target.

### 1.2.1 Radiometric observables

Here it follows a description of the radiometric observables used in current space missions. In most common situations, Doppler and ranging observables are used as a primary source of data for the OD problem, whereas Delta-DOR measurements are only introduced to obtain more accurate information. In particular, this applies when the knowledge of the heliocentric state of the spacecraft is more critical, like during the initial approach to a target celestial body. These radiometric observables alone are currently capable of high scientific results in the estimation of the gravity field of planets, comets, and asteroids, and they are the current state of the art for gravity field estimation.

#### Range

This type of observable measures the time it takes a properly modulated signal (see also [24]) to cover the distance between a sender and a receiver, and provides a value that can be expressed, for example, in range units ( $RU$ ). The timing information related to the range observable is dependent on the speed of light, and it has a different meaning depending on the configuration which is used.

In the case of a one-way configuration, the information is extracted from the difference in times  $\tau$  of the signal sent from the spacecraft and the same signal received at the ground station, measuring the OWLT. If we consider the range  $\rho$ , expressed as a distance, and the speed of light  $c$  we have:

$$\tau = \frac{\rho}{c} \tag{1.19}$$

As it may be seen in Figure 1.2, if the signal is transmitted from the spacecraft at time  $t_1$  and received from a ground station at time  $t_2$ , the distance measured is between the position of the spacecraft and ground station while taking into account the relative motion of the bodies. However, the one-way configuration is inherently affected by large errors, since the onboard oscillators have lower performances in terms of frequency stability, often expressed as Allan variance [25], than the ones located at the ground stations.

The three-way configuration is a degraded version of the two-way in terms of achievable accuracy since there is the added interstation clock-drift. Thus, the two-way configuration is usually preferred, and it is the one considered in the simulations for this study. In the latter case, the signal is sent from a ground station transmitter at an instant of time  $t_0$  and it is received at  $t_1$  from the spacecraft; then, the signal is locked and sent back in a different frequency band (the transponder turnaround ratio [26]), which is introduced to avoid interference; finally, the signal sent from the spacecraft is received at  $t_2$  from the original ground station receiver (if two-way) or from a different one (if three-way).

In a first approximation, the two-way measurement is related to:

$$\tau = \frac{\rho_{up} + \rho_{down}}{c} \quad (1.20)$$

Where  $\rho_{up}$  and  $\rho_{down}$  are the one-way range observables for the uplink and downlink paths, divided by the speed of light in the medium,  $c$ .

In a more detailed description, many different delay effects should be considered, such as charged particle delays introduced by the ionosphere, the transponder, and ground station-based delays.

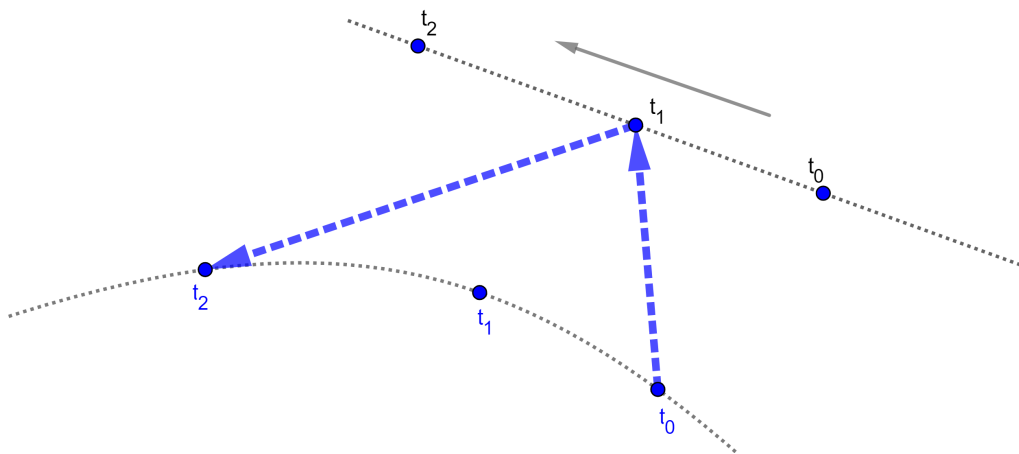


Figure 1.2: Range two/three-way geometric description.

### Range-rate

The range-rate observables are extracted from the Doppler shift present on the carrier frequency of the transmitted signal. In this way, the effects due to the relative velocity in the line-of-sight (LOS) of the transmitter with respect to the receiver can be measured. Even in this case, there are many configurations, and the two-way range-rate (F2) is the most accurate one and therefore the one that will be considered in this analysis. An approximate description of the received frequency received as a function of the range-rate

is:

$$f_r = f_t \left( 1 - \frac{\dot{\rho}_{up} + \dot{\rho}_{down}}{c} \right) \quad (1.21)$$

Where  $\rho$  is the range rate,  $f_t$  is the transmitted frequency from a ground station and  $f_r$  is the one received back at the ground station after being retransmitted by the spacecraft transponder.

It is possible to compute the Doppler shift by integrating the phase variation over a count time:

$$F = \frac{1}{t_f - t_0} \int_{t_0}^{t_f} (f_{REF} - f_t) dt \quad (1.22)$$

Where  $f_{REF}$  is usually taken as the transmitted frequency  $f_t$ , scaled by the turnaround ratio, and  $T = t_f - t_0$  is the count time.

### Delta-DOR

The delta-DOR observable provides information about the incoming angle of a signal with respect to a baseline composed of two widely spaced ground stations. If the source of the incoming signal is sufficiently far, the incoming wavefront can be considered planar, such that the approximation in Figure 1.3 is valid.

In this case, delta-DOR is a one-way type of observable, since the ground stations are receiving radio signals emitted from the spacecraft. To compute the differential ranging  $\rho$ , the signal from both ground stations is correlated, to find a time delay:

$$\tau = t_1 - t_0 \quad (1.23)$$

which is proportional to the differential ranging, if multiplied by the speed of light  $c$ :

$$\boldsymbol{\rho} = c \tau \hat{\mathbf{d}} \quad (1.24)$$

Which is a vector directed as the incoming wavefront  $d$ . In this case, the correlation is not performed in the classical sense, but after phase extraction from different DOR tones, which are unmodulated sine wave functions at different frequency values [27], and the time delay is found as the value which best fits all the phases.

Therefore, since the baseline vector  $B$  is known and considering  $\hat{\mathbf{b}}$  its direction versor, it is possible to link the differential ranging observable  $\rho$  with the direction of the incoming signal  $\theta$ , since:

$$\cos(\theta) = \hat{\mathbf{b}} \cdot \hat{\mathbf{d}} \quad (1.25)$$

Thus, providing angular information for the spacecraft position starting from a measured time delay  $\tau$ . However, this measurement is affected by huge errors, therefore an additional correction is required.

The estimated correcting factor is provided by the differential ranging of another incoming wavefront, in this case, emitted by quasars. Those are far sources of electromagnetic noise provided by active black holes, whose positions are well known in the plane of the sky, thanks to continuous surveys performed with the very long baseline interferometry (VLBI) network of high-gain antennas. In this case, the data is not in the form of pure sine waves, therefore it is possible to extract the time delay  $\tau_q$  through a correlation in the classical sense.

Since the position of the quasars is known with high accuracy, a measurement of  $\tau_q$ , which provides the quasar differential range, can yield information about the expected error in the measurement for the spacecraft, thus removing by default the clock offset of the stations and other correlated error sources. In addition, to better approximate the correction value, spacecraft and quasar measurements are collected on an alternating schedule, and the calibration value obtained from the quasar is interpolated for the time instants in which the spacecraft measurements are acquired.

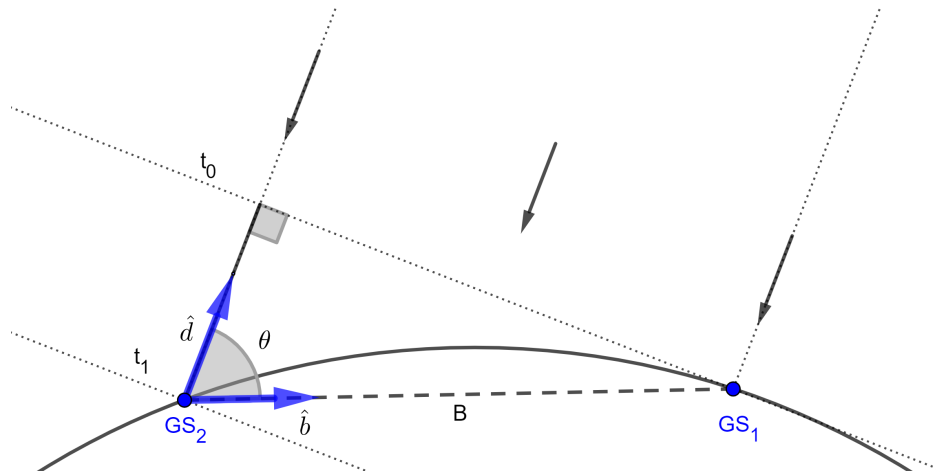


Figure 1.3: Delta-DOR configuration.

## 1.2.2 Optical observables

These observables can be collected from optical payloads present on the spacecraft, such as navigation or scientific cameras. The main difference with respect to the radiometric observables is that the images usually need to be transferred to the ground stations for processing, thus their total collection is mostly limited by the download data budget allowed for the instrument. For the acquisition of radiometric observables, instead, only limits due to the required power and attitude apply, if the ground stations are available for the tracking.

Since the optical observables are more sensitive to certain types of parameters than radiometric observables, they can provide improvements to their estimation. The information

that cameras provide is related to the plane of the sky, which corresponds to a direction of an imaged body or features in the field of view (FOV) of the camera.

Some methods for the extraction of optical observables are related to the tracking of local or global features, such as:

- Center-finding techniques [28], which can be accomplished through limb fitting [8] in the case of large bodies, or through analysis based on the measured brightness in the case of stars or asteroids. This latter analysis requires a comparison with star catalogs and eventually the collection of multiple pictures to properly discern a bright pixel among far asteroids, comets, stars, or single event upsets (SEU) due to background radiation [3].
- Surface landmarks or features, which applies when dealing with bodies whose re-projected dimension in the FOV is sufficiently large so that surface details can be resolved. By combining many pictures taken from different locations, even some 3D geometric reconstructions can be applied. This is a natural outcome of stereo cameras [29], [30], but it is also possible to adapt images taken from a non-stereo camera at different time instants using stereo photogrammetry [31], [32]. If the lighting conditions are not consistent between shots, which is a scenario extremely emphasized with small bodies such as asteroids and comets, stereophotoclinometry techniques come to help [33], [34].

The outcome of all the different optical techniques is a pixel position expressed in terms of sample and line, which are the row and column indices of the camera sensor. The pixel position observable, which refers to a particular element in the captured image, can be used in the estimation process, where its computed value from the dynamical model is compared with the observed one. In the case of the Hera mission, since the spacecraft will be orbiting the system for many months (from February to July 2027), we can consider the higher accuracy observables which are provided by means of multiple images processed with stereophotoclinometry techniques.

### 1.2.3 Noise sources

There are many sources of noise that affect the radiometric observables, which can occur in the tracking instruments, in the transmission media, and in the tracking model geometry. The effect they have is here briefly described [23].

- Clock instability; it derives from the oscillator noise, which distorts the reference frequency used for range-rate measurements. This is mitigated by using the same clock both on the transmitting and receiving side, therefore in a two-way configuration, since stability is an intrinsic characteristic of the oscillator.

- Non-dispersive transmission media, which are delays not frequency dependent, such as tropospheric delays (both dry and wet components, which can be calibrated with dedicated instruments).
- Dispersive transmission media, where the delays introduced by solar plasma or Earth's ionosphere are decreasing with the frequency squared (thus having a lower effect at larger frequencies). With multiple frequency measurements, it is possible to compensate for these errors.
- Random instrumental noise, mainly due to thermal effects in the electronics which are involved in the extraction of radiometric observables.
- Systematic instrumental noise, introduced by antenna multipath and either dispersive (if frequency dependent) or non-dispersive instrumental delays.
- Model errors, arising from incorrect spacecraft integrated trajectory due to mismodelling of non-gravitational and non-deterministic models.

In case of optical observables, we can consider:

- Model errors as well, where the spacecraft trajectory errors affect the content of the images.
- Sensor noise, which degrades the quality of the content of the images, such as thermal noise, shot noise, single event upsets (SEU), hot pixels, sensor's non linearities, blooming, readout smear noise.
- Pointing instability, which can cause blurring, and its magnitude is proportional to the total camera integration time.
- Optical misalignment, due to thermal expansion and erroneous installation of the optics with respect to the sensor position.
- Optical distortions, which depend on the lens and filters used and that need to be properly calibrated in order to accurately assess the direction each pixel is really pointing.
- Image processing, depending on the applied method, we can have different accuracies in the final optical observables provided.

The error sources that mostly affect the stereophotoclinometry technique are the ones that introduce a mismatch in the pixel position, therefore the optical distortions, misalignments, and model errors.

### 1.3 The Hera Mission

The European Space Agency’s Hera [1] is a planetary defence mission first in its kind, named after the Greek goddess of marriage. The design of the mission takes inspiration from the Asteroid Impact Mission (AIM) project [35], which had the purpose of investigating the structure of a near-Earth binary asteroid system and providing different type of technology demonstrations in an international collaboration, the Asteroid Impact Deflection and Assessment (AIDA) [36]. For these kinds of binary asteroids, a rendezvous has never been performed, thus the current knowledge of their history, properties, and dynamics is limited.

Hera aims to investigate the same near-Earth binary system targeted by the AIM mission, which is composed of the asteroids Didymos, the primary and largest body, and Dimorphos (Figure 1.4). Didymos is an S-type asteroid [37] and it has been estimated from Earth-based measurements that it is a triaxial ellipsoid whose dynamically equivalent equal volume axes are  $783 \pm 6\%$ ,  $797 \pm 6\%$ ,  $761 \pm 10\%$   $m$  (1-sigma uncertainties), and maximum extent is  $832 \pm 6\%$ ,  $838 \pm 6\%$ , and  $786 \pm 10\%$   $m$  (1-sigma uncertainties), while Dimorphos is expected to have a prolate ellipsoid shape with a major axis of  $150 \pm 20\%$   $m$  (1-sigma uncertainty) [38]. They are Potentially Hazardous Asteroids (PHA), since their minimum orbit intersection distance with Earth is lower than  $0.05 AU$ , and their maximum dimensions are larger than  $140 m$  in size; as a reference, a near-Earth Object (NEO) whose dimensions are in the order of  $30 m$  could provide vast damages in the proximity of their impact.

On 26 September 2022, NASA’s Double Asteroid Redirection Test (DART) probe [39] impacted the surface of Dimorphos, in an attempt to modify its momentum and trajectory. At that date, Didymos was near its closest approach to the Earth, and DART impacted the secondary body at a speed of approximately  $6 km/s$ . Before the impact with DART, Dimorphos had a period of revolution around Didymos of roughly 11 hours and 55 minutes, which was estimated via Earth-based measurement (e.g. time of binary occultation from astrometric observables). The same measurements have confirmed that the impact provided a variation to the orbital period of about  $33 \pm 1$  minutes (at 3-sigma) [40], way above the variation of 1 minute and 13 seconds required as a minimum value to consider the impact successful.

At the same time of the impact, another small spacecraft, the Italian Space Agency’s LiciaCube [41], was witnessing and recording the event of the *kinetic impactor* (KI), by acquiring pictures of the plumes generated after the collision, formed by ejected rocks and dust particles.

The Hera mission is meant to be launched in October 2024 and will reach the Didymos binary asteroid system in 2027, where it will study the effects of the impact of DART, to fully validate the kinetic impactor technique. The effects related to the deflection

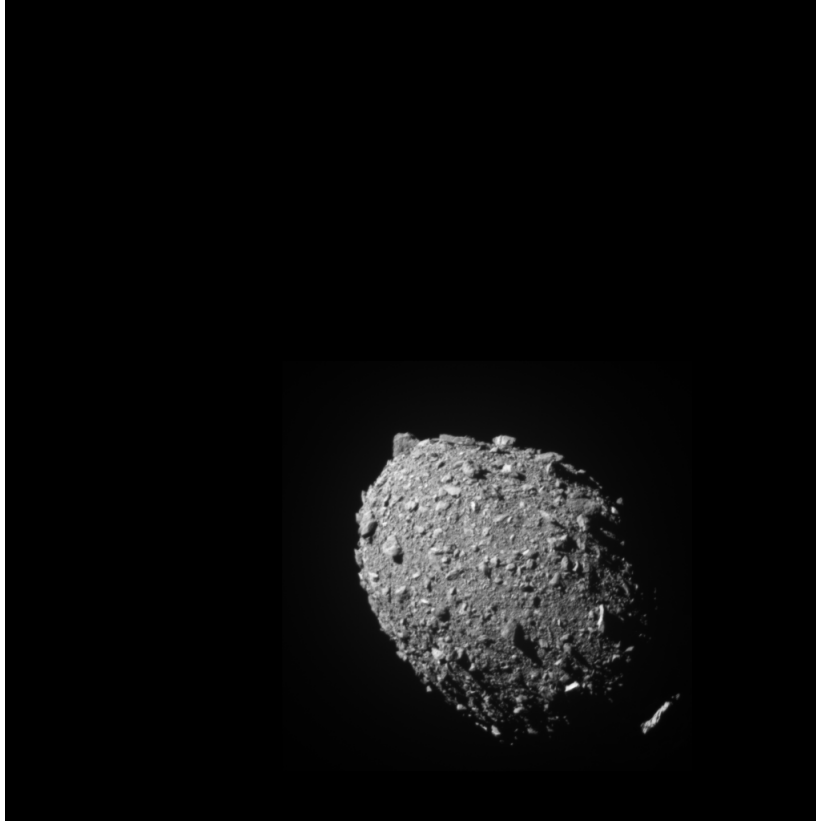


Figure 1.4: Dimorphos as seen by the DART spacecraft 11 seconds before impact. Source: <https://dart.jhuapl.edu/Gallery>, NASA/Johns Hopkins APL.

capability that will be studied are [1]:

- a quantitative measurement of the momentum transfer provided by the impact with NASA's spacecraft, from the precise measured mass of Dimorphos.
- a detailed survey of the impact crater left on Dimorphos, to improve knowledge about the way craters are formed and how this affects the momentum transfer efficiency.
- study dynamical effects such as libration due to the impact, and orbital and spin excitation of Dimorphos.
- provide information about the morphology, the superficial and interior properties of Dimorphos, so that it is possible to better scale the momentum transfer efficiency to differently sized asteroids.

There are also other unanswered questions, such as how much energy is required to achieve a certain degree of disruption in the body, and which amount is transferred to rotational energy. Furthermore, the impact models available to date are valid for high gravity bodies, therefore it is difficult to describe the way craters form in low gravity bodies with

the current knowledge. However, the mission will also perform other scientific analyses, to obtain:

- the first characterization of a near-Earth binary system, to validate the current mathematical models and to assess the production mechanisms that lead to the formation of near-Earth asteroids (NEA).
- analyze how the properties of the material composition of the two bodies affect the formation of asteroid satellites.
- the first study of the effects provided by impacts between asteroids, since they are similar to DART impacting velocity (which was approximately  $6 \text{ km/s}$ , while the average impact speed for asteroids is about  $5 \text{ km/s}$ ).
- study the surface and geophysics of two bodies probably formed by the same material but with different sizes and gravitational fields.
- obtain measurements about the properties of asteroids, whose size is in-between gravity- and strength-dominated structures.
- since the impact velocity is known, it is possible to address which parameter between gravity and strength is most influential in crater formation; the impact models available to date are valid for high gravity bodies, therefore the ways craters form in low gravity bodies are difficult to be described with our current knowledge.
- observe particle emission events, both due to the impact with the spacecraft or the naturally occurring ones.
- analyze the material below the surface, which didn't sustain the process of weathering, to better characterize how space-weathering in the inner Solar system occurs.
- check if the mission Hayabusa2, with its impactor on Ryugu, formed a crater in the gravity regime, by comparing the results of DART and Dimorphos.
- study the effects on the structural stability of a body characterized by a fast spin rate, such as in the case of Didymos.

This will be achieved in collaboration with Milani [42] and Juventas [43], the two CubeSats that will support the main actor in its analysis of the binary system. They are characterized by a low-frequency monostatic radar payload (JuRa) and a gravimeter for small solar system objects (GRASS) for Juventas, and cameras at different spectral ranges, near-infrared (ASPECT) and micro-thermo-gravimeter (VISTA) for Milani, to get a better insight into the mineral composition of the asteroid boulders. Both carry the inter-satellite link (ISL) transponder.

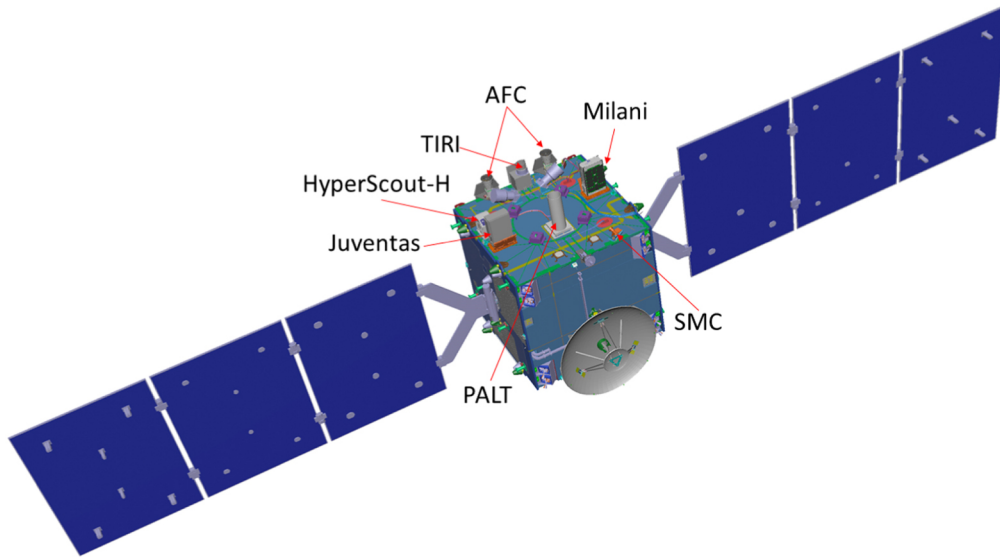


Figure 1.5: The Hera spacecraft and its instruments, source [1].

### 1.3.1 The spacecraft

Hera is a small-to-medium-size spacecraft powered by solar panels, which will carry different scientific and operative instruments (Figure 1.5), for its different scientific goals, such as:

- The Thermal Infra-Red Imager (TIRI), which will perform mid-infrared mapping of the surface of Dimorphos to constrain surface properties [44], and estimate its thermal inertia and composition.
- The Planetary Altimeter (PALT), a micro light detection and ranging (LIDAR) Time-of-Flight altimeter, is characterized by a Cassegrain telescope design composed of two mirrors, a lens, and the sensor. Its goal is to measure the distance of the spacecraft with respect to the target from laser emissions, but also to provide near-asteroid guidance and measurements about the albedo [20].
- The X band deep-space transponder (X-DST), used both for navigation and for the Hera Radio Science Experiment (RSE). It will provide radiometric observables useful to characterize the gravity field of the bodies, with the help of the inter-satellite links (ISL) with the CubeSats, while taking advantage of the pictures for better constraining the estimation process.
- The Asteroid Framing Cameras (AFC), characterized by different spectral filters, which will capture images useful for inspection and optical navigation, whose instantaneous/pixel field of view (IFOV) is about  $94.1 \mu\text{rad}/\text{pixel}$ .

- The Hyperscout-H Spectral Imager, characterized by a mosaic filter, will capture images in the visible near-infrared spectrum, to identify asteroid spectral classes and weathering effects at a resolution of  $133.1 \mu\text{rad}/\text{pixel}$ .
- The Small Monitoring Cameras (SMC).

The communications are performed with ground stations and the two CubeSats by means of a fixed high-gain antenna (HGA), and two low-gain ones (LGA).

### 1.3.2 Mission timeline overview

The launch of Hera will be between the 8<sup>th</sup> and 25<sup>th</sup> October 2024, with a Falcon 9 deep-space launcher. It will perform a maneuver between 2 and 3 weeks after launch, to which it follows a swing by Mars and another maneuver. The arrival, predicted for December 2026, will be characterized by five maneuvers ending with the orbit insertion into the binary system at the beginning of February. If the launch window in 2024 will not be feasible, other launch opportunities will delay the arrival at the system to the end of 2030. The mission will be divided into different phases following the orbit insertion:

1. Early characterization phase (ECP), six weeks with hyperbolic arcs at a distance of 20-30 *km* from Didymos and Dimorphos. In this phase, it is possible to assess the global shape of the asteroids, together with the thermal properties and mass of the bodies.
2. Payload deployment phase (PDP), two weeks with the same arcs as per the ECP, in which Juventas and Milani are released.
3. Detailed characterization phase (DCP), four weeks where the same hyperbolic arc scheme is followed, but at a closer distance, between 8-20 *km*. At this point, autonomous attitude guidance with the position of Didymos will be used. In this phase, the asteroids can be mapped at meter-scale level, analyzing their interior and superficial properties.
4. Close observation phase (COP), six weeks again with hyperbolic arcs, but with the pericenter at about 4 *km*. This phase is characterized by full autonomous attitude guidance, and the PALT will be used for this purpose.
5. Experimental phase (EXP), six weeks, where innovative navigation techniques related to low altitude flybys can be tested (up to altitudes  $< 1 \text{ km}$ ), as well as autonomous attitude, trajectory guidance with the laser altimeter and features tracking. High-resolution data up to decimeter level can be acquired in this phase. The mission will be followed by Hera landing on Didymos.

### 1.3.3 Hera Radio Science Experiment

The Hera mission, with its Radio Science Experiment (RSE), is the key to providing an accurate measurement of the gravity field, orbits, and rotational dynamics of both Didymos and Dimorphos. In fact, information about the gravity field is fundamental to constraining the interior structure of the bodies, while the study of the orbits will allow for better insights into the momentum transfer efficiency provided by the kinetic impactor. This will be accomplished thanks to the Doppler and ranging radiometric techniques, together with the images provided by the AFC. To this extent, the experiment takes advantage of the following contributions:

- the ground based radiometric tracking performed between Hera and the ground stations, considering a standard two-way link in the X-band with a coherent transponder.
- the images captured by the AFC.
- the satellite-to-satellite radiometric tracking, or inter-satellite link (ISL), between Hera and the CubeSats, which provides high-accuracy measurements in the low-gravity environment, thanks to the proximity of Juventas and Milani to the observed bodies. The ISL will be performed in the S-band with a maximum range of 60 *km* and will allow observing the  $J_2$  gravitational parameter, which is not observable by Hera alone.

The onboard X band deep-space transponder (X-DST) will provide an end-to-end Allan standard deviation of  $2e-15$  at 1000 *s* of integration, which corresponds to an error in the measured velocity of 0.6  $\mu m/s$  at 1000 *s*. The expected error on the ranging data is about 3.4 *ns* for the high frequency noise, to which are added 3 *ns* for the calibration error and 3 *ns* due to the drift, which fulfils the requirements when Hera was being studied under the name AIM [45].

In this study, we will focus on the generation of the images captured by the AFC, to better constrain the estimation process of the OD.

### 1.3.4 Hera Asteroid Framing Camera

The Hera Asteroid Framing Cameras (AFC) are two identical multispectral imagers based on Jena Optronik's Astrohead cameras [1]. They are both composed of a CMOS sensor, located at the focal plane of the optics, and their characteristics are depicted in Table 1.1.

Table 1.1: Characteristics for the AFC.

Sensor type	FaintStar CMOS Active Pixel
Active area dimension	1020 × 1020 pixels
Field of view	5.5 × 5.5 deg
IFOV	94.1 $\mu$ rad (5.4 <i>mdeg</i> )
Spectral range	370 - 1100 <i>nm</i>

The AFC will provide useful information for the navigation of the spacecraft during the far approach and nominal phases of the mission at the binary system, while it will also be used for scientific return.

In fact, the AFC aims to:

- contribute to the creation of global maps of Didymos and Dimorphos, with stereophotogrammetry and stereophotoclinometry.
- provide light curves of the binary system during cruise.
- allow the Radio Science Experiment, which will address the gravity field, to assess the rotational state of the body thanks to the precise OD, and to constrain the density and inner structures, combining the gravity field and the three-dimensional shape.
- describe the surface geomorphology and reflectance properties at both global and local scales.

In our simulated experiment, the boresight of the camera is chosen to be in the Z-direction of a right-handed frame, whose origin is in the center of the camera sensor and the X- and Y- axes are in the plane of the sensor, as it is depicted in Figure 1.6. The convention for the pixel count of samples (X direction) and lines (Y direction) starts from the bottom left corner.

## 1.4 The Dynamical model

For the estimation of the parameters of the system in which we are interested, we first need to define a dynamical model to be used in the solution of the OD problem. This should describe the motion of all the bodies involved. The dynamical model is defined within the MONTE [46] frame, which is a software developed since the late 2000s at the Jet Propulsion Laboratory (JPL), and it is the current navigation standard for NASA’s missions.

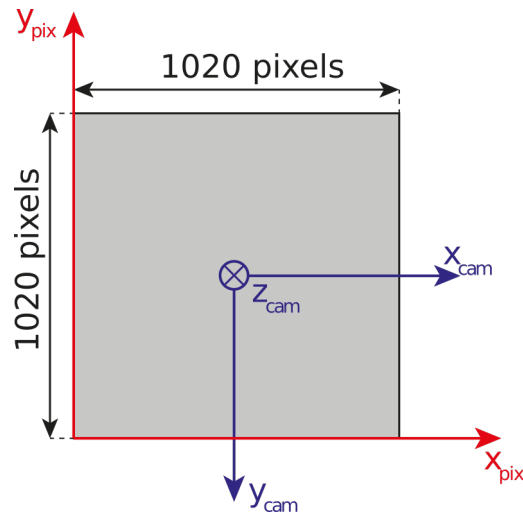


Figure 1.6: Representation of the CMOS sensor mounted on Hera AFC.

The dynamical models considered will be divided into gravitational and non-gravitational accelerations:

- For the gravitational acceleration we consider the effects of the Sun, the solar system planets and satellites, and the asteroids of the binary system, Didymos and Dimorphos.
- Among the non-gravitational accelerations, we will consider the solar radiation pressure (SRP).

The maneuvers performed during the mission, starting from the Early Characterization Phase, up to the Experimental Phase, will be performed between the considered arcs. Since we are integrating the spacecraft trajectory using the estimated positions available at the middle of each arc, we don't need to introduce the maneuvers to the model.

This section will begin with a definition of the reference frames used in this description (subsection 1.4.1), followed by the description of the system's parameters and models considered in the implemented dynamical model (subsection 1.4.2, subsection 1.4.3, and subsection 1.4.4).

### 1.4.1 Reference frames

Many reference frames are required during the overall analysis of the setup. Here we define the most important ones which will be considered:

- **J2000/EME2000 Reference Frame**

This frame depends on the Earth Mean Equator at epoch J2000 (1 January 2000 12:00 ET). The Z axis is directed as the normal of the mean equator, the X axis can

be found as the intersection between Earth’s ecliptic plane and Earth’s equatorial plane (equinox at epoch J2000). The Y axis is chosen so that the reference frame follows the right-hand convention.

- **EMO2000 Reference Frame**

Earth Mean Orbit at epoch J2000, defined similarly to EME2000, where the Z axis is directed as the normal of the Earth’s ecliptic plane instead.

- **Didymos Body Fixed Reference Frame**

The reference frame origin is located in the center of gravity of Didymos. The Z axis is directed as the Didymos North Pole (the instantaneous rotational axis), whose coordinates are extracted from the latest knowledge described in the Planetary Constant Kernels (as Right Ascension and Declination with respect to the J2000 frame). The pole spins with an angular velocity of approximately  $7.72e-4$  rad/s, which translates into a rotational period of about 2h15’. This allows for fast changing illumination conditions between consecutive pictures, which is an advantage for the stereophotoclinometry method used to extract the optical observables.

- **Hera Body Fixed Reference Frame**

This reference frame is rigidly connected to the chassis of the spacecraft, with its origin located in the center of gravity. The Z axis is along the nominal boresight direction of the AFC, the X axis is along the nominal boresight direction of the High-Gain Antenna (HGA), and the Y axis direction is chosen to form a right-hand frame. This reference frame is the one which is available in the SPICE kernels of the mission available to date [47], [48].

- **Hera Nadir Pointing Didymos Reference Frame**

We consider Hera’s camera frame as being always pointed towards the center of gravity of Didymos asteroid, while the camera itself is rigidly connected to the Hera chassis. The pointing direction (the boresight of the AFC) defines the Z direction, while the X direction is pointing at the Sun and the Y direction is found so that it forms a right-hand reference frame. In this way, the Sun is always on the opposite side of the radiators. This reference frame can be obtained by applying attitude corrections to the current values described by the kernels to date.

## 1.4.2 Asteroid’s rotational models

The rotation of the asteroids needs to be modeled, since their attitude affects their mutual gravitation interactions and the acceleration imparted on the spacecraft.

In general, a rotational model is composed of spin rate, direction of the spin axis, direction of the prime meridian and a description of the secondary motion types, such as precession,

nutations, librations, or polar motions. The pole orientation for a body can be given as a function of time from a reference epoch, J2000 (1 January 2000, 12:00 ET), expressed in spherical coordinates:

$$\alpha = \alpha_0 + \alpha_1 (t - t_0) \quad (1.26)$$

$$\delta = \delta_0 + \delta_1 (t - t_0) \quad (1.27)$$

Where  $t_0$  is the J2000 epoch. The same formulation is applied to the prime meridian orientation, which is described by an angle which is a linear function of time referred to J2000 as the starting epoch, and represents the spin rate of the body:

$$w = w_0 + w_1 (t - t_0) \quad (1.28)$$

The rotational model considered for the Didymos system was estimated from ground-based measurements; in our analysis, no secondary motion effects are introduced. In Table 1.2 the values adopted in the dynamical model are described. Missing values are considered zero by default.

Table 1.2: Rotational parameters for the binary system.

<b>Didymos</b>		
Base frame	EME2000	
$t_0$ - Reference epoch	J2000	
$\alpha_0$ - Pole Right Ascension	60.94	deg
$\delta_0$ - Pole Declination	-71.67	deg
$w_1$ - Spin rate	3823.01	deg/day
<b>Dimorphos</b>		
Base frame	EM02000	
$t_0$ - Reference epoch	J2000	
$\alpha_0$ - Pole Right Ascension	320.60	deg
$\delta_0$ - Pole Declination	-78.60	deg
$w_1$ - Spin rate	3823.01	deg/day

The values for Didymos are obtained from the latest available SPICE kernels, which refer to [49], while Dimorphos refers to older values [50].

The best estimations about the rotational dynamics are performed with in situ spacecraft-based measurements. However, when those are not available, ground-based observations may be used [51], where information about the rotation is obtained from the observed

light-curves of the object using inversion techniques [52], [53] or through radar images [54]. This latter technique is more accurate with respect to the light inversion but is viable only for near-Earth passing asteroids since the echo of the ground-based radar transmission needs to be collected.

### 1.4.3 Gravitational accelerations

In the description of the gravitational accelerations, we will consider the following models:

- the Newtonian point mass description for the Sun, the planets, and satellites of the solar system.
- the relativistic correction to the simple point mass description for the Sun, Earth, Saturn, and Jupiter.
- the spherical harmonics modeling for Didymos and Dimorphos.

The gravitational parameters, together with the state vector of the Sun and other planets, can be found in the planetary ephemerides DE440 [55], produced by JPL. The references for the Didymos system are the SPICE kernels [56], [57].

The Didymos extended gravity model was obtained considering spherical harmonics up to degree 20, whose coefficients were derived from a polyhedral shape [38], considering uniform density for the body [58]. In the case of Dimorphos, an ellipsoidal model was used, considering uniform density and providing non-zero terms to the spherical harmonics up to degree 2.

The integration of the ephemerides of the system will be divided into three main blocks:

- The integration of the Didymos System Barycenter with respect to the Solar System Barycenter.
- The orbit of Dimorphos and Didymos with respect to the Didymos System Barycenter.
- The spacecraft trajectory in the Didymos System Barycenter.

### 1.4.4 Non-gravitational accelerations

Among all the possible sources of non-gravitational acceleration, in this description only the solar radiation pressure (SRP) is considered. Due to the incoming radiation flux from the Sun, the bodies in space are affected by an acceleration that is provided by the exchange of momentum of the photons with their surface. The total number of incident photons will have different results in terms of momentum variation, depending

on the way they interact with the surface. Therefore, we can differentiate three categories (Figure 1.7), each of them representing a fraction of the total number of photons which reach the surface:

- The absorbed photon fraction  $\alpha$ , which is characterized by the photons that reach the surface and are not bounced back. Therefore, in this case we are considering the black body behaviour of the surface.
- The reflected photon fraction  $\beta$ , which are the photons that leave the surface at a specular angle with respect to the incoming one.
- The diffused photon fraction  $\gamma$ , which means that the photons reach the surface and bounce back in random directions, thus providing an illumination that statistically is directed as all the possible emission directions, with an intensity that decreases as the angle between the local normal of the surface and the emitting direction increases (like in the Lambert reflection description [59]).

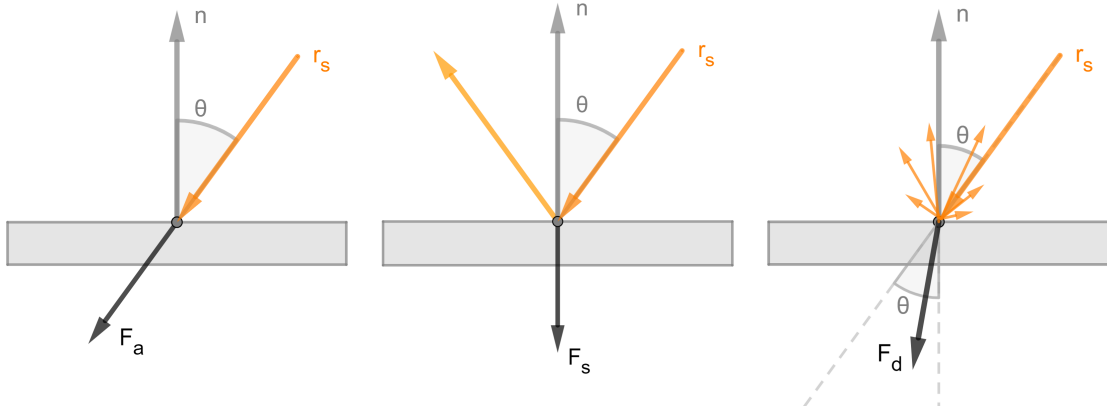


Figure 1.7: The effect on the direction of momentum transfer among absorbed, reflected (specular), and diffused reflection.

The total SRP force, given a flat surface, may be written as the vector sum of:

$$\mathbf{F}_{SRP} = \alpha \mathbf{F}_a + \beta \mathbf{F}_s + \gamma \mathbf{F}_d \quad (1.29)$$

Where, by definition,  $\alpha + \beta + \gamma = 1$ . Considering  $P_{SRP}$  as the solar radiation pressure at a generic distance  $d$  from the Sun, each contribution may be written as:

$$\mathbf{F}_a = P_{SRP} S (\hat{\mathbf{n}} \cdot \hat{\mathbf{r}}_s) \hat{\mathbf{r}}_s \quad (1.30)$$

$$\mathbf{F}_s = 2 P_{SRP} S (\hat{\mathbf{n}} \cdot \hat{\mathbf{r}}_s)^2 \hat{\mathbf{n}} \quad (1.31)$$

$$\mathbf{F}_d = P_{SRP} S (\hat{\mathbf{n}} \cdot \hat{\mathbf{r}}_s) \left( \hat{\mathbf{r}}_s + \frac{2}{3} \hat{\mathbf{n}} \right) \quad (1.32)$$

Where  $a$ ,  $s$  and  $d$  are referring to *absorption*, *specular*, and *diffuse*;  $S$  is the total surface,  $n$  is the normal of the surface,  $r_s$  is the incident direction. Combining all the contributions, we have a model that is valid for a given surface:

$$\mathbf{F}_{SRP} = P_{SRP} S (\hat{\mathbf{n}} \cdot \hat{\mathbf{r}}_s) \left[ (1 - \beta) \hat{\mathbf{r}}_s + 2 \left( \beta (\hat{\mathbf{n}} \cdot \hat{\mathbf{r}}_s) + \frac{\gamma}{3} \right) \hat{\mathbf{n}} \right] \quad (1.33)$$

From (1.33) it is possible to obtain the finite element version, applying the formula to each face composing the mesh of the considered object. This result tells us that the force deriving from the SRP acting on the body is a function of the specular and diffusive reflectivity coefficients and of the orientation of the surface with respect to the Sun. Therefore, for the SRP computation, a shape model of the spacecraft is required. In our case, we are using a simplified flat plate model description composed of:

- The **solar arrays**, described as two flat plates.
- The **high-gain antenna** (HGA), modelled as a dish.
- The **main bus**, as six flat plates which combined form of a rectangular parallelepiped.

This description considers Didymos and Dimorphos as occulting bodies for the incoming radiation flux.

The values required for the SRP computation in the dynamical model are described in Table 1.3, with standard values considered for the thermo-optical coefficients (specular  $\beta$  and diffusive  $\gamma$ ).

Table 1.3: Shape model parameters for the computation of the SRP acceleration in the Hera body fixed frame.

	<b>Direction</b>	<b>Dimensions or area</b>	<b><math>\beta</math></b>	<b><math>\gamma</math></b>
Solar arrays	+Y,-Y	5.60 $m^2$ ( $\times 2$ )	0.038	0.052
HGA	+X	0.90 $m$ radius $\times$ 0.15 $m$ depth	0.0	0.327
Bus Top/Bottom	+Z,-Z	3.60 $m^2$ ( $\times 2$ )	0.0735	0.252
Bus Side Left /Right	+Y,-Y	3.78 $m^2$ ( $\times 2$ )	0.0735	0.252
Bus Front/Back	+X,-X	4.20 $m^2$ ( $\times 2$ )	0.0735	0.252



# Chapter 2

## Optical observables generation

Images of onboard cameras have been extensively used for navigation purposes, but also for the characterization of the structure of celestial bodies, such as comets (67P / Churyumov-Gerasimenko [3]), asteroids (Lutetia [60]), planets, and moons (Vesta and Ceres with the Dawn mission [61]).

In case of small bodies, such as the comet for the Rosetta mission, the optical observable extraction was fundamental both for scientific and navigation purposes. During the mission there was an initial phase (in March 2014) where the centroid of the comet, to be found in the field of view of the Narrow Angle Camera (NAC, 2.2 deg field of view, Osiris instrument [62]), was the considered optical observable which allowed the far approach to the comet. While this method is suitable for large distances between camera and target, it is not as accurate as other methods when the distance is reduced up to a point at which the features of the target become distinguishable.

However, in the case of spinning asteroids characterized by extreme contrast, fast-changing lighting conditions, and a relatively low rate of captured pictures, methods like feature detection or a simple correlation are not applicable for the extraction of optical observables. Therefore, when the spacecraft was sufficiently close to its target, the centroid extraction procedure was superseded by a more sophisticated stereophotoclinometry approach based on the use of landmarks identified on the surface [63]. This latter method which considers the use of landmarks will also be adopted for our case study about the Hera mission.

The general setup for optical observable extraction with landmark matching is depicted in Figure 2.1. The scenario is divided into two different parts, one related to the creation of the computed optical observables, which are the result of the integration of the dynamical model, and a different part, related to the creation of the measured observables.

The short pipeline for the creation of the computed observables requires some initial conditions, provided as ephemerides of the bodies from the SPICE kernels, to compute the trajectories and attitudes of the bodies. Then, once they have been created, it is possible

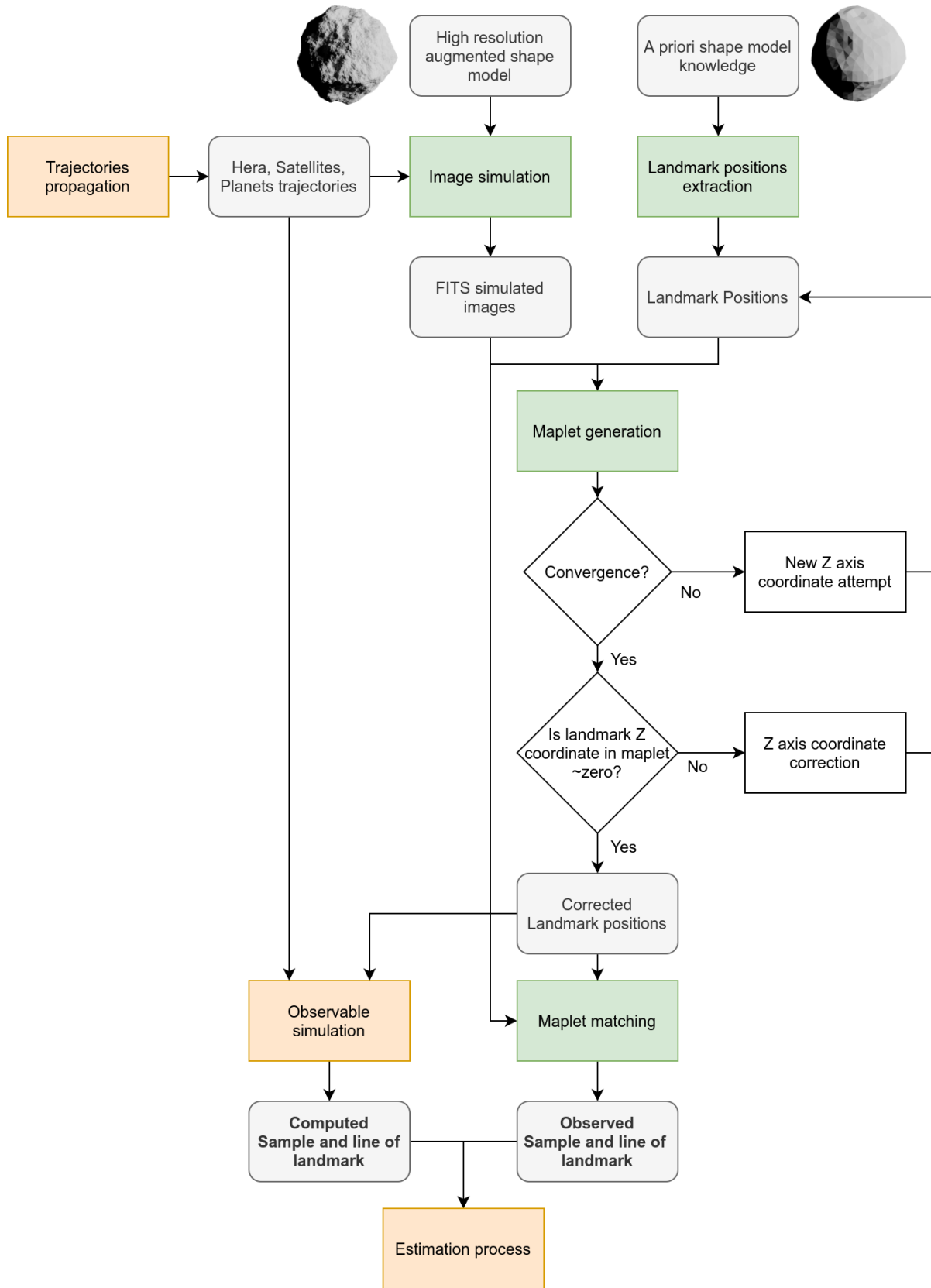


Figure 2.1: Optical observables generation pipeline.

to obtain the computed values for the corresponding counterpart related to the measured observables.

On the other hand, the creation of the observed/measured observables is an almost independent procedure, except for the input of the trajectories, and is related to the simulation of every step of optical observable extraction, starting from realistic images. The procedure is composed by the following main steps:

- **Landmark selection**, expressed in the Didymos body fixed reference frame.
- **Images simulation**, considering the parameters of the AFC.
- **Maplets creation**, height maps, obtained from the input simulated images.
- **Maplets matching**, extracting the sample and line positions of the selected landmarks, using the previously obtained maplets.

The inputs required by this pipeline are the trajectories and attitudes of the involved objects, and an *a priori* shape model of Didymos, which often corresponds to the best shape model available to date. However, for the purpose of simulating OD performances before the mission, a shape model with a higher level of details with respect to the one available in the Didymos Reference Model (DRM) [38] is used for the creation of the simulated images of the AFC. At the end of the process, we obtain the sample and line positions of the landmarks in the camera sensor, together with a better knowledge of their positions in the Didymos Body Fixed reference frame. These values represent the measured optical observables, as if they were obtained from the images collected during the real Hera mission. Afterwards, the newly corrected landmark positions are used to extract the observed sample and line positions in the simulated images, which will be compared with the computed positions obtained from the dynamical model used to integrate the trajectories of the bodies.

## 2.1 Landmarks selection

To generate the optical observables, we need to define in advance an arbitrary list of landmarks placed on the surface of the asteroid. These landmarks are simply defined as constant vectors expressed in the Didymos Body Fixed reference frame, and in principle they should conveniently describe positions placed on the real surface of Didymos. However, the real shape of Didymos is only known with a certain degree of uncertainty, so that the guess value for the landmark position will be improved by an iterative procedure which converges when maplet creation is successful. In theory, to reach convergence a simple displacement of the radial position of the landmark is required, up to a point which is sufficiently close to the real landmark surface which allows the maplet extraction

method to converge.

It has to be noted that landmarks are not necessarily characterized by points on the surface of the asteroid with specific features, such as recognizable boulders or irregularly shaped formations. In principle, landmarks can even be located in the middle of a flat surface, with the constraint that in their closest surroundings some irregularities are present. If these irregularities are capable of providing many different shadowing conditions in the pictures captured by the onboard cameras, a height map (or maplet) can be correctly created. However, if the maplet of that landmark is defining a simple flat plane with no additional features, no information can be used for the stereophotoclinometry method. Therefore, in the following step of maplet matching for the extraction of the optical observables, no particular feature would be available in the images used for the correlation process, so the optical observable cannot be assessed.

Since the real position of the surface of Didymos is not accurately known in advance, we will use a guess value from the best *a priori* knowledge available of the shape of the asteroid, which was extracted from previously collected Earth-based photometric observations and radar measurements. This reference shape<sup>1</sup>, shown in Figure 2.2, is stored in wavefront OBJ format, as a plain text file.

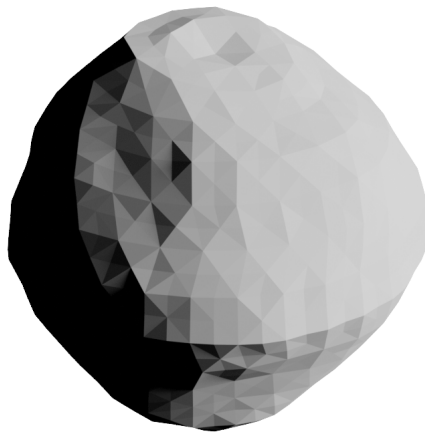


Figure 2.2: Low resolution Didymos reference model, best data available prior to the DART encounter.

In its simplest form, the content can be fully described by only two different fields, such as vertex and face lines in the shape described in Table 2.1.

---

<sup>1</sup>We are using the model `g_50677mm_rad_obj_dida_0000n00000_v001.obj` from ESA's SPICE kernel database, which has a total count of 1996 faces [38].

Table 2.1: Obj data structure.

Line type	Units	Line content
Vertex lines	[length]	$v$ $\langle x \rangle$ $\langle y \rangle$ $\langle z \rangle$
Face lines	[-]	$f$ $\langle nv_0 \rangle$ $\langle nv_1 \rangle$ $\langle nv_2 \rangle$

Each vertex is composed of three cartesian coordinates  $(x, y, z)$ , in this case expressed in  $km$ . Each face is described by three vertex indices  $(nv_0, nv_1, nv_2)$ , which are the incremental numbers of the vertex line indices as they are encountered in the OBJ file, starting from one), and the order in which they are stored gives information about the direction of the normal of the face. The positive normal direction is, by definition:

$$\mathbf{n}_f = (\mathbf{v}_1 - \mathbf{v}_0) \times (\mathbf{v}_2 - \mathbf{v}_0) \quad (2.1)$$

Where this formulation provides a right-handed frame.

For the generation of the optical observables, we will simulate pictures as if they were taken from the onboard AFC, which will be capable of capturing higher frequency details with respect to the ones depicted by the low-resolution version of Didymos. Therefore, a shape model with a much larger level of detail was artificially generated (our truth model, as it was done for other missions [64]), and the result is depicted in Figure 2.3.

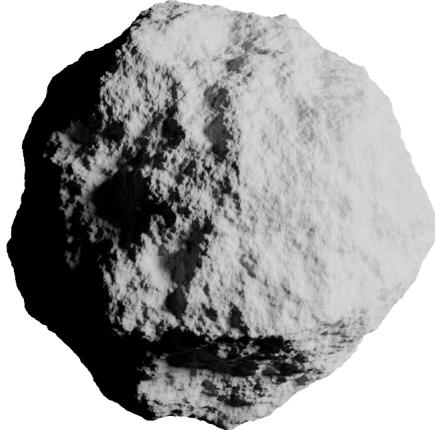


Figure 2.3: Shape model with artificially augmented features. This comprises 786432 faces obtained by applying Perlin noise to the radial position of the shape model coordinates.

The structural features of the low polygon count shape model presented in Figure 2.2 were augmented by means of 3D Perlin noise on top of a version of the low polygon shape model with a much larger number of total faces. The augmented version of the shape model creates a minimum terrain feature resolution which is required for the effectiveness

of the OD process. The maximum deviation in the radial direction from the low polygon version is approximately  $32\text{ m}$ , whereas the mean diameter of the shape model is around  $830\text{ m}$ . The resulting height map for the low-resolution shape model is depicted in Figure 2.4, while the same plot for the augmented shape model is in Figure 2.5. These plots are obtained by interpolation of 4000 discretized values of the surface.

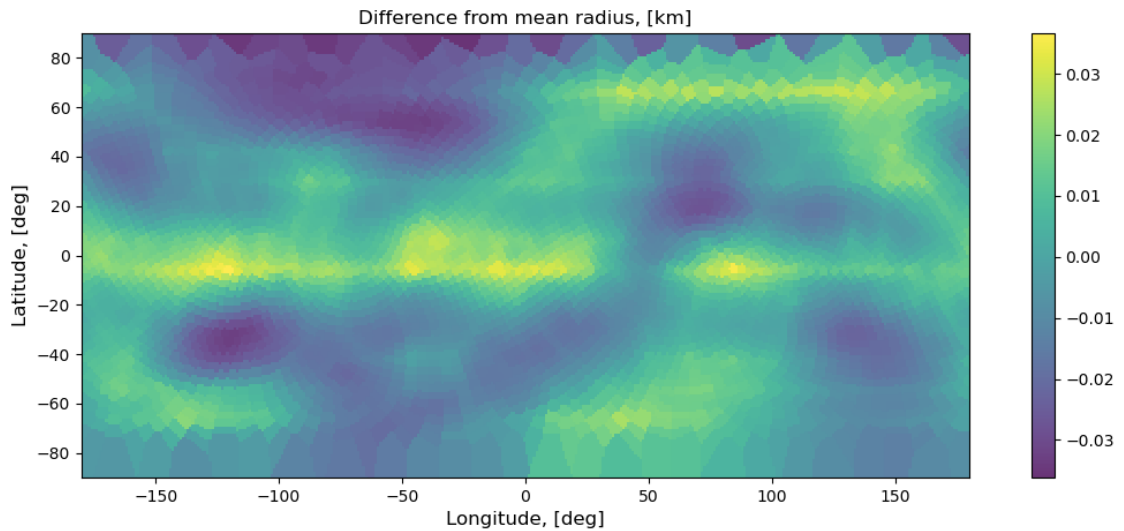


Figure 2.4: Height profile for the low-resolution shape model, expressed as difference of the local surface position with respect to the mean radius.

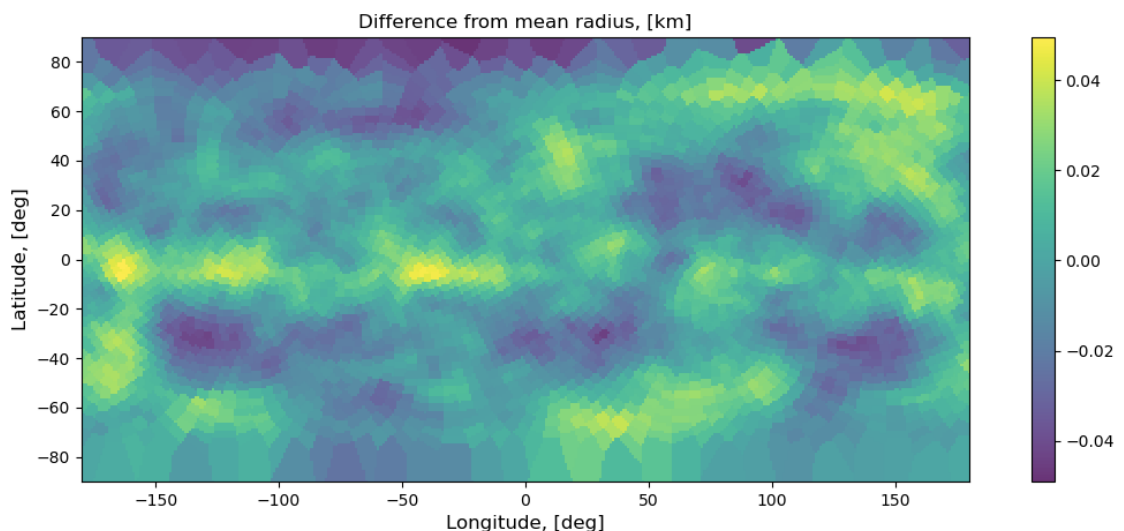


Figure 2.5: Height profile for the augmented shape model.

On top of a given shape model, the landmarks can be selected with many different methods.

- A first method consists of creating a grid of equally spaced longitude and latitude coordinate values and finding the intersection of this angular grid with the selected shape model. Although this method is convenient due to its simplicity, it yields a non-optimal landmark distribution, which is characterized by a scarcity of landmarks towards the equator and an excess of them at the poles.
- Another method consists in selecting landmark directions as a random distribution around a sphere, however this provides a general lack of control about the distance between each landmark, so that many of them are placed too close to each other and do not provide the best coverage of the whole asteroid's surface.

Therefore, a distribution which follows a Fibonacci pattern was considered as a better candidate method for landmark selection [65]. The method obtains a uniform distribution independent on the desired number of landmarks and makes sure that their relative distance is almost the same for each one. In Figure 2.6 it is possible to see the Fibonacci Lattice output of the method as a function of the input number of requested landmarks.

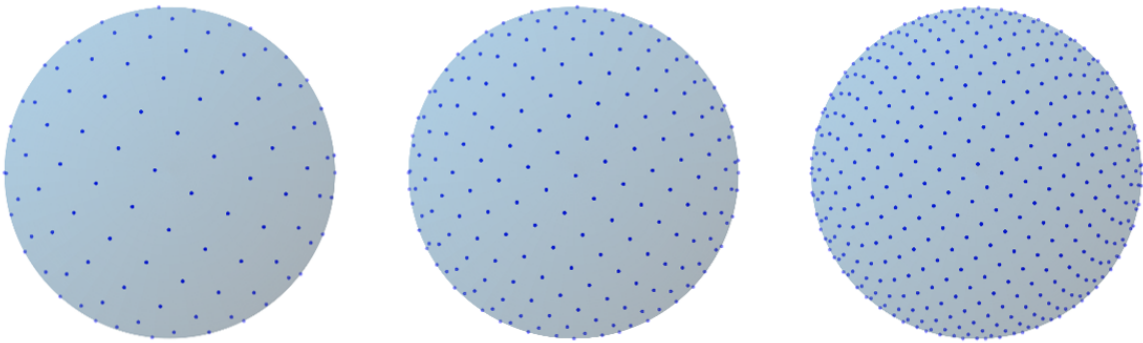


Figure 2.6: The resulting Fibonacci Lattice on top of a spherical surface, using 200, 400, and 800 samples respectively.

The resulting Fibonacci lattice is analytically generated from a spiralling line which starts from a point in a reference sphere, and which is evolving and is being sampled by a function which depends on the total number of desired elements and the golden ratio,  $\phi$ .

Once the landmarks directions obtained with the Fibonacci lattice computation method are found, the landmark coordinates are obtained as the intersection of these directions with the reference shape model of Didymos used for the analysis.

The intersection of the landmark direction with a face of the shape model can be found with the Möller-Trumbore ray-triangle intersection algorithm. This is a numerically efficient method [66] to check if a triangle is intersected by a given ray, and it is capable of best performances when an *a priori* knowledge of the plane equation of each shape model face is not available (such as in our case). Once the intersecting face is found, the intersecting point is computed by combining the line equation of the landmark direction with

the plane equation of the face (which is computed only once, after finding the intersecting face). Recalling the face normal  $\mathbf{n}_f$  from Equation 2.1, the plane described by that face is defined by:

$$(\mathbf{P}_f - \mathbf{x}) \cdot \mathbf{n}_f = 0 \quad (2.2)$$

Where  $\mathbf{P}_f$  is a point belonging to the plane and  $\mathbf{x}$  is a generic point. The line equation is:

$$\mathbf{x} = \mathbf{P}_l + \lambda \mathbf{d}_l \quad (2.3)$$

Where  $\mathbf{P}_l$  is a point on the line of the landmark direction (in our case we will use the *a priori* landmark position obtained by the Fibonacci Lattice method),  $\mathbf{d}_l$  is the landmark direction, and  $\mathbf{x}$  is a generic point. Combining everything together, we get the intersecting point  $\mathbf{x}_0$  as:

$$\mathbf{x}_0 = \mathbf{P}_l + \left( \frac{(\mathbf{P}_f - \mathbf{P}_l) \cdot \mathbf{n}_f}{\mathbf{d}_l \cdot \mathbf{n}_f} \right) \mathbf{d}_l \quad (2.4)$$

To sum up, we use the line obtained from the Fibonacci method inside the Möller-Trumbore algorithm to find the intersecting face, and then we compute the intersection to find the landmark position. The result we get is a series of landmarks distributed on the surface of the asteroid's model, as depicted in Figure 2.7 (in this case, we considered the high-resolution model as the source of intersecting faces).

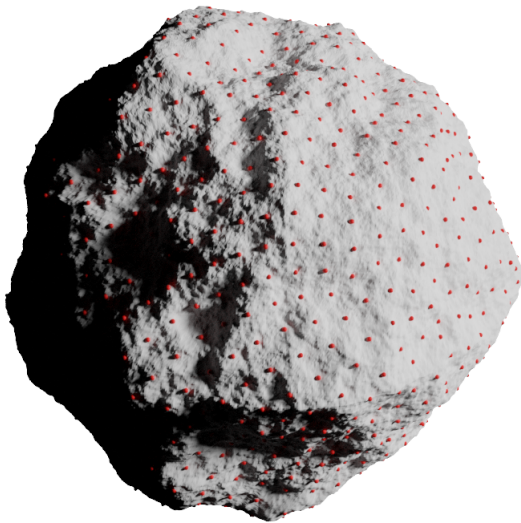


Figure 2.7: A series of 1000 landmarks (in red), distributed as the Fibonacci Lattice and displaced on top of the surface of the augmented Didymos shape model.

After displacing the landmarks so that they lay on the top of Didymos' surface, we obtain a distribution which, in principle, is not perfectly equally spaced anymore, since the Euclidean distance between points depends on the local height gradient. However, the angular separation between landmarks is preserved, which is the most desirable require-

ment about the landmark distribution to avoid cluttering.

The two shape models (the low- and high-resolution versions) provide different local normal vectors at the positions of the chosen landmarks since the local geometry is different. Considering a fine landmark grid, it is possible to show the normal vector angular difference distribution on the whole surface of Didymos; in the case of Figure 2.8 the granularity of the normal vector positions is provided by 4000 landmarks, which have been extracted with the aforementioned Fibonacci distribution.

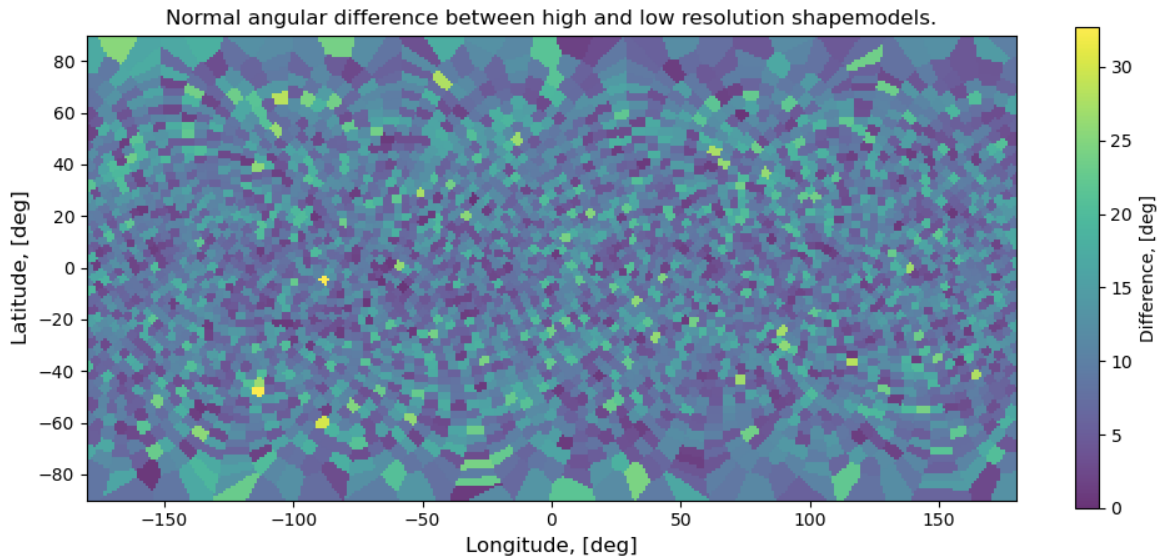


Figure 2.8: Low and high resolution normal angular difference computed at the positions of 4000 test landmarks.

In Figure 2.8, an interpolated distribution of the angular difference between computed normal vector values at the position of the considered landmarks is depicted, with a maximum value of angular difference of about 32 deg.

The normal for a given landmark is computed at two different positions, since the local surface position is shifted due to the introduced Perlin noise in the high-resolution model. Therefore, for our purposes, a landmark is considered the same in both shape models if they only share the same radial direction. The landmark position is found in both cases with the same direction vector intersecting each shape model, while the local normal at that position is computed in two analogous but slightly different ways:

- For the low-resolution shape model, since the number of faces is limited, a small list of vertices surrounding the considered landmark is selected. At first, the closest vertex to the landmark position is chosen; secondly, all the faces that have that vertex in common are selected. Finally, all the faces adjacent to the selected ones are added and all the vertices belonging to the considered faces are fitted with a

best-fit plane. The normal of this plane becomes the computed normal for that landmark.

- For the high-resolution shape model, the number of faces is sufficiently large such that it is no more a limiting factor. By providing a simple filtering based on the distance from the landmark, it is possible to select many vertices and extract the best-fit plane from that list of vertices. In our case, all the vertices which are at an Euclidean distance lower than half of the maximum maplet lateral dimension are considered to compute the best fit plane.

It should be noted that the choice of computing the landmark normal as the best fit plane of multiple vertices around the landmark is driven by the processing routines described in the following sections, which require an accurate *a priori* knowledge of the maplet normal. In this way, it is more representative of the expected normal which will be provided by a local squared maplet, which is a small height matrix associated with that landmark. This is important, since at the exact position of the landmark the normal could be off due to local excessive slopes with respect to the mean normal of the whole maplet.

The computation of the best fit plane is performed using an efficient algorithm based on Singular Value Decomposition (SVD). The algorithm takes all the vertices and shifts them at the origin of the reference frame in which they are described by subtracting from each vertex the barycenter of the point cloud composed of all the vertices. Then, the shifted vertices are all collected in a column vector  $X$  of size  $(M, 3)$ , where each of the  $M$  rows is composed of the 3 cartesian coordinates of each vertex. This vector  $X$  is decomposed into a matrix product  $X_{m \times 3} = U_{m \times m} S_{m \times 3} V_{3 \times 3}^h$  using the SVD algorithm (which can be found implemented in [67]). The direction of the normal of the plane is found as the eigenvector of  $V^h$  corresponding to the minimum eigenvalue (from the diagonal of the diagonal valued matrix  $S$ ). If the method provides the opposite normal direction with respect to the direction of the barycenter of the vertices previously found, then the eigenvector is artificially flipped and the real best fit normal is obtained.

## 2.2 Images simulation

Once we have defined the landmark positions in the Didymos body fixed reference frame, we need different input information for simulating the AFC images, as if they were captured during the mission at the binary asteroid system. Those inputs are then used to feed a photometric model [3], [60], which will output the camera picture files as if they were acquired by the real instrument.

The inputs that are needed to simulate the images are (Figure 2.9):

- the position vectors and quaternions of the AFC, the Sun and the asteroids at the

considered epochs, which are obtained by integrating the trajectories and attitudes of the bodies.

- the AFC optical parameters (i.e. focal length, distortion parameters), the sensor's characteristics (FOV, pixel size and count), the shutter integration time and the general electronic settings (e.g. photon conversion quantum efficiency).
- an *a priori* high-resolution shape model and albedo model of the target asteroid.
- a photometric model describing a realistic reflectance function for the asteroid's surface.

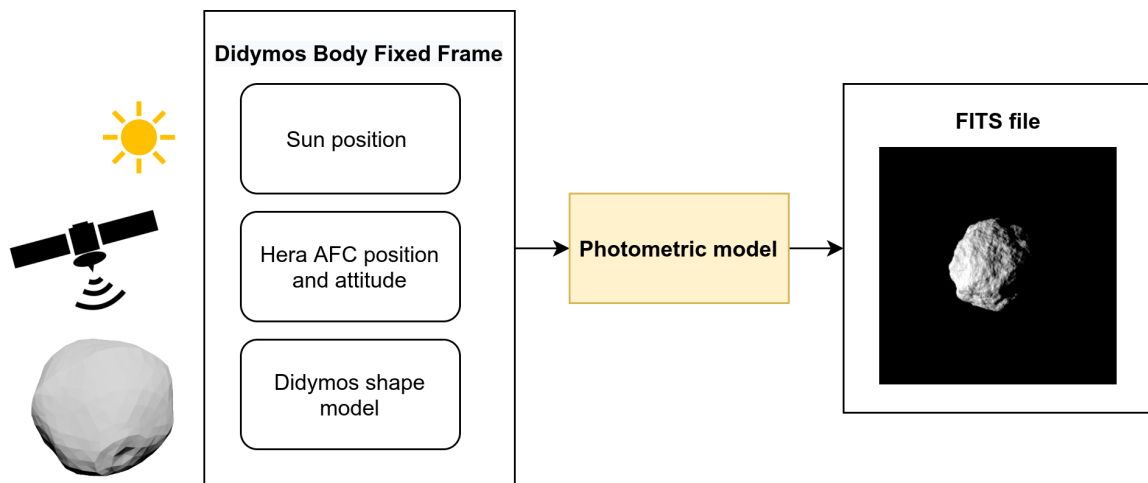


Figure 2.9: High level list of the geometric inputs required for the image simulation.

The shape model of Didymos used for the simulation of images must be at high resolution since it is meant to represent the ground truth asteroid geometry (see Figure 2.3). The resolution can be considered sufficiently high if the reprojected dimensions of its smallest features are at most in the order of magnitude of the pixel size. In the overall pipeline, this high-resolution model is meant to be used only for the simulation of images of the AFC, while all the other steps will consider the *a priori* knowledge of the system instead, such as the low polygon count geometry shown in Figure 2.2.

The images depicted in Figure 2.3 or Figure 2.7 are obtained with a graphic engine mainly used for aesthetic renderings [68], therefore those do not have the same characteristics as a real captured asteroid image, both in terms of bit depth and of photometric models used to compute the brightness of the pixels.

A step related to a photometric model implementation is indeed required for the creation of the final simulated scientific images. In this way we can associate the sensor's signal with the solar photon flux and convert its value to the digital unit (*DU*) count of the pixels with the real AFC parameters, while also providing additional realistic noise sources.

The overall simulation procedure may be simplified in these two different steps:

- **Timeline extraction**, which is also filtered to keep only images valid for the method of maplet creation and used to extract the positions and attitudes of the bodies.
- **Application of the photometric model**, whose output is composed of the final images.

The epochs chosen during the nominal mission are filtered to provide a list of valid pictures, with a constraint applied to the phase angle. These epochs are not filtered per single landmark, but only on a general phase angle valid for the mean illumination of the asteroid. In this way we can have a general database of images that will be filtered by each landmark visibility condition during the creation of each maplet.

Finally, once all the inputs have been acquired, they can be fed into a photometric model, which will provide the final output image in the standard file format used in space missions. These images span the whole mission timeline, and they will be the input for the following step related to maplet creation (see Figure 2.9).

### 2.2.1 Timeline extraction

The image simulation step requires an input timeline for the acquisition of the AFC pictures. It should be noted that the considered procedure will provide a collection of pictures not directly meant for navigation purposes: the rationale of acquisition is intended for a not in real-time processing, since it will provide useful results as soon as a sufficient number of images is available for the geometry reconstruction of the surface. In that case, the timeline may even be tailored to the acquisition of more images in the best overall conditions (like when closer to the surface), or the transmission data rate can even be reduced if strictly unnecessary potential pictures are excluded.

#### Mission overview

The mission's range of dates of interest spans the period between February and July 2027 and it is divided into many consecutive arcs which are defined by the geometry of the trajectories. During the main mission timeline, the distance of Hera with respect to Didymos will be in the approximate range of 5-30 *km*, with different subranges depending on the mission phases, as it is shown in Figure 2.10.

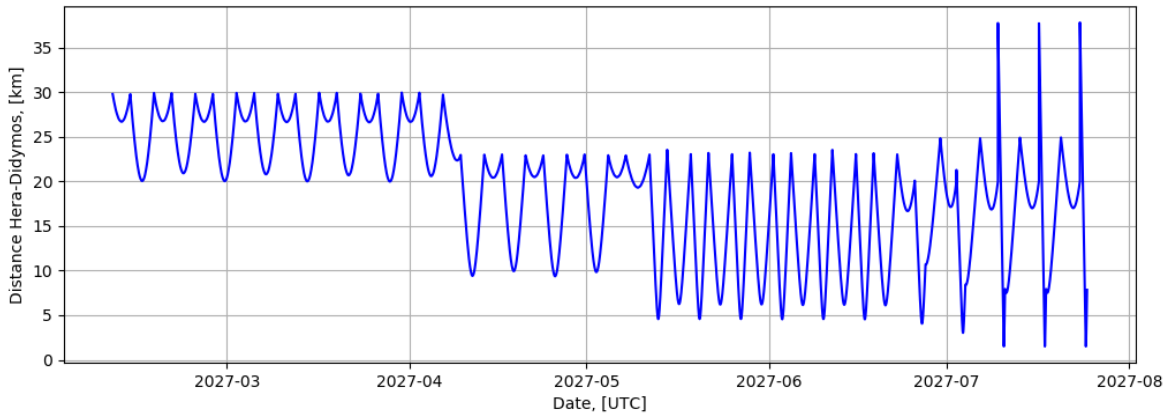


Figure 2.10: Hera-Didymos distance.

And in Figure 2.11 the distance of Hera with respect to Dimorphos for the same time span considered in Figure 2.10 is shown:

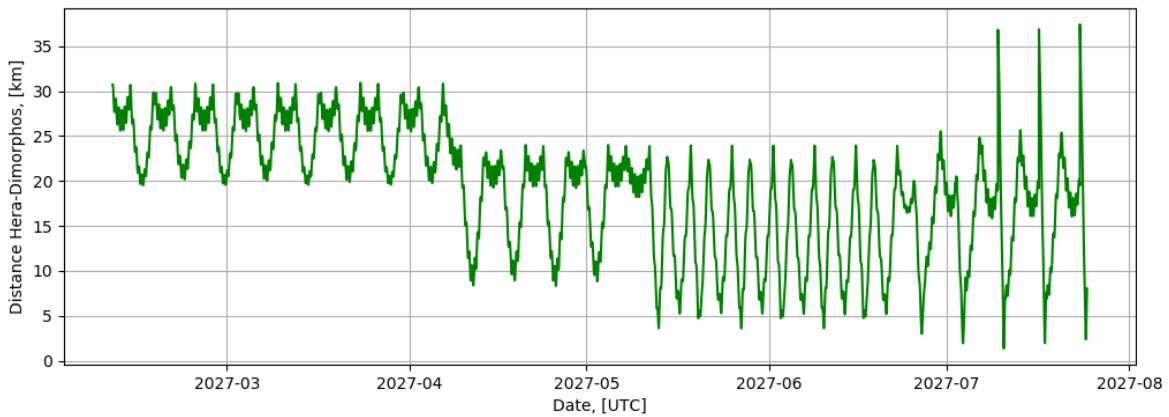


Figure 2.11: Hera-Dimorphos distance.

### Nominal scheduling

Many different scheduling setups can be considered for the acquisition of images; in our case, we will consider a realistic radiometric-dependent case, where pictures are collected only when no radiometric observables are being simultaneously acquired.

This reference setup (Table 2.2) is the one that intervals radiometric and optical observables, with an acquisition pattern that is typical for every single arc.

Table 2.2: Timeline for observable collection during an arc.

Time interval	Observable type
$[t_0, t_0 + N]$	radiometric measurements
$[t_0 + N, t_{C/A} - N]$	optical observables
$[t_{C/A} - N, t_{C/A} + N]$	radiometric measurements
$[t_{C/A} + N, t_1 - N]$	optical observables
$[t_1 - N, t_1]$	radiometric measurements

Where  $t_0$  and  $t_1$  represent respectively the starting and ending epochs of every single arc,  $t_{C/A}$  is the epoch of closest approach of Hera with respect to Didymos and  $N$  is a reference number of hours dedicated to the collection of radiometric observables. The resulting picture acquisition distribution, as a function of the distance from Didymos is depicted in Figure 2.12.

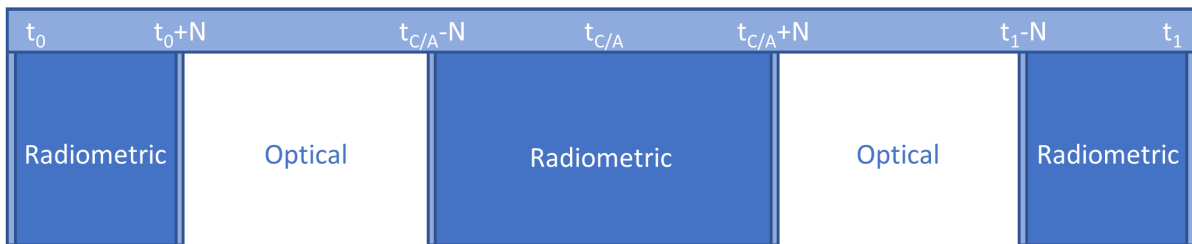


Figure 2.12: Nominal timeline setup for observable acquisition during a single arc.

Considering an acquisition rate of 1 picture per hour in the reserved time windows, and  $N = 4$  hours for the collection of radiometric observables, the proposed nominal setup for the acquisition of optical observables provides the distribution shown in Figure 2.13, where each large gap is 8 hours long.

In our test cases, we will consider a nominal setup comprising a picture every 2 hours, which is a more conservative assumption. The proposed timeline provides an upper limit to the pictures available for optical observable extraction, however this blind selection does not consider the visibility conditions that characterize each of these pictures. Therefore, a further selection based on geometric conditions allows to keep only the images that are providing useful outcomes in terms of quality of the optical observables.

### Filtering images

Once the desired nominal timeline is chosen, it is possible to filter unnecessary images based on generic geometrical and illumination conditions. The filtering step is meant to remove the pictures that will not meet the minimum required quality to provide optical observables, such as good visibility conditions for the landmarks in the field of view of

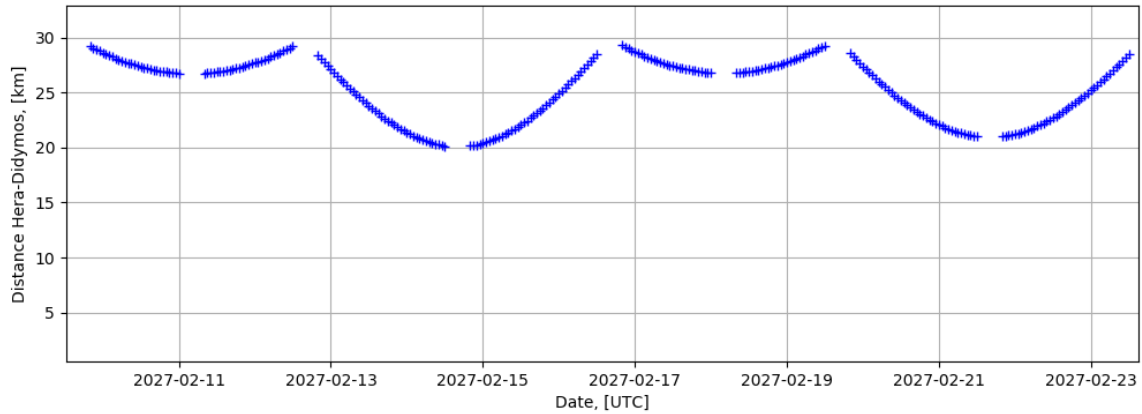


Figure 2.13: Nominal timeline for picture acquisition (considering 4 arcs). Inside the visible gaps, only radiometric observables are intended to be collected.

the AFC. The rationale is that an image is kept if at least one landmark is visible and well lit, otherwise it is discarded.

To properly address filtering based on illumination and visibility conditions, some useful angles should be defined. In photometry, the standard nomenclatures for the angles [60] involved in the imaging of a surface illuminated by a generic light source and observed at arbitrary angles are (Figure 2.14):

- **Incidence angle**, between the local surface normal and the Sun direction.
- **Emission angle**, between the local surface normal and the camera direction.
- **Phase angle**, between the Sun direction and the camera direction.

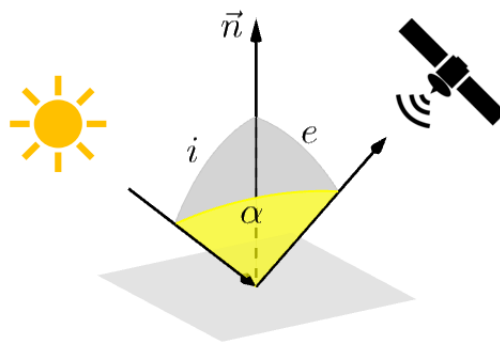


Figure 2.14: Incidence ( $i$ ), emission ( $e$ ), and phase ( $\alpha$ ) angles for a reference surface.

To address the filtering, the spacecraft and asteroids trajectories are integrated with the dynamical model described in section 1.4, starting from the initial conditions provided

by the available SPICE kernels. From the integrated trajectories, the following quantities are evaluated:

- the Sun position coordinates in the Didymos body fixed reference frame, used to filter based on illumination conditions (incidence and phase angles).
- the Hera AFC position coordinates in the Didymos body fixed reference frame, to filter based on geometric visibility of landmarks (emission and phase angles).

At this preliminary step, the surface normal which is used as a reference for the incidence and emission angles is computed assuming a simple spherical model, which means that the normalized landmark position vector directly provides the direction of the local surface normal.

The illumination condition used to filter the images is about both the **incidence** and **phase angles**, which can exclude the images with Didymos completely or partially backlit, thanks to information about the Sun and Hera positions expressed in the Didymos body fixed frame. Conservative values for this filtering are phase angles below 170 deg and incidence angles below 90 deg (which means that the Sun should be above the local horizon for a landmark). In this way we are sure that no useful images are discarded but all the dark images are avoided.

Furthermore, a filtering based on the **emission angle** is applied. The rationale is that the camera should be pointing at the landmarks from above their local horizon so that they are not occulted. The maximum value of emission angle allowed at this step is 90 deg, since for larger values the target will not be visible.

Finally, the images should have the landmarks inside the **field of view** of the camera; this may discard some pictures during the flybys, for which Didymos is filling entirely the sensor frame. This requires the attitude of the AFC, which is needed to properly reproject the Didymos shape model into the correct pixel positions of the camera sensor. In the Hera case, the most convenient frame to be used for representing the attitude of the AFC is one which we here call the **Hera Nadir Frame**, characterized by a commanded attitude where:

- Didymos is at the center of the AFC field of view (the boresight of the camera is along the Z direction of the frame) at each instant of time during the whole mission (Hera is Nadir pointing at Didymos).
- The cross product of a second chosen direction and the Z direction provides the Y axis for a right-handed frame; in our case, we considered the Sun direction so that all the pictures are illuminated from the same side. However, another direction can be chosen if other constraints must be fulfilled (for example, having a radiator for the electronics cooling never pointing to the Sun).

It should be noted that, since the chosen landmark distribution is uniform around the body, this frame will always provide some landmarks in the field of view. Another frame that could be considered is the AFC attitude defined in the Hera SPICE kernels. However, the attitude provided is at its early stages (the CONOPS is currently not defined), so we consider instead the Hera Nadir Frame for all the analyses throughout this study.

Considering a test case of 3166 pictures, which was obtained with the nominal scheduling with a time interval between pictures of 1 hour when not acquiring Doppler data (see section 2.2.1 Nominal scheduling above), no images are discarded after filtering, which means that at least one landmark is visible and well-lit in each image.

Furthermore, this filtering provides some useful information about the total number of images which contain a landmark that fulfils the visibility and illumination constraints. The resulting total number of images available for each landmark is shown in Figure 2.15.

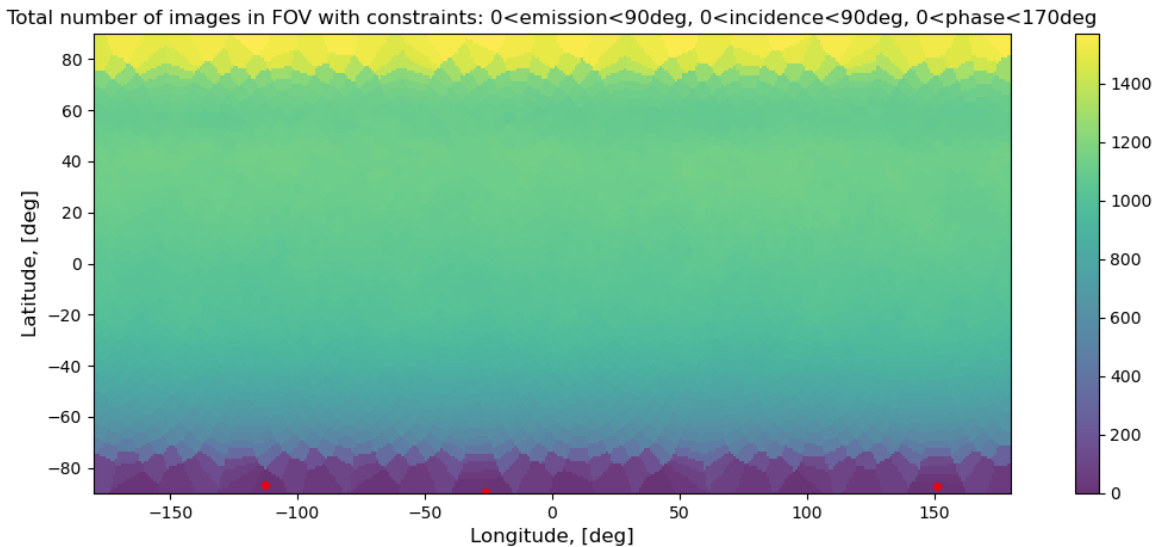


Figure 2.15: Total number of images which satisfy the minimum filtering based on visibility and illumination conditions for each of the 4000 landmarks considered. The total available images before filtering were 3166.

The depicted distribution has a granularity of 4000 landmarks, and the total number of available images mostly depends on the landmark’s latitude on the surface of Didymos. At the North pole, approximately half of the total collected images satisfy the minimum constraints, and this number is decreasing with the negative latitude. It is possible to see 3 landmarks (depicted with 3 red dots at the lowest latitudes) which do not satisfy the constraints: in particular, they never fulfill the maximum allowed incidence angle, which means that the Sun is always below the local horizon. However, it should be noted that even if for these 3 landmarks no images are available, in the end all the pictures survived this mild filtering, which means that all the images from the nominal scheduling setup

contain at least one visible and well-lit landmark.

### 2.2.2 Photometric model

Once the filtered timeline for optical observables is consolidated, the full database of images may be created by means of a photometric model.

The photometric model used in our analysis was considered for the Rosetta mission when targeting the comet 67P / Churyumov Gerasimenko. The described reflectance model is the one of McEwen Lunar [69], which has been properly modified and improved so that the real images collected during the mission could be fitted with respect to the output of the simulation. For the simulation of the pictures of Didymos, as a starting point we will assume the same parameters since both missions refer to small bodies with similar characteristics.

The photometric model provides the pixel signal intensity  $S$  expressed in digital units ( $DU$ ), and it can be modelled as [33], [60]:

$$S = a \cdot R(\alpha, i, e, \alpha_0, \beta_0) \cdot \Lambda(K_0) \cdot t_{int} + \phi \quad (2.5)$$

Where  $\alpha$  is the phase angle,  $i$  is the incidence angle,  $e$  the emission angle and:

- $a$  is the albedo of the surface of the shape model, which represents a pure scaling factor.
- $R$  is the reflectance function which describes the way the surface reflects the incident power, which only depends on geometric conditions.
- $\Lambda$  is a function that represents the contribution of the Sun at a distance  $d_{Sun}$ , expressed in  $DU/s$ .
- $t_{int}$  is the camera integration time in seconds.
- $\phi$  is the camera sensor background level in  $DU$ .

Three parameters need to be estimated in the described photometric model, which are the constants  $\alpha_0$ ,  $\beta_0$  and  $K_0$ :

- $\alpha_0$  is the angle which describes the transition from the two types of considered reflectance models (Lambert and Lommel-Seeliger).
- $\beta_0$  models the exponential decrease of the reflectance with the phase angle.
- $K_0$  contains the incident received power to be converted into  $DU$ . In the real case, if the albedo of the comet is not known, this parameter may absorb its actual value.

To a certain extent, the parameter  $K_0$  can absorb also other unmodeled factors, such as the spectral transmission of the optics.

The final image is then obtained by combining all the contributions provided for all the camera pixels.

### The reflectance function

The core of the photometric model is the **reflectance function**, which computes the reflectance associated with each pixel while imaging a particular object. The output reflectance matrix contains an uncalibrated version of the reprojected image of the surface of Didymos, which needs to be scaled in order to obtain the final expected image. With the model described in Equation 2.5, the total scaling is due to the albedo and other parameters independent of the considered pixel position, such as the integration time, the photon conversion efficiency factor and the Sun distance, which provides the reference incident photon flux on the surface.

To compute the reflectance matrix, we first need to understand how the shape model faces are geometrically reprojected onto the camera sensor, and this is done by mapping each sensor pixel position to each face direction expressed in the camera frame. The information required for performing the reprojection is:

- the relative position and attitude of the involved bodies
- the Hera AFC optical parameters, such as the focal length, pixel size, and pixel count, which can be extracted from the SPICE kernels.

In a simple approach, a pinhole model can be used, but in a real-case scenario the mapping should consider the optical distortions measured during the calibration of the camera optics.

After the geometric reprojection of the shape model of Didymos onto the camera sensor, the contribution that each shape model face provides to the pixel reflectance can be computed. In general, if a single reprojected shape model face is larger than a pixel, the pixel reflectance is provided entirely by that face. However, if the shape model resolution is sufficiently high, a pixel of the camera sensor may be mapped to many shape model faces. In that case, the reflectance of the pixel is computed as the joint contribution of all the effects provided by each face mapped to it, obtained from a function of the incidence, emission angles and albedo of the faces involved.

The model for the reflectance function used in the photometric model is the following:

$$R = P(\alpha) [(1 - L(\alpha)) R_L(i) + L(\alpha) R_{LS}(i, e)] \quad (2.6)$$

Where  $\alpha$ ,  $i$ ,  $e$  are respectively the phase, incidence and emission angles as defined in Figure 2.14. The reflectance model is comprised by a linear combination of a pure isotropically distributed diffusive term (Lambert reflectance,  $R_L(i)$  [59], [70]) together with a scattering function (Lommel-Seeliger reflectance,  $R_{LS}(i, e)$  [32]), where  $L$  is an exponential weighting function (the McEwen Lunar function) depending on the phase angle  $\alpha$ . The equations described above are:

- The Lambert reflectance:

$$R_L(i) = \cos(i) \quad (2.7)$$

- The Lommel-Seeliger reflectance:

$$R_{LS}(i, e) = \frac{\cos(i)}{\cos(i) + \cos(e)} \quad (2.8)$$

- The McEwen Lunar function:

$$L(\alpha) = e^{-\frac{\alpha}{\alpha_0}} \quad (2.9)$$

It should be noted that constant values present in the original formulas are omitted, so that they will be absorbed by the constant parameter  $K_0$ .

This type of description would consider a pure Lambert behaviour when  $\alpha = 0$  (so when the Sun is parallel to the line of sight of the camera), while its behaviour becomes more similar to Lommel-Seeliger in correspondence of larger phase angles.

The modification which allowed the Rosetta team to obtain simulations which could properly fit the real data was related to the addition of the new scaling factor  $P$ , function of the phase angle  $\alpha$ , that better fits the differential brightness experienced in the real data recorded by the camera sensor:

$$P(\alpha) = e^{-\frac{\alpha}{\beta_0}} \quad (2.10)$$

However, if the exponential is not sufficient to properly model the final computed brightness, it can be substituted with a different model, such as a polynomial phase function.

### The Sun contribution

If we consider the total emitted power of the Sun  $P_{Sun} = 3.86 \cdot 10^{26} \frac{J}{s}$ , the surface power density  $P_d$  at the distance  $d_{Sun}$  is:

$$P_d = \frac{P_{Sun}}{4\pi d_{Sun}^2} \quad (2.11)$$

This value can be converted to  $\frac{DU}{s}$ , considering a constant conversion factor  $K_{cam}$  for the AFC sensor, so that we obtain the function described in the photometric model:

$$\Lambda = P_d K_{cam} = \frac{K_0 K_{cam}}{d_{Sun}^2} \quad (2.12)$$

Where  $K_0$  is a constant value to be estimated which considers the total incident power provided by the Sun and eventually other absorbed constants.  $K_{cam}$  represents the constant conversion efficiency of incident power into the final quantized version expressed in  $DU/s$ . The computation required to fully characterize  $K_{cam}$  starts with the surface photon density received at the target distance. Correction factors are then applied for: the photon loss due to the transmittivity of the clear filter, the conversion efficiency between photons and photoelectrons on the sensitive surface of the pixel, and the conversion between collected photoelectrons and raw  $DU$  value.

### The camera integration time

In the photometric model, the camera integration time is a simple scaling factor and provides the total number of incident photons collected during the exposure. In order to capture properly exposed pictures, the camera integration time is the only parameter that can be modified, if we consider constant values of sensor gain and optical aperture, and during the acquisition phase its value should be defined in advance.

The optimal camera integration time should avoid saturation of the white levels, in order not to lose any precious details in the brightest areas of the picture, and expose to the right (ETTR), which means that the picture is at its maximum recorded brightness without overexposing, to make the most of the camera dynamic range. The method used in [60] is obtained by inverting the photometric model:

$$t_{int} = \frac{(S - \phi) d_{Sun}^2}{K_0 K_{cam} a_{max} R_{max}} \quad (2.13)$$

Where  $S$  is the desired pixel signal value expressed in  $DU$  and the max values of albedo and reflectance are defined, in that case, as:

$$a_{max} = 1.3 \quad (2.14)$$

$$R_{max}(\alpha) = P(\alpha) [(1 - L(\alpha)) \sin(\alpha) + L(\alpha)] \quad (2.15)$$

This method of computing the integration time has been proven valid within a specific range of target distances (100-400 *km*) and phase angles (60-120 deg) [3], where the computed value used for the real acquisition allowed to collect pictures that never reached the saturation condition.

These models are not meant to properly model the illumination condition when outside of a certain range of applicability, which can be stated being phase angles lower than 10 deg, incidence and emission angles larger than 60 deg. However, during the Rosetta mission, acceptable quality results were provided even considering phase angles in the range 0-130 deg and emission and incidence angles between 0-90 deg [63].

### 2.2.3 Simulation output

To sum up, the described photometric model is at the core of the image simulation, and it is used to compute how much each single face of the reference shape model affects the signal of the camera sensor pixels. At the very end, the final simulated images are created by providing:

- a database of camera positions, attitudes of camera, Sun positions in the Didymos body fixed reference frame.
- the shape model of Didymos, with an *a priori* value of albedo for all its faces.
- the camera integration times and other camera parameters.
- some estimated/fixed values for the free parameters present in the photometric model.

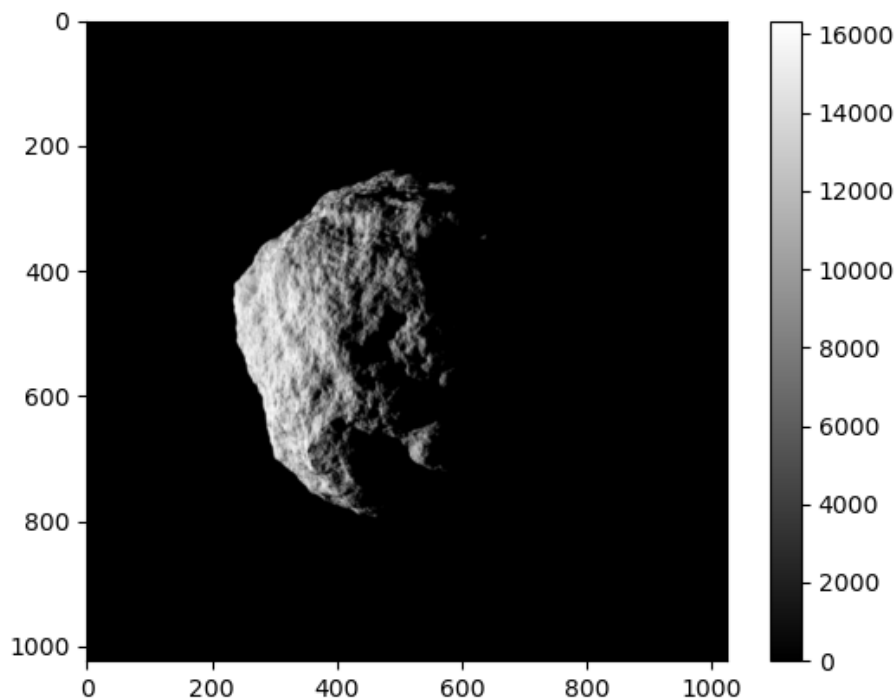


Figure 2.16: The output of the photometric model, stored in a FITS file. Gray levels expressed in  $DU$ .

This provides the final simulated matrix of pixel intensities, expressed in raw  $DU$  values. Considering the parameters of the AFC of Table 1.1, the output is a matrix of  $1020 \times 1020$  pixels, whose elements contain up to 14 bits/pixel of information (due to the quantization applied to the signal of the sensor), a value which is then meant to be stored in the Flexible Image Transport System (FITS) file format, which has a larger standard limit of 16 bits/pixel [71]. An example of the output of the method is provided in Figure 2.16. As it may be seen from the histogram of the image in Figure 2.17, there is an expected peak in the black levels due to the large number of dark areas. The white levels stay below the threshold value provided by the simulated sensor pixel's bit depth ( $2^{14}$ ), thus leading to no loss of details and providing the best SNR without having clipped pixels in the highlights.

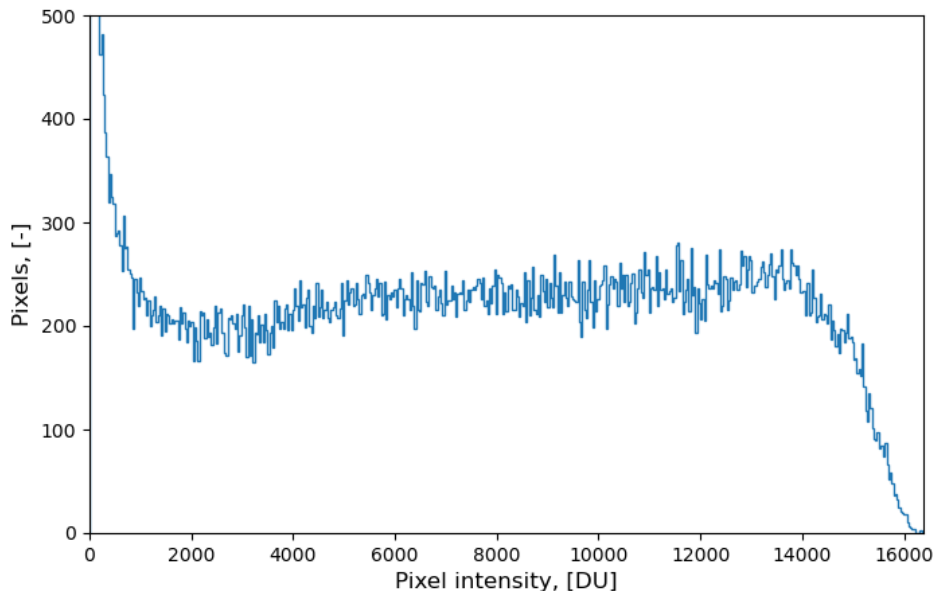


Figure 2.17: Histogram of FITS file, with bin size of  $2^{14}/500$   $DU$ . The maximum black value count (at 0  $DU$ ) exceeds the limit of the scale.

The quality of the images may impact the final outcome of the stereophotoclinometry in different ways, depending on the eventual mismodeling of the camera distortion, the presence of clipped regions, and non-linearities in the brightness recorded at the sensor. However, by using many pictures in the stereophotoclinometry process, the best-fit solution mitigates some of the errors introduced [72].

## 2.3 Maplets creation

The method proposed for optical observable extraction in the case of the Hera mission recalls the approach used for the navigation of Rosetta around the comet 67P / Churyumov Gerasimenko [63]. The method was previously introduced in [73], [33] and it is a

stereophotoclinometry technique capable of extracting height maps (or maplets, see Figure 2.18) from a series of input images and landmark positions defined for convenience in the body fixed reference frame of the target. Then, the stereophotoclinometry method can be combined with stereophotogrammetry techniques to obtain further improvements [60].

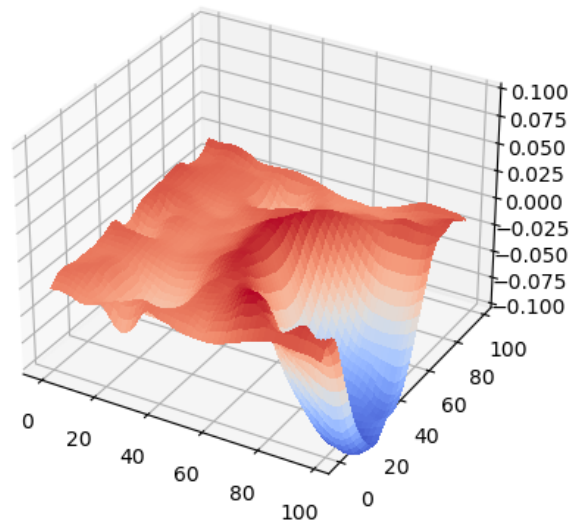


Figure 2.18: Maplet of a generic landmark, generated from a controlled series of fits files containing the same target under different illumination conditions.

The method for reconstructing height information from differently lit pictures containing the same landmark is described in detail in [60]. In the case of the Hera mission, the steps involved are depicted in Figure 2.19, where the *a priori* normal of the surface close to the considered landmark is extracted and used as a guess value for the Z direction of the maplet.

The input for the creation of a single maplet of a landmark is a series of pictures in which the landmark is visible. Therefore, the database of pictures obtained by the image simulation step is filtered per landmark, so that only the useful images are fed into the maplet creation step. The accuracy of the stereophotoclinometry is affected by different criteria [74], and the filtering here considered takes into account the following constraints, which are described in detail in the following sections:

- Landmark on the proper side of the asteroid (based on emission angle).
- Landmark properly lit (based on phase and incidence angles).
- Landmark in the field of view.
- Landmark at an optimal distance.

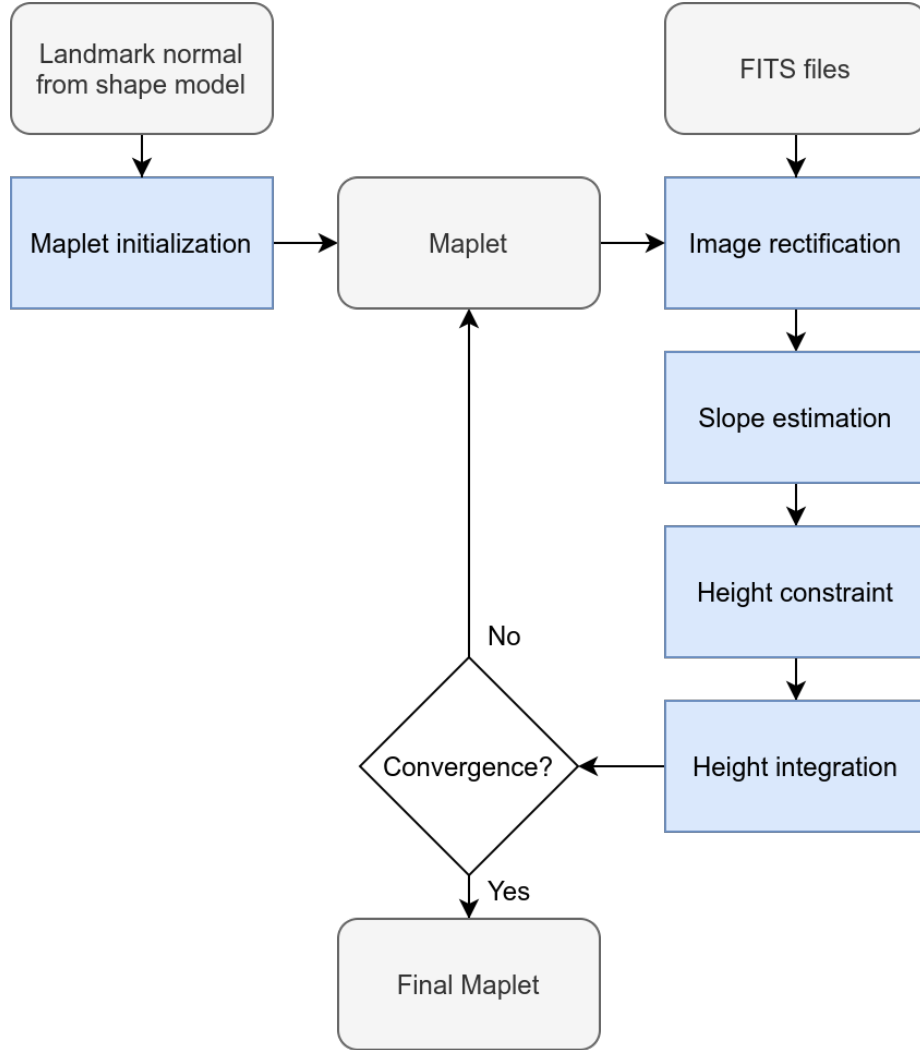


Figure 2.19: Maplet creation pipeline.

### 2.3.1 Visibility constraints

#### Landmark on the proper side

A landmark is placed on the proper side of the asteroid with respect to the observer if  $\gamma > \frac{\pi}{2}$ , which is the angle formed by the AFC, the landmark position, and the geometric center of the asteroid, as shown in Figure 2.20. This formulation with the angle  $\gamma$  is useful to avoid some false positives when the considered shape is not a perfect sphere.

In fact, another expression for this constraint is based on the emission angle  $e$ , as it is shown in Figure 2.21, where we have that it should always be that  $e < \frac{\pi}{2}$ .

Alternatively, we can use the scalar product between local landmark normal  $\mathbf{n}$  and camera direction, and set it to be positive:

$$(\mathbf{c} - \mathbf{LM}) \cdot \mathbf{n} > 0 \quad (2.16)$$

Where  $\mathbf{c}$  is the position vector of the AFC in the asteroid's body-fixed reference frame, and  $\mathbf{LM}$  is the landmark position expressed in the same frame. However, this may be satisfied even on the part of the asteroid which is out of view if the surface has locally a normal with a component in the direction of the camera. An advantage of this constraint on the emission angle is to arbitrarily discard the landmarks characterized by the AFC at too low local elevation angles, which otherwise would lead to excessively distorted images once reprojected in the image rectification step.

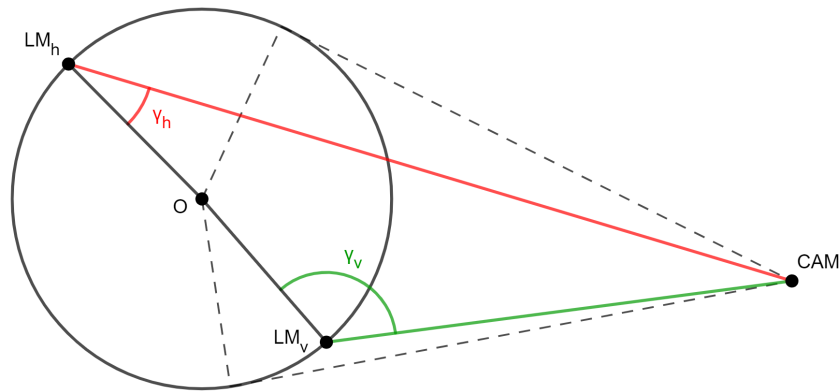


Figure 2.20: Visibility constraint based on the relative position on the asteroid.

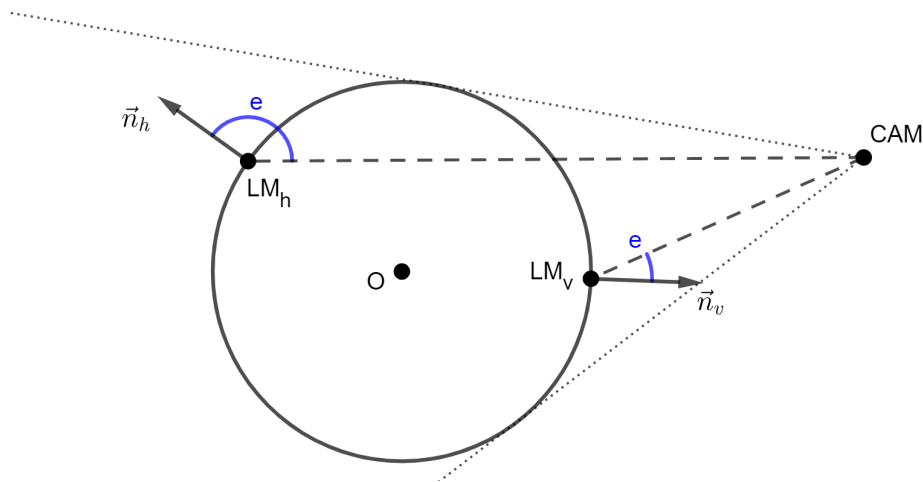


Figure 2.21: Visibility constraint with emission angle.

### Landmark properly lit

Landmarks are properly lit if  $i < \frac{\pi}{2}$ , where  $i$  is the incidence angle between local landmark normal  $\mathbf{n}$  and the Sun direction  $v_{Sun}$ , see Figure 2.22. If we consider the camera direction

(which is the emission angle) in addition to the incidence angle, it is possible to extend this filtering based on a desired range of phase angles.

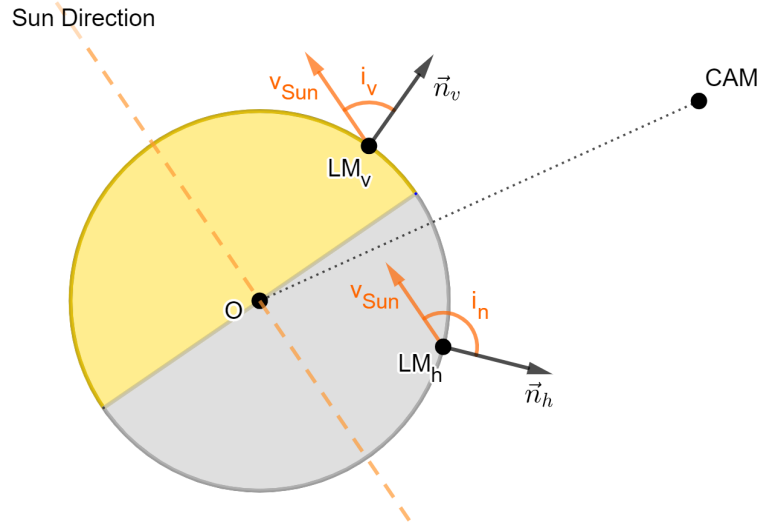


Figure 2.22: Filtering based on illumination conditions.

The described constraints may be further tailored with respect to the values presented, in order to obtain better inputs for the analysis. In fact, a landmark seen with an emission angle of almost 90 deg provides a distorted image, which, once reprojected, leads to interpolated results with a huge loss of illumination details. The same applies for the illumination condition based on the incidence, which will provide an excess of dark pixels due to the local slopes and height features if the value is close to 90 deg. Considering again the incidence angle, if it is too close to 0 deg, most of the shadow information is lost. A similar condition applies for the phase angle when the Sun direction is close to the camera direction and the shadows disappear. Therefore, we can consider different values for filtering, such as a minimum filtering that retains most of the images, a mild filtering, a medium filtering, and a strict filtering with the best geometric and illumination conditions. The limit values chosen for the photometric angles are depicted in Table 2.3, where  $e$  is the emission angle,  $i$  is the incidence angle, and  $\alpha$  is the phase angle.

Table 2.3: Photometric angles' limits for different filtering levels.

$e$	$i$	$\alpha$	<b>Filtering level</b>
[0, 85] deg	[5, 85] deg	[10, 170] deg	minimum
[0, 75] deg	[5, 75] deg	[10, 170] deg	mild
[0, 65] deg	[5, 65] deg	[10, 170] deg	medium
[0, 55] deg	[5, 55] deg	[10, 170] deg	strict

The considered filtering provides a different number of images available for each land-

mark, as depicted in Figure 2.23, Figure 2.24, Figure 2.25, and Figure 2.26. In these figures, it can be seen that there is a region where the best conditions are met, which is approximately located within the latitude range that spans from  $-40$  deg to  $+60$  deg at all the longitude values.

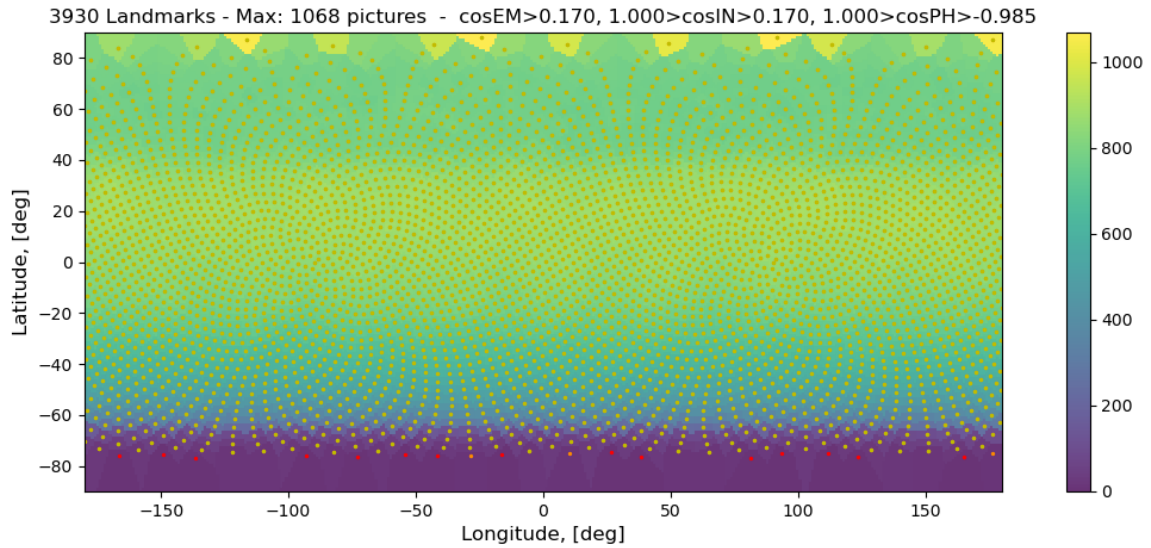


Figure 2.23: Minimum filtering based on photometric angles.

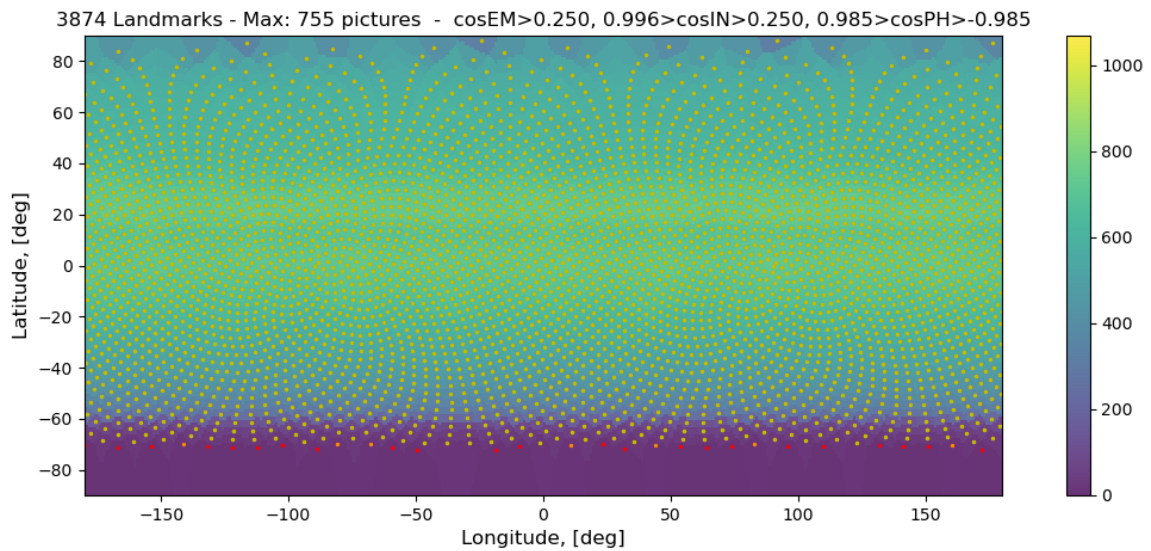


Figure 2.24: Mild filtering based on photometric angles.

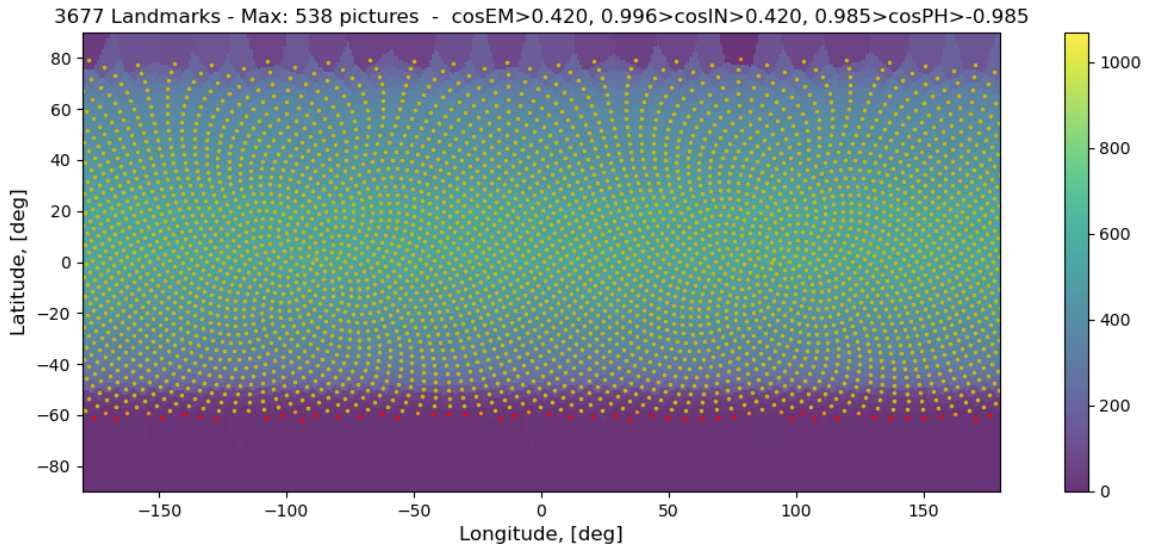


Figure 2.25: Medium filtering based on photometric angles.

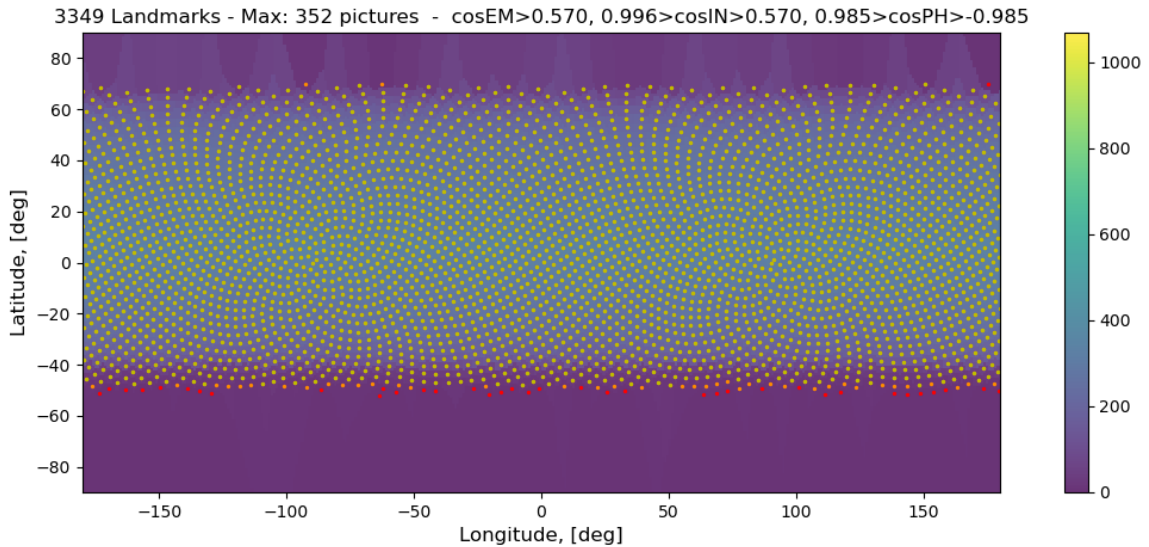


Figure 2.26: Strict filtering based on photometric angles.

In the figures, all the dots represent the landmarks which have at least one image which survived the filtering. In red are the landmarks for which 1 to 4 pictures are available, in orange the ones for which 5 to 9 images are available, and in yellow the ones for which 10 or more images are available. The total number of landmarks described in the titles consider the landmarks which have at least 10 images available.

It should be noted that this filtering based on the photometry angles is not considering the field of view constraint and the optimal distance. Therefore, for the maplet creation it is also required to check the distance of the considered landmark from the camera position.

### Landmark in field of view

Landmarks are in the field of view if  $\theta < \frac{FOV}{2}$ , where  $\theta$  is the angle formed by the landmark position, the AFC position and the AFC boresight, as shown in Figure 2.27. Since we assume the camera to always be nadir-pointing towards Didymos, this constraint ensures that landmarks which are on the proper side of the planet but outside the FOV are filtered. This may happen when the spacecraft is sufficiently close to the asteroid and only a portion of it is in sight. This filtering is independent of the shape of the asteroid considered, but only of the landmark position.

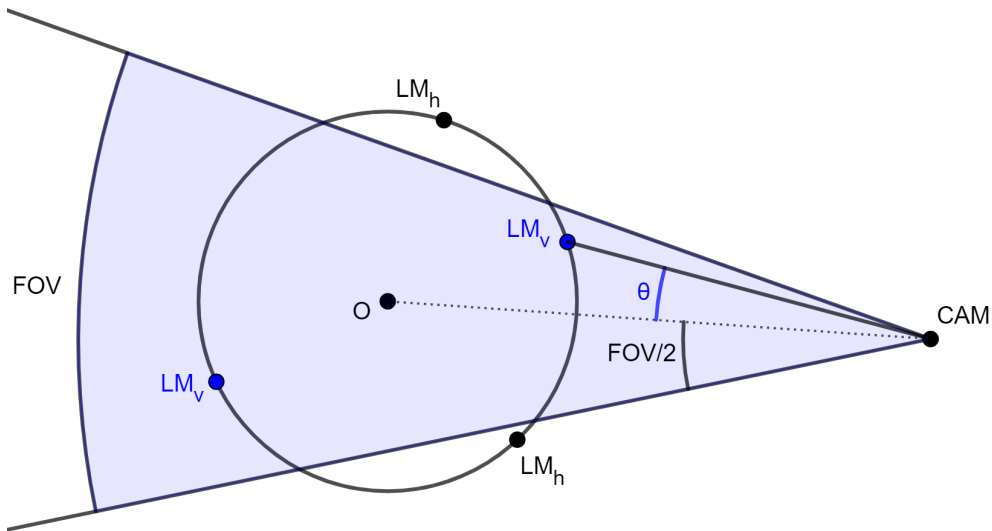


Figure 2.27: Visibility constraint based on field of view.

### Landmark at an optimal distance

This is a constraint which is based on the dimension chosen for the maplet to be created. A landmark is at an optimal distance when the pictures have the dimension of the reprojected maplet pixel or cell size comparable to size of the AFC pixel, which is described as  $p$  in Figure 2.28. A certain amount of tolerance between the relative size of maplet pixel and camera pixel is allowed; in literature the suggested value is between one-third to three times the reference camera pixel size. The limits of the method were stressed and it was demonstrated that it is possible to create maplets from pictures taken at distances larger than the optimum value (up to a factor of 4.2 with respect to the reference pixel dimension) [63]. Considering a reference distance  $d$  for which the maplet cell dimension is reprojected with size  $p$ , the optimal value for maplet creation is in the range  $[d_{min}, d_{max}]$ . In fact, considering the pinhole description of Figure 2.29, where:

- $f$  is the focal length of the pinhole camera, in units of length.
- $\alpha$  is the half field of view (FOV) angle of the camera sensor.

- $sizeCCD$  is the physical dimension of the sensor, in units of length.
- $pixelCCD$  is the physical dimension of a single sensor pixel, in units of length.
- $d$  is the distance at which the subject of the image is located (such as Didymos' surface), in units of length.

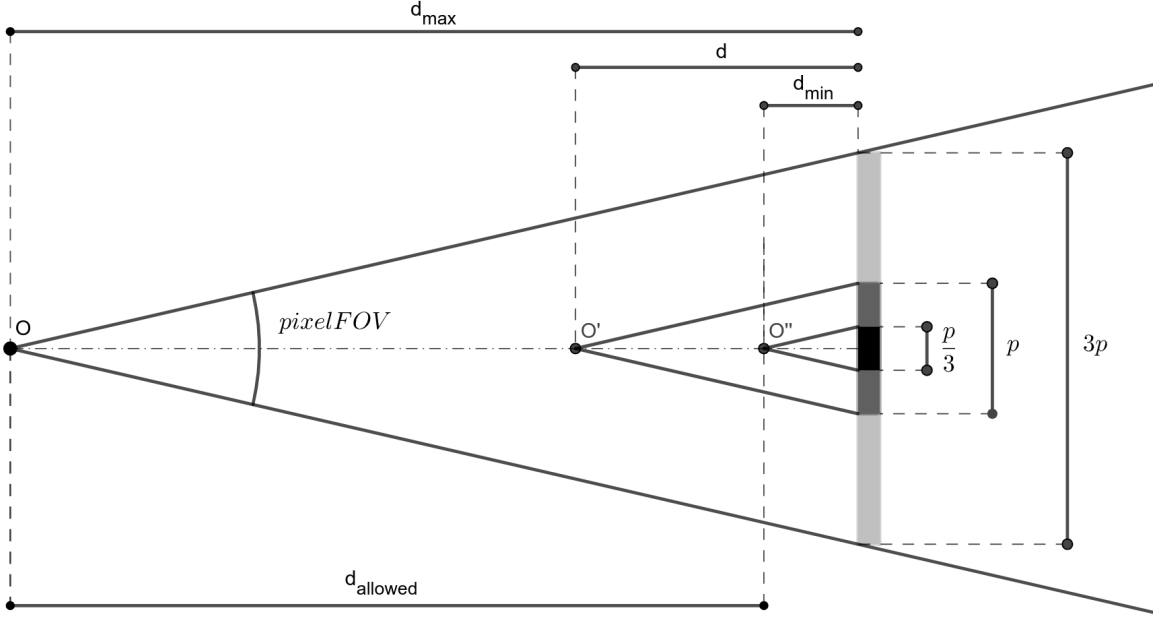


Figure 2.28: Allowed range of distances to create a maplet with cell size  $p$ .

It is possible to get the formulation for the optimal maplet size as a function of the distance from the AFC:

$$pixelMaplet = \frac{d}{f} \cdot pixelCCD \in \left[ \frac{1}{3}, 3 \right] \cdot pixelCCD \quad (2.17)$$

In fact, given the field of view as:

$$FOV = 2\alpha \cong \arctan \left( \frac{sizeCCD}{f} \right) \quad (2.18)$$

The pixel FOV (IFOV) angle is:

$$IFOV \cong \arctan \left( \frac{pixelCCD}{f} \right) \equiv \arctan \left( \frac{pixelMaplet}{d} \right) \quad (2.19)$$

Where, remembering that the AFC has a total number of pixels  $n_{pixels} = 1020$  for each side:

$$pixelCCD = \frac{sizeCCD}{n_{pixels}} \quad (2.20)$$

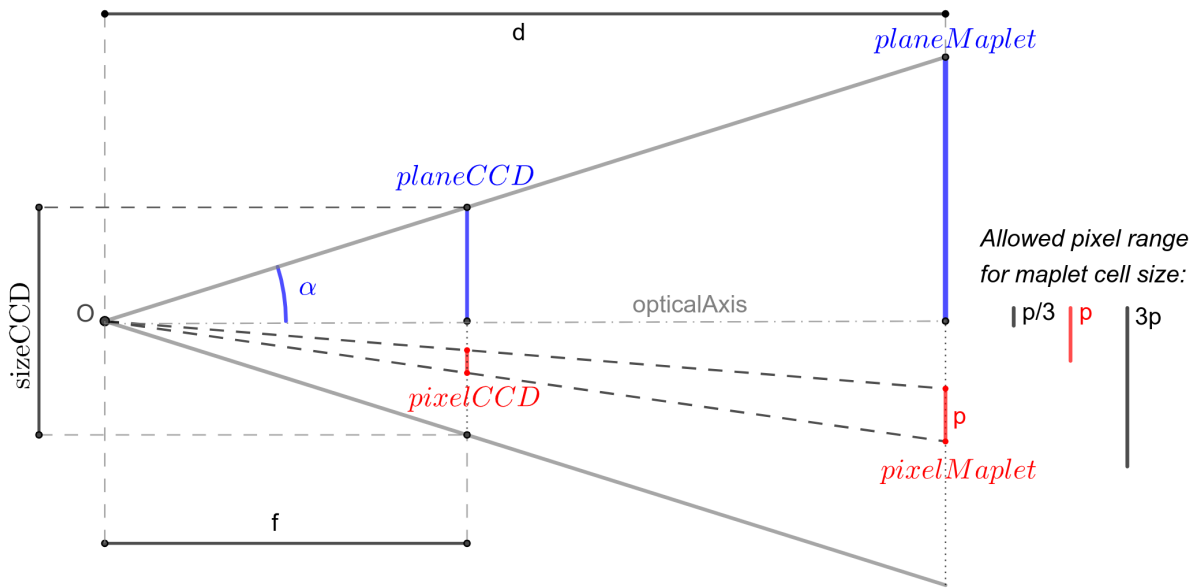


Figure 2.29: Pinhole camera model and allowed maplet cell size.

Considering Figure 2.23, Figure 2.24, Figure 2.25, and Figure 2.26, we can now add to the filtering the constraints related to landmarks being in the field of view and the camera being at an optimal distance for the creation of maplets of a given size. In our case we are considering maplets with lateral dimensions of  $40\text{ m}$  on each side. The total number of available pictures is drastically reduced after these filtering, and largest effect on the resulting available pictures for each landmark is the limit imposed on the distance between camera and landmarks. These effects are depicted in Figure 2.30, Figure 2.31, Figure 2.32, and Figure 2.33 (which can be compared with the previous filtering provided in Figure 2.23, Figure 2.24, Figure 2.25, and Figure 2.26).

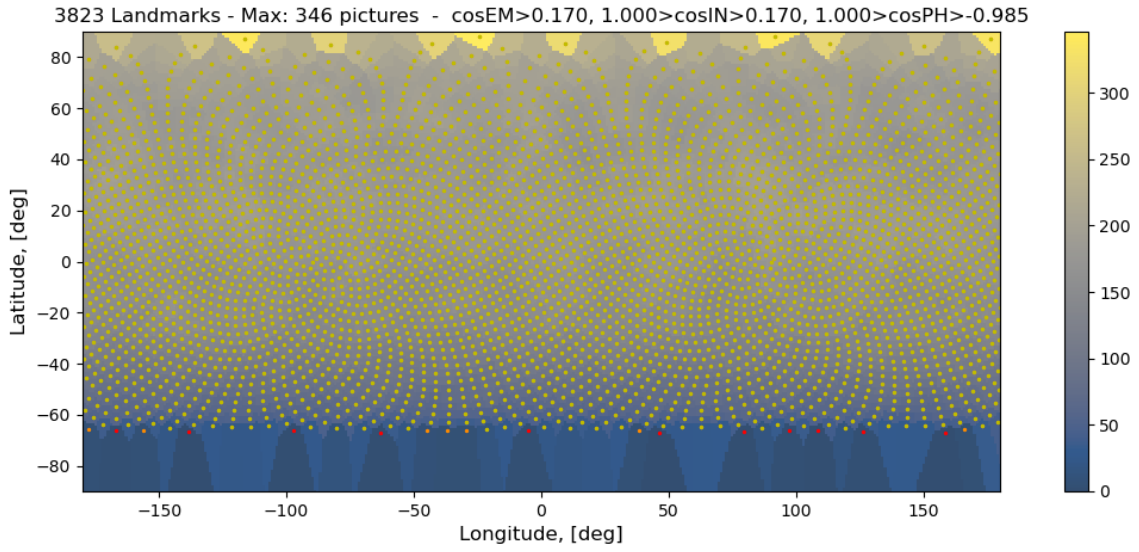


Figure 2.30: Minimum filtering based on photometric angles, landmarks in FOV and camera at an optimal distance.

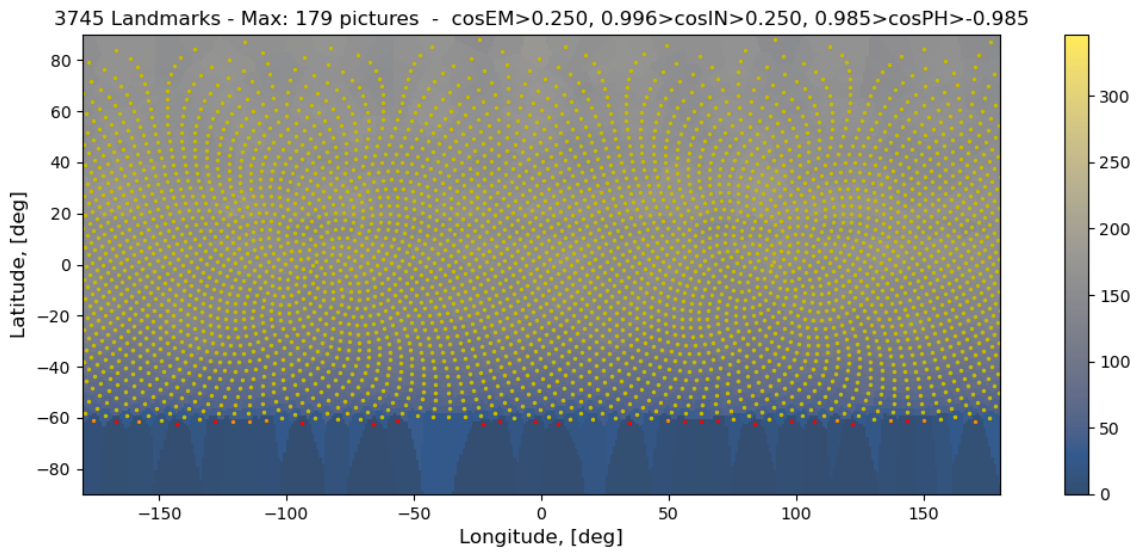


Figure 2.31: Mild filtering based on photometric angles, landmarks in FOV and camera at an optimal distance.

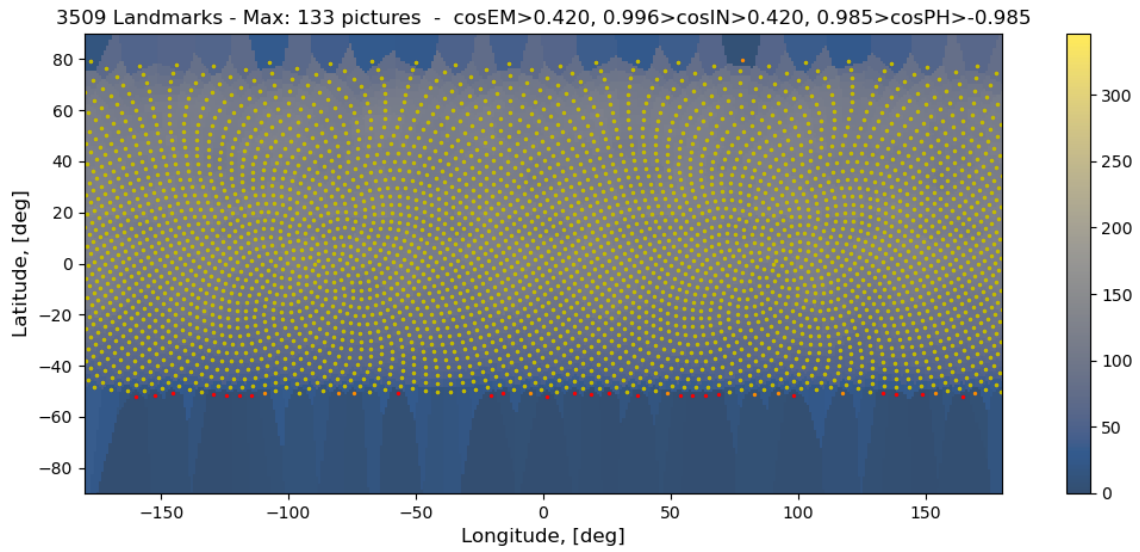


Figure 2.32: Medium filtering based on photometric angles, landmarks in FOV and camera at an optimal distance.

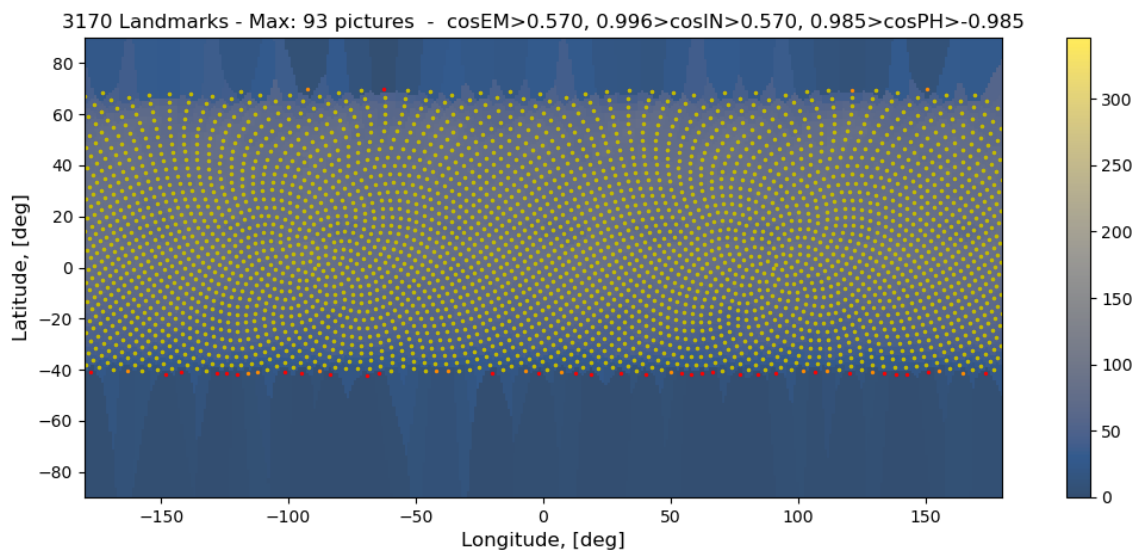


Figure 2.33: Strict filtering based on photometric angles, landmarks in FOV and camera at an optimal distance.

In red and orange are the landmarks for which less than 5 and 10 images are respectively available, while in yellow are the landmarks for which at least 10 images fulfill all the requirements (in terms of photometric angles and conditions based on in field of view and optimal distance).

### 2.3.2 Maplet initialization

At the first iteration, the maplet is initialised as a 2D matrix of fixed dimensions, in our case it is composed by  $99 \times 99$  cells. Regarding the maplet initial height content, the *a priori* shape model can be used as a starting point to fill in the maplet content, however this is not strictly necessary and even a matrix initialised as a flat plate can reach final convergence.

The maplet reference frame has the origin in the middle of the matrix of heights and corresponds, by definition, to the landmark position in the Didymos body fixed reference frame. The attitude of the maplet may be defined in arbitrary ways, depending on the *a priori* input information:

- If no *a priori* information is available, the maplet attitude is related to a flat surface whose normal direction  $Z$  is parallel to the radial direction described by the landmark position, thus considering a simple spherical model for the body.
- If an *a priori* knowledge of the surface is available, such as in our case (see Figure 2.2), for the  $Z$  direction we can consider the landmark's local normal, which is computed as the normal of the plane which best fits the polyhedron's vertices surrounding the landmark position.

For the purpose of maplet creation, it is not particularly relevant how the  $X$  and  $Y$  directions are chosen; we can consider the East and North directions as  $X$  and  $Y$  components forming a right-handed frame, where the North direction is aligned with the pole of the asteroid.

This frame provides the attitude of the maplet with respect to the Didymos body fixed frame, which is required for the following image rectification step. At each step of the maplet creation, a new guess for the height map is provided, so that a new value for the local normal is computed.

### 2.3.3 Image rectification

To create the maplet for the landmark, we need to extract the part of the pictures taken by the AFC which contain it [63]. In general, the pixels related to the maplet cell positions need to be reprojected, due to the landmark not being seen always from nadir, and the image is required to be undistorted prior to proceeding with the height estimation.

This rectification process provides a view of the landmarks as if they were seen from the local normal direction of the corresponding maplets they are referred to. In the simplest case, a pinhole camera model can be used for the undistortion process, while for images collected from a real camera, one should also consider the lens distortion parameters in the conversion between the direction of the camera frame and the corresponding pixel

position in the sensor.

The geometric rectification to undistort the images is possible if the following information is available:

- The camera position and attitude in the target's body frame is known, which in our case is extracted from the integrated spacecraft and asteroid trajectories. A correct reprojection is dependent on the knowledge of the camera attitude in the frame of reference in which the landmarks are defined, which in our case is the Didymos body fixed reference frame.
- The attitude of the maplet corresponding to the considered landmark in the target's body frame is known with a certain degree of accuracy, since it was initialized in the previous step. The larger the error, the worst the reprojection of the maplet from a camera picture.
- The mapping between the direction of the target in the AFC reference frame and pixel position is known (through a pinhole model).

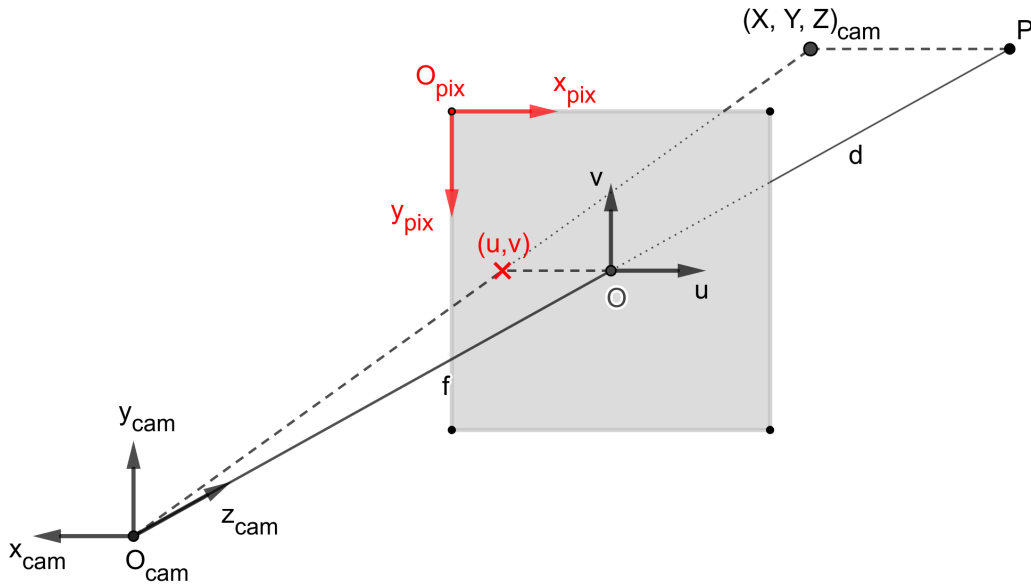


Figure 2.34: Pinhole reprojection of a point into the sensor pixel location.

To obtain the camera direction to pixel mapping, we consider a point with coordinates  $(X, Y, Z)_{cam}$  expressed in the AFC frame, whose  $Z$  direction corresponds to the boresight, as shown in Figure 2.34.

The intersection of the direction of this point with the sensor plane (depicted as the  $O(u, v)$  reference frame, and placed at a distance  $f$  along the camera boresight) is given by:

$$(u, v)_O = \left( \frac{X}{Z}f, \frac{Y}{Z}f \right) \quad (2.21)$$

Where  $X/Z$  and  $Y/Z$  represent respectively the directions of the point along  $x$  and  $y$  in the AFC frame. The value of  $(u, v)_0$  expressed in meters, can be converted to pixel coordinates (where, by definition, we consider  $x$  as samples and  $y$  as lines) considering the pixel dimension, which we assume equal for both  $x$  and  $y$  directions:

$$(u, v)_{pix} = \left( \frac{X}{Z} \frac{f}{p_{size}} - c_u, \frac{Y}{Z} \frac{f}{p_{size}} - c_v \right) \quad (2.22)$$

Where  $c_u, c_v$  are the pixel positions in sample and line of the principal point of the camera ( $O$ ),  $p_{size}$  is the pixel dimension in meters and the sign for  $c_u$  and  $c_v$  depends on the convention adopted in Figure 2.34. Considering many images with different illumination and geometric conditions, an example of the result of the maplet reprojection is shown in Figure 2.35. These images are the final output of all the iterations and were obtained starting from a simple flat plate description of the initial maplet with the attitude provided by the reference scientific model at low resolution, which is our best knowledge of the shape to date.

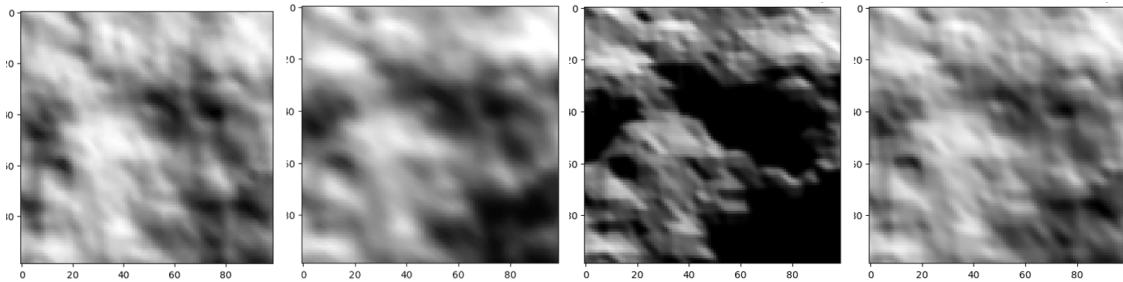


Figure 2.35: Reprojected images of a landmark with different illumination conditions.

The maplets do not need to be created from the whole set of images collected during the mission, but a subset of them with the best lighting conditions is chosen. Considering a dataset of pictures which has been properly filtered by the distance of the camera to create a maplet of given cell dimension, then the maplets will only cover a small portion of the total image of  $1020 \times 1020$  pixels and can usually be entirely reprojected, except for the landmarks really close to the borders of the picture.

The next step will combine these maplets with an albedo map and a photometric model, after proper geometric reprojection, in order to simulate the expected camera view at any arbitrary geometric condition.

### 2.3.4 Slopes estimation

Once all the images of a single landmark have been rectified, it is possible to estimate both the slopes and albedo at the same time using a stereophotoclinometry technique, as described in [73], which comprises a linear least squares solver. This method provides

valid results if the initial knowledge of the relative positions of camera and attitude of the maplets are known with a certain degree of accuracy. Otherwise, the precise reprojection needed for slope reconstruction may be too off due to parallax effects.

Given a surface  $F(x, y, z) = 0$ , the gradient computed at a point  $(x, y, z)$  provides the local normal:

$$\mathbf{n} = \nabla F(x, y, z) \quad (2.23)$$

In the case of a maplet, the surface  $F$  may be described as  $z - h(x, y) = 0$ , thus the normal becomes:

$$\mathbf{n} = \left( \frac{\partial(z - h(x, y))}{\partial x}, \frac{\partial(z - h(x, y))}{\partial y}, \frac{\partial(z - h(x, y))}{\partial z} \right) \quad (2.24)$$

Considering the slopes as the components of the gradient of the height profile  $h(x, y)$  expressed in the reference frame of the maplet:

$$t_1 = \frac{\partial h(x, y)}{\partial x} \quad ; \quad t_2 = \frac{\partial h(x, y)}{\partial y} \quad (2.25)$$

The normal vector of a single maplet cell in the maplet reference frame becomes:

$$\mathbf{n} = (-t_1, -t_2, 1) \quad (2.26)$$

Even if the maplet is initialized as a flat plate, we may express the photometric angles of emission and incidence for each maplet cell, since the camera position with respect to the frame of the maplet and the Sun direction are known; in fact, we have:

$$\cos(i) = \frac{\mathbf{n} \cdot \mathbf{s}}{|\mathbf{n}| |\mathbf{s}|} \quad (2.27)$$

$$\cos(e) = \frac{\mathbf{n} \cdot \mathbf{c}}{|\mathbf{n}| |\mathbf{c}|} \quad (2.28)$$

Where  $\mathbf{s}$  and  $\mathbf{c}$  are respectively the Sun direction and camera position computed in the maplet reference frame. In this way, we can write the angles as a function of the slopes:

$$i = i(t_1, t_2) \quad (2.29)$$

$$e = e(t_1, t_2) \quad (2.30)$$

For each rectified picture used for the maplet creation, as they are depicted in Figure 2.35, it is possible to express the signal of each pixel by means of the photometric model previously introduced. The pixel signal intensity of Equation 2.5 has the reflectance

function which can now be described as a function of the slopes:

$$R = R(\alpha, t_1, t_2, \alpha_0, \beta_0) \quad (2.31)$$

In this way it is possible to solve the photometric equation in each pixel for the unknowns (the albedo and the slopes) using a linear least squares method. This requires a minimum of three rectified images, and it has to be noted that we need a filtering on the cells which are in shadow before performing the step of slope estimation (since dark cells do not contain height information).

### 2.3.5 Height constraints

The desired height profile  $h(x, y)$  is obtained by integrating the slopes estimated in the previous step. However, a reference constant height value for the integration needs to be determined, to get the true solution.

A guess value for the constant of integration can be retrieved by means of different methods; in this study a technique based on anchor points is considered, as described in [60]. This method requires the selection of a series of locations in the maplet, the anchor points, whose position is extracted by means of stereophotogrammetry [75], thus providing a location in full three dimensions.

As a first step, each of the original rectified images used to create the maplet is compared to the simulated version of themselves, which can be created from the albedo and slopes information obtained in the slope estimation step.

The anchor points are selected in the maplet, and their position may be assessed with high accuracy in the simulated pictures by correlating the part of the image which is expected to contain them. The output of this step is the pixel position of the anchor point in each of the rectified images, which corresponds to a direction in which the point is expected to be located. However, if the initial offset introduced with the reprojection was too large, at this step we do not expect to find a proper correlation, and a new guess value for the position of the maplet and/or attitudes of the cameras should be considered.

Once the pixel positions of the chosen anchor points (and therefore, the directions in the camera frame) are available for many different pictures, it is possible to assess the 3D coordinates of each anchor point (the point  $P$  in Figure 2.36 represents a typical scenario in which the anchor point position is extracted from the original images, before applying any rectification). The frame in which the anchor points are found is the same frame where the camera positions are defined, thus it is possible to express that value on the maplet frame and use it as a height constraint.

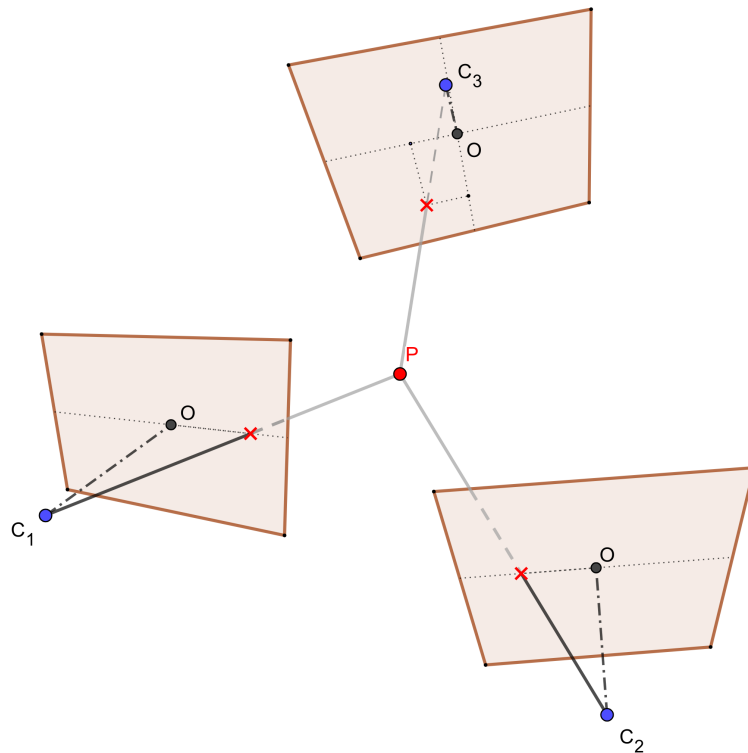


Figure 2.36: Classical photogrammetry technique to extract 3D location of a point from multiple pictures.

### 2.3.6 Height integration

Starting with an initial guess value for the height of the anchor points, together with the full estimated albedo and slopes maps, a least squares algorithm is used to compute the height values for all the maplet cells. Many methods can be used, such as Fourier filtering, path integration, local integration or the one adopted, which is the direct solution of a linear system, by means of a least squares method for sparse matrices [76]. The linear system to be solved is [60]:

$$\begin{cases} h_{0i,j} = h_{i,j} \\ t_{1i,j} = \frac{h_{i-2,j} - 4h_{i-1,j} + 3h_{i,j}}{2s} \\ t_{2i,j} = \frac{h_{i,j-2} - 4h_{i,j-1} + 3h_{i,j}}{2s} \end{cases} \quad (2.32)$$

Where  $s$  is the size of a maplet cell,  $i, j$  the indices of the cells, and the slopes  $t_1$  and  $t_2$  are defined through a numerically stable second order retarded/backward difference approximation. The relative uncertainties in  $h$ ,  $t_1$ , and  $t_2$  can be added as weights to this equation.

The final output of the method, using a set of pictures where Figure 2.35 is a subset of

the full list used, leads to the result in Figure 2.37. In this case, we considered a maplet with 50  $m$  of lateral size, which represents a landmark on top of the high-resolution model of Didymos.

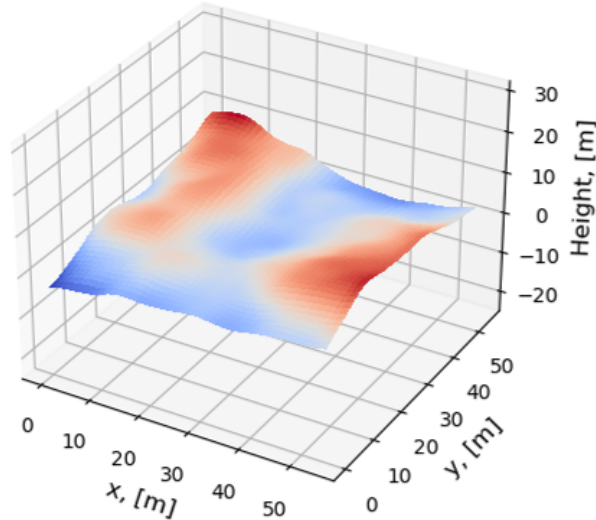


Figure 2.37: Maplet output of the method.

For comparison, Figure 2.38 depicts a generic flat plate with the same dimensions as the maplet in Figure 2.37. It is clearly shown that the level of detail in the final estimated maplet increased with respect to the *a priori* low-resolution polyhedral shape model. The method could converge thanks to the iterative correction of the radial position of the landmark, given an uncertainty in the original position (given by the difference between low-resolution and high-resolution polyhedral shape models) having the same order of magnitude as the maplet's lateral size.

Since in our simulated environment the high-resolution shape model is available, it is possible to place one of the generated maplets on top of the original shape model, so that a visual feedback of the reconstructed maplet can be assessed (see Figure 2.39).

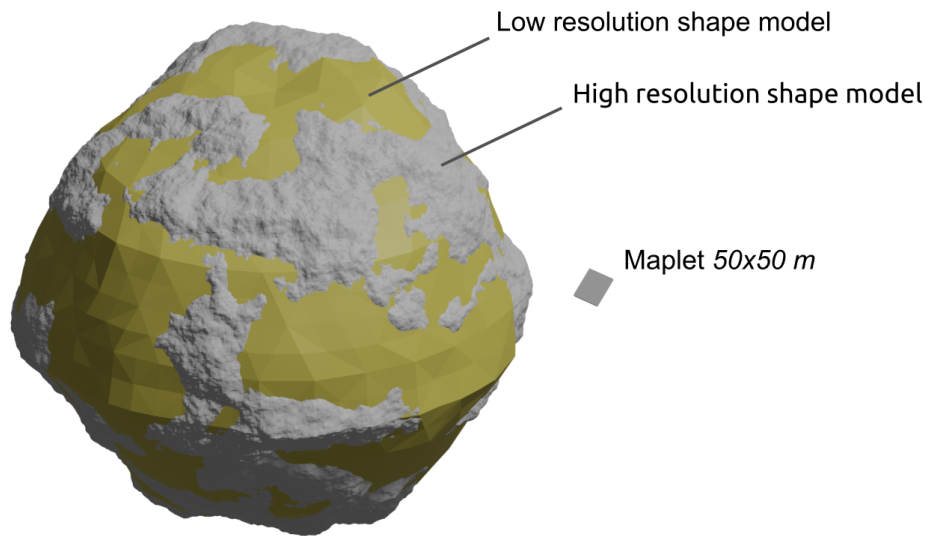


Figure 2.38: A maplet on the same scale as the original model used for initialization (in yellow). The superposed augmented version (in grayscale) was only used for the creation of the input images.

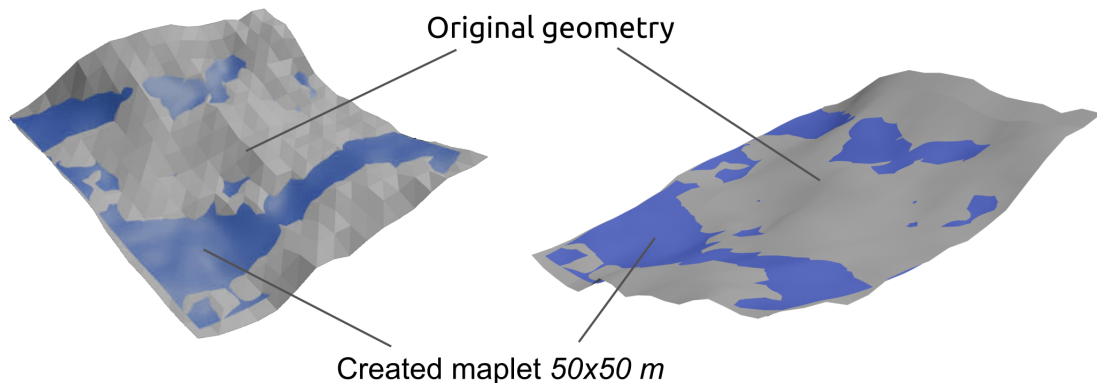


Figure 2.39: The created maplet (blue) and the corresponding region in the original high-resolution shape model (in gray).

As it can be seen, the maplet is created in the expected position, and it is coherent with the original high-resolution geometry used only to create the input images as FITS files. A detailed description of the error between the created maplets and the original high resolution shape models is show in chapter 3 in Figure 3.1.

## 2.4 Observables extraction through maplet matching

In order to extract the observables of the landmark position from the images of the AFC, it may be required to have an initial correction of the camera position and attitude with

respect to the target for each single picture, if the uncertainty in their computed values is too large for the maplet matching method.

A first order correction is applicable if maplets were created in advance starting from a different set of images characterized by low uncertainty about the spacecraft's state and attitude. These maplets can be reprojected onto a blank frame of the dimension of the AFC sensor (as in Figure 2.40, middle and right images), considering proper photometry and illumination conditions, to provide an expected picture to be compared with the real one. The difference between center and right images is the dimension and total amount of the maplets, thus providing very different visual results.

Then, a cross correlation between the real picture (Figure 2.40, left) and the one obtained from the reprojected maplets can be computed, providing a rough correction in terms of camera pointing or position. However, it is not necessary that the entire object is covered by maplets, since only the non-zero valued signals are considered in providing the final correlation value. As a first approximation, the correction computed from the correlation can be considered as a shift on the AFC sensor's plane; once the shift is applied to the real image, it still has a small residual offset but it is enough to enable the precise maplet matching [63].

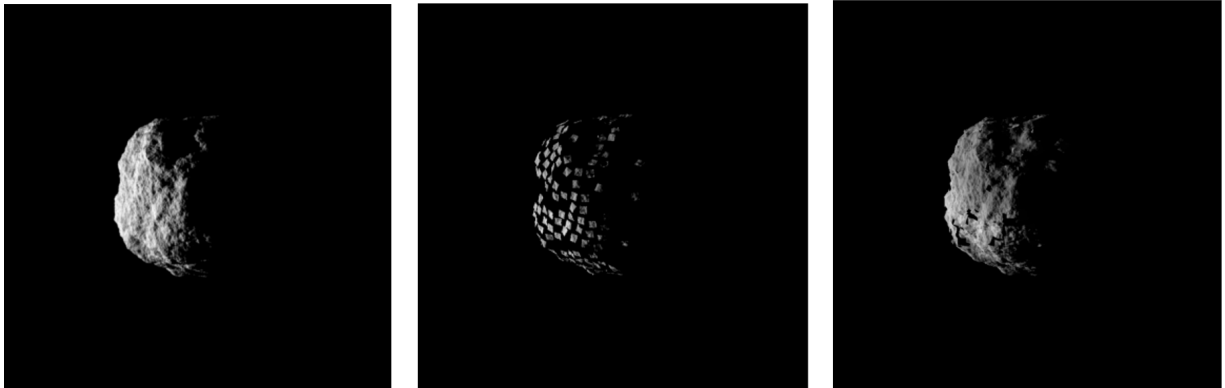


Figure 2.40: From left to right, the image simulated from the high-resolution polyhedral model; a partial reconstruction of the original image using a sparse set of maplets; a simulated version with more maplets of larger size.

After the eventual correction, the maplet matching method can be started. This is a step which allows the extraction of optical observables, thanks to a correlation between a top view of the maplet, whose illumination is simulated by means of a photometric model, and a corresponding reprojected picture of the AFC.

The input for automatic maplet matching is a maplet of a landmark and the real Hera AFC picture of the target body (Figure 2.40 on the left), which contains the desired landmark for which we want to extract the optical observable. The presence of a landmark in a picture may be easily assessed from geometric constraints if the positions and attitudes of Didymos and Hera AFC are known with an adequate degree of accuracy.

Once a proper picture is selected, a step of reprojection is performed, in order to obtain a rectified version of the region containing the maplet pixels. The rectified image is then compared to a synthetic version of the maplet, where the photometric model is applied considering the same expected geometric conditions present in the real picture. The result is a couple of images which have, in theory, the same brightness value content, if the photometric model was providing a good approximation of the expected illumination conditions, and a slight displacement, if the relative positions and attitudes were approximately the same.

Since those pictures depict the same region with equal illumination conditions, a simple cross correlation can be applied to extract the relative displacement present between the two pictures. The offset value is obtained by the normalized cross correlation measurement described in [77], which can be computed with different efficient techniques [78], [79]. The formulation used is:

$$\rho = \frac{\sum_i \sum_j (S_{i,j}^o - \bar{S}^o) G(r)}{\sqrt{\sum_i \sum_j (S_{i,j}^o - \bar{S}^o)^2 G(r)}} \cdot \frac{\sum_i \sum_j (S_{i,j}^s - \bar{S}^s) G(r)}{\sqrt{\sum_i \sum_j (S_{i,j}^s - \bar{S}^s)^2 G(r)}} \quad (2.33)$$

The sum is over the indices  $i, j$  which are the maplet cell indices,  $S^o$  and  $S^s$  are respectively the signals of each maplet cell for the original rectified image and for the simulated picture from the maplet,  $\bar{S}^o$  and  $\bar{S}^s$  are the mean values of the signals of the entire image. The Gaussian distribution:

$$G(r) = e^{-\frac{r^2}{2\sigma^2}} \quad (2.34)$$

Is a function of the distance  $r$ , expressed in cells, and it has a standard deviation taken as a fraction of the whole dimension of the maplet's lateral side [60]. The correlation will provide the coordinates of a point of local maximum, which represents the measured displacement between the two images expressed in the frame of the maplet. This method can achieve sub-maplet-pixel accuracy by interpolating the local maximum with a polynomial of degree two, and the curvature of the paraboloid can be used to set a value for the uncertainty of the measurement.

This value, which is the measured position of the landmark, can be reprojected from the maplet frame to the pixels in the picture that was rectified (Figure 2.41), thus providing the new measurement for the landmark location on the image, corrected through maplet matching.

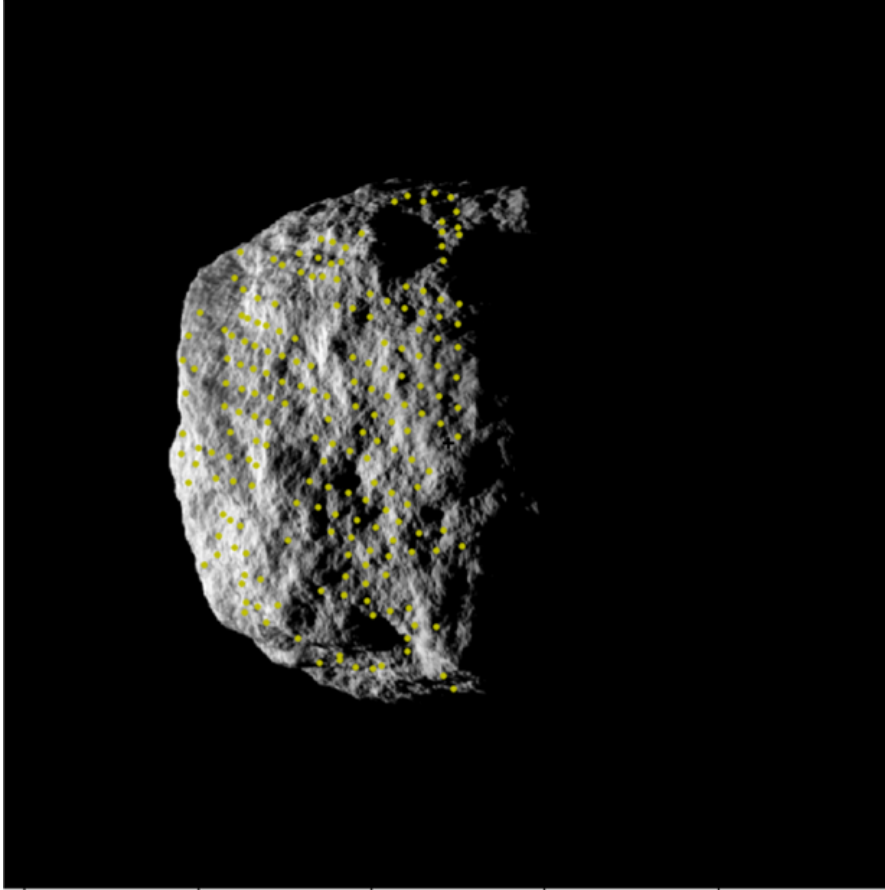


Figure 2.41: In yellow, all the landmark positions extracted from maplet matching, after being reprojected onto the original image.



# Chapter 3

## Results

The procedure described in chapter 2 allowed the creation of a database of simulated images captured at two hours step interval, properly filtered according to the visibility constraints on the landmarks. Then, for each landmark a sub selection of the best images led to the extraction of their corresponding maplets, creating a new maplet database.

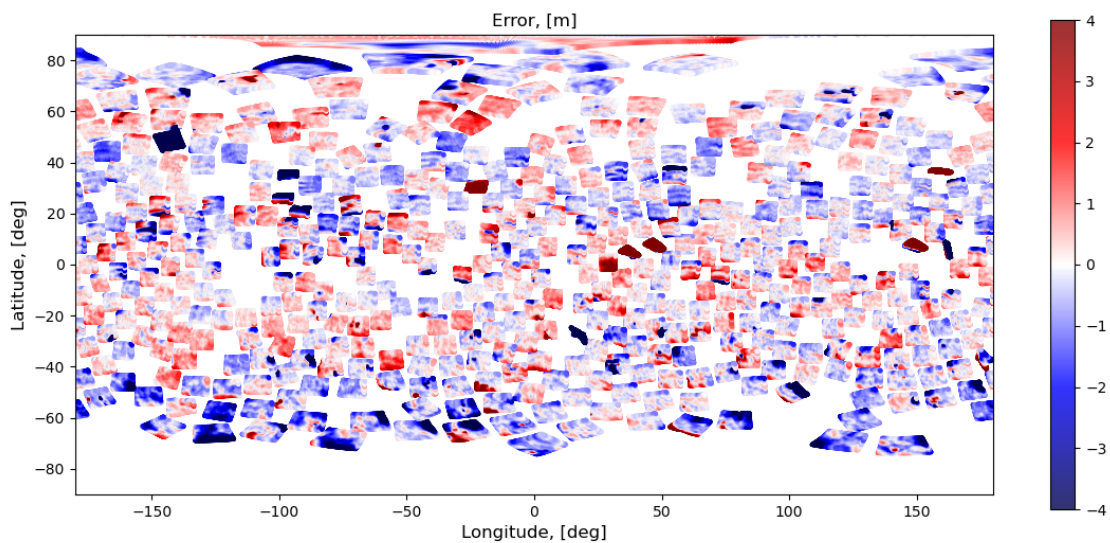


Figure 3.1: Difference between each maplet coordinate with respect to the original reference high resolution shape model, along the radial direction.

In Figure 3.1 it is possible to see the error of the created maplets' cell positions with respect to the ground truth, provided by the high resolution shape model used to generate the input images. It should be noted that no manual pre- or post-processing correction was applied on the inputs or outputs of the automatic routines used for the generation of the database. The initial distribution was comprising 560 landmarks equally spaced as per the Fibonacci method (like in Figure 2.6).

The missing maplets of Figure 3.1 are mostly located at low latitude values, where we

know that a limited number of images is available, and at other few positions around the asteroid's surface. In the latter case, even by changing the radial Z-coordinate described by the method of Figure 2.1, no convergence of the maplet creation method used to extract the geometry from the input images could be found. This may have different causes, such as an incorrect selection or a general lack of high quality images for that landmark in terms of illumination conditions.

In Figure 3.2 the error related to each created maplet is depicted, which is computed as RMS of the errors of all its cells (where the maplet lateral dimension is 40  $m$ , divided in  $99 \times 99$  cells).

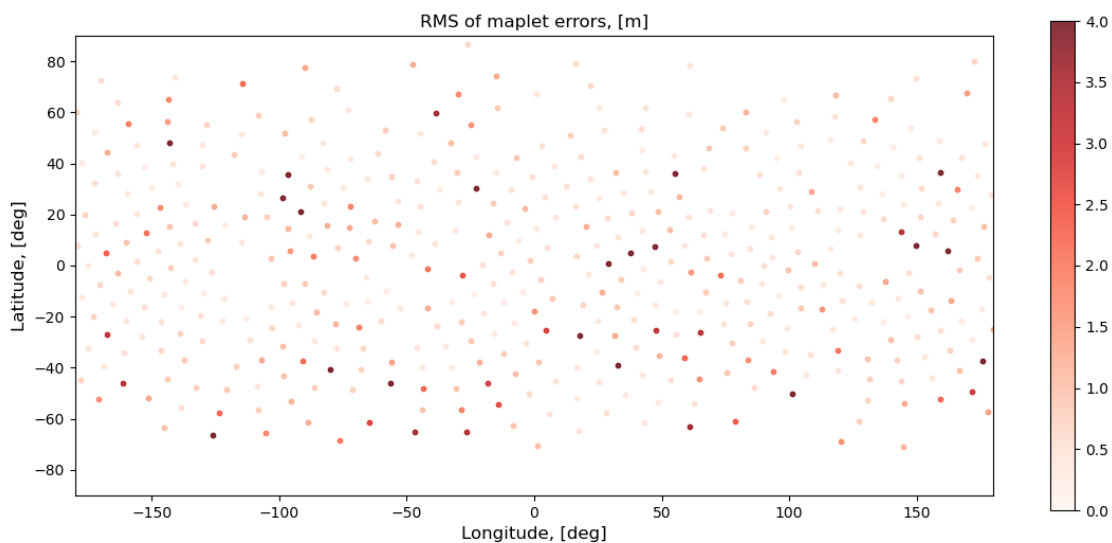


Figure 3.2: RMS of the maplet errors in the radial direction with respect to the original reference high resolution shape model.

Some of the maplets are characterized by large errors, and this is due to the convergence of the stereophotoclinometry method to a wrong geometry, thus providing false positives. However, since in the real scenario an *a priori* knowledge of the high resolution shape model is not available, the problematic maplets cannot be easily discerned. Therefore, we will remove the observables derived from maplets characterized by a wrong geometry by fine tuning some parameters involved in the optical observables extraction.

Given the maplet database, it was possible to reprocess all the images and extract the optical observables, expressed as sample and line coordinates in the pictures obtained through maplet matching. In this section, we will describe how certain parameters involved in the creation of the maplets have an influence in terms of quality of the output observables. The parameters that will be analyzed are related to:

- The maplet dimension, expressed in terms of length of its lateral side and considering a fixed number of maplet cells, so that the dimension univocally determines the

resolution of the maplet. In general, the lower the value, the higher the achieved accuracy.

- The minimum value of correlation of maplet matching, which tells how good the matching between the maplet, opportunely illuminated with a photometric model, is similar to the reprojected version of the corresponding region extracted from the image.
- The minimum value of occupation, which sets a limit to the amount of dark areas present in the rectified maplet, since it is possible to have false positives in case of high correlation but low number of non-black pixels.

The analysis will be performed in the order depicted above, considering the RMS of the residuals (between simulated observables and computed observables) as a high-level metric to assess the general quality of the simulated observables. At the first step, the values of correlation and occupation are set to almost non-constraining values, so that the most observables are retained. Then, after each step the best case is chosen, and a new test is performed, in order to empirically find the best compromise which provide a good output to be inserted in the estimation process.

### 3.1 Maplet dimension

In principle, the smaller the maplets, the better the accuracy in the matching of maplets with the images, due to the increased resolution provided by smaller maplet cell sizes. However, some other effects may play a role in the quality of the results.

Considering an extreme case in which the dimension is really low, if the resulting resolution of the maplet is too high, there may not be enough details in the target body to provide shadow information for the photoclinometry technique. On the other side, if the resolution is too low, the total accuracy that can be achieved with this method is left unexploited. Depending on the geometric conditions, for certain landmarks it may not be possible to have the desired resolution. In fact, to create a maplet of an arbitrary size, a collection of images should be available such that:

- The combination of distance from the landmark and focal length of the camera should provide the sensor a maplet with dimensions of constrained size, such that a single pixel is approximately as large as a maplet cell, with a tolerance of a factor of three.
- The illumination conditions are favorable, which means that the maplet is well-lit, the emission angle is not too high, and not too many shadows are present in the reprojected maplet image (i.e., a large enough occupation).

Therefore, these optimal conditions may not be available for all the landmarks and throughout the whole mission. Considering a setup where:

- There is a fixed set of pictures, spanning the whole Hera mission timeline at the binary system;
- All the parameters for the maplet creation are kept fixed, except for the desired maplet dimension;

the total number of maplets that are successfully created while varying the maplet dimension is shown in Figure 3.3.

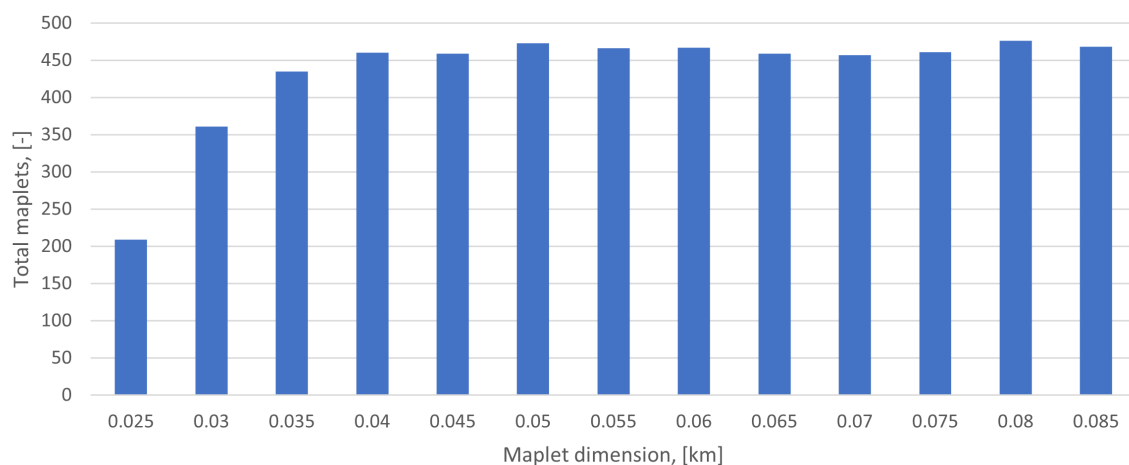


Figure 3.3: Maplets created with basic settings as a function of the maplet dimension.

In our case, we chose a total amount of 560 landmarks as a result of a Fibonacci lattice distribution, and they were in common to every analysis at each of the different maplet sizes. Not all the maplets of those landmarks reached convergence for the creation during the stereophotoclinometry technique, and this mainly depends on the availability of pictures with proper incident lighting conditions, emission, and phase angles.

Some parts of the asteroid may have regions fully in shadow for most of the pictures, or the landmarks are seen from high emission angles, so that their reprojection amplifies errors, introduces huge distortions, or exacerbates parallax effects. Even the method by which the candidate images are chosen affects the convergence of the maplet creation. In fact, a simple scoring for the pictures based on optimal geometric and illumination conditions may not fulfill the requirement of providing a selection with images that are lit differently among them. For example, in a test case with images taken at an acquisition rate up to one picture every five minutes, there were multiple images with very similar conditions characterized by high scores, so that the selection was providing images with high quality but lacking illumination diversity, leading to unsuccessful convergence in maplet creation.

Therefore, an additional constraint about the similarity of geometric and illumination conditions was added during the picture selection.

The other important parameter which affects the creation of the maplets is the distance, for which a filtering on the pictures is applied. This is most evident for the cases at smaller maplet dimensions, which are created in lower numbers. In fact, by looking at the distance of the spacecraft with respect to Didymos during the mission, the total amount of time spent at closer distances with respect to Didymos is much smaller: for comparison, the images available for the maplet size of 25  $m$  is approximately one-third of the images for the size of 40  $m$  (for precise numbers, see Appendix - Camera distances and maplet dimensions), thus not providing sufficient information for many landmarks.

The typical behavior of the residuals is depicted in Figure 3.4 (we consider the prefit version of the residuals, which is computed as a difference between the observable and the computed version from a model prior to any iterative correction of the estimation filter).

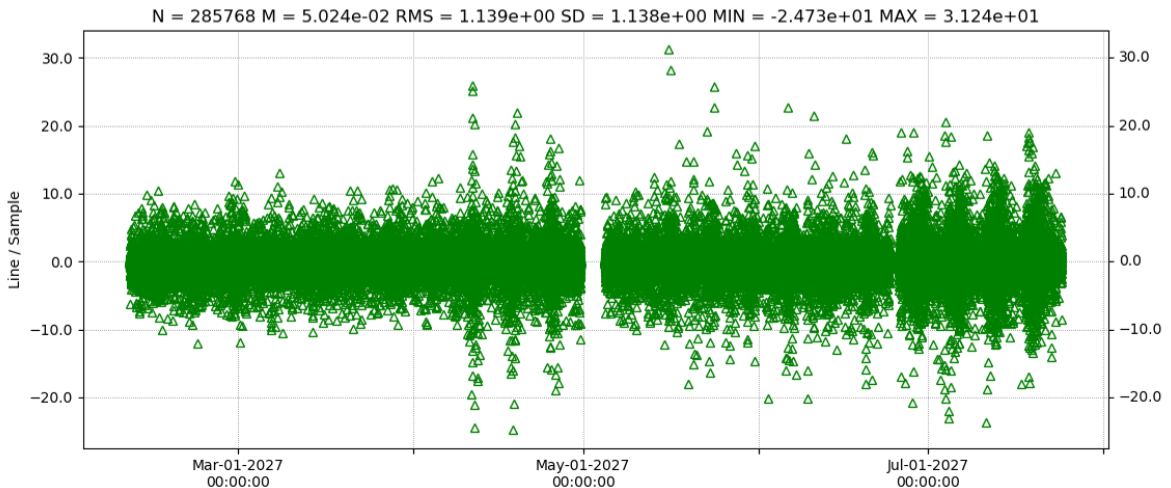


Figure 3.4: Prefit sample and line residuals, expressed in pixels, for 40  $m$  sized maplets, filtered for a minimum normalized correlation coefficient of 0.4 and minimum occupation of 0.3 during maplet matching.

The low value of normalized correlation used (in this case a relaxed version of 0.4) and occupation, while allowing a large number of observables to be kept, it cannot get rid of many observables which are worsening the distribution of the residuals.

If we consider an *a priori* fixed weight of 3 pixels for the sample and line observables, provided to each measurement without considering the information available as result of the maplet matching, it is possible to see also a general behaviour for the postfit residuals, computed after a single step of the iterations provided by the estimation filter. The result is depicted in Figure 3.5 and shows a trend similar to the prefit residuals.

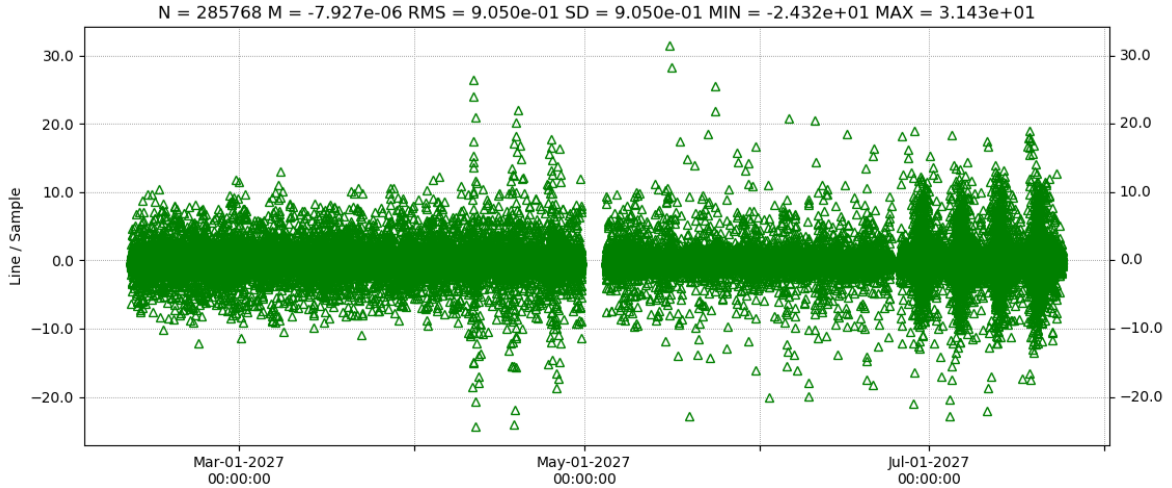


Figure 3.5: Postfit sample and line residuals, expressed in pixels, for 40  $m$  sized maplets, filtered for a minimum normalized correlation coefficient of 0.4 and minimum occupation of 0.3 during maplet matching.

As we can see, in both cases the RMS of the residuals is approximately one pixel, with a slight improvement thanks to the adaptation of the solve-for parameters applied by the filter in the postfit plot. There are some evident signatures, and they are correlated to the distance of the camera from Didymos: the considered maplet dimension of 40  $m$  provides better performance when the spacecraft is farther from the target landmarks, where the maplet cell side dimension is smaller than a pixel.

In general, the prefit and postfit residuals at different maplet sizes do not show any remarkable difference from the ones depicted in Figure 3.4 and Figure 3.5, except for their RMS, as it can be seen from their collection reported in Appendix - Residuals at different maplet dimensions. In Figure 3.6 we can see the RMS of the residuals in a summary of all the tested maplet size dimensions.

To a larger maplet dimension corresponds a larger value for the RMS of the residuals, which is mostly due to the lower resolution of the considered maplet. However, we can see that there is a value of minimum at around 40  $m$  of maplet side dimension. Therefore, this is the value that will be considered as a starting point for the next analysis based on the correlation value of the maplet matching.

It should be noted that, since the illumination and geometric conditions are kept the same for the whole dataset, the filtering performed is the same for all considered maplet dimensions of the test cases. Therefore, the difference between the multiple maplet sizes considered in this analysis is the result of the filtering based on the optimal distance only. By reversing the calculation, a maplet of 40  $m$  of maximum dimension per side is the result of pictures taken at an optimal distance of 4.33  $km$ , with minimum and maximum ranges of allowed values of [1.44  $km$ , 13  $km$ ] (see also Appendix - Camera distances and maplet dimensions).

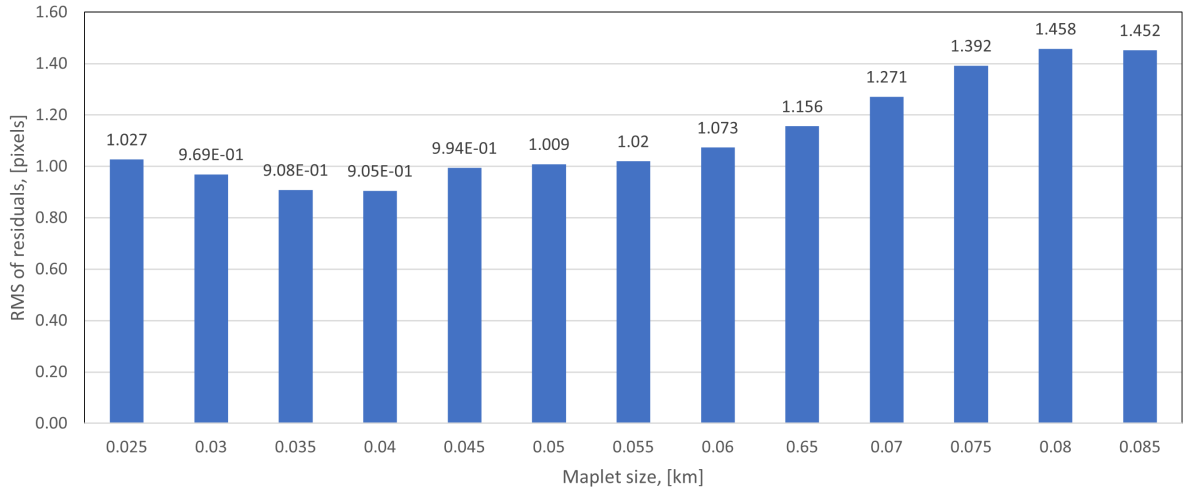


Figure 3.6: RMS of all the postfit residuals (as both sample and line) from the estimated solve-for parameters.

In Figure 3.7 the result of the selected pictures belonging to the chosen range of allowed distances is shown.

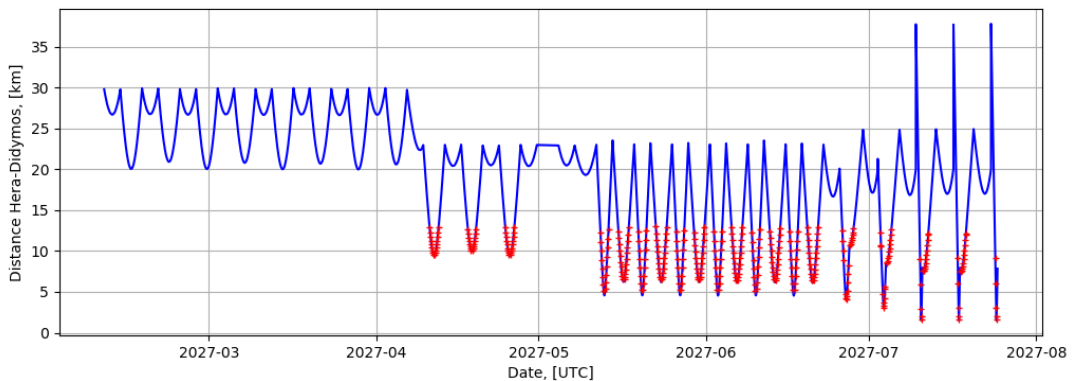


Figure 3.7: In red, the pictures (nominal setup with 2 h interval) at an optimal distance for the creation of maplets whose lateral size is 40 m.

At this preliminary step, this shows that the most useful pictures which lead to best outcomes in terms of residuals are the ones captured while Hera was closest to Didymos, thus leading to the creation of rather small maplets.

In this case, for maplet creation we are considering only a fraction of the whole dataset of pictures available, equal to 22% of the 1624 total images. However, it should be noted that the whole dataset of images is used when finally extracting the observables with maplet matching after maplet creation.

The effect of the filtering based on maplet dimension and distance on the total number of available pictures is shown in greater detail in Appendix - Camera distances and maplet

dimensions.

The results regarding the prefit and postfit residuals are summarized in the following tables, where the columns are defined as:

- N: the total number of sample and line observables. It should be divided by two to get the total number of observables as full pixel positions (since a pixel is formed by both sample and line) for each landmark.
- Mean: mean value of the residuals, in pixels.
- RMS: root mean square of the residuals, in pixels.
- SD: standard deviation of the residuals, in pixels.
- MIN, MAX: the minimum and maximum value of the residuals, in pixels. It provides rough information about the worst outliers.

The prefit data are summarized in Table 3.1.

Table 3.1: Prefit values based on maplet dimension. Common maplet matching minimum correlation allowed is 0.4.

Maplet size [ <i>km</i> ]	N [—]	Mean [ <i>pixels</i> ]	RMS [ <i>pixels</i> ]	SD [ <i>pixels</i> ]	MIN [ <i>pixels</i> ]	MAX [ <i>pixels</i> ]
0.025	110362	9.15E-02	1.136	1.132	-20.33	33.56
0.030	218516	9.19E-02	1.081	1.077	-32.31	25.42
0.035	264446	6.04E-02	1.052	1.051	-26.93	26.88
0.040	285768	5.02E-02	1.139	1.138	-24.73	31.24
0.045	290040	5.03E-02	1.145	1.144	-33.00	60.34
0.050	289580	5.04E-02	1.135	1.134	-34.76	37.84
0.055	279458	5.59E-02	1.128	1.127	-42.26	40.96
0.060	278626	4.95E-02	1.261	1.260	-44.40	42.75
0.065	267010	8.29E-02	1.316	1.314	-49.14	78.35
0.070	251940	8.86E-02	1.399	1.396	-40.42	53.26
0.075	243294	1.12E-01	1.520	1.516	-83.00	72.20
0.080	251220	1.20E-01	1.628	1.623	-50.84	53.92
0.085	246958	1.15E-01	1.651	1.647	-55.13	62.28

Whereas the postfit data are summarized in Table 3.2.

Table 3.2: Postfit values based on maplet dimension. Common maplet matching minimum correlation allowed is 0.4.

<b>Maplet size</b> [ <i>km</i> ]	<b>N</b> [ <i>-</i> ]	<b>Mean</b> [ <i>pixels</i> ]	<b>RMS</b> [ <i>pixels</i> ]	<b>SD</b> [ <i>pixels</i> ]	<b>MIN</b> [ <i>pixels</i> ]	<b>MAX</b> [ <i>pixels</i> ]
0.025	110362	1.15E-03	1.027	1.027	-20.44	29.47
0.030	218516	9.03E-04	0.969	0.969	-35.31	25.16
0.035	264446	-2.37E-04	0.908	0.908	-27.60	27.33
0.040	285768	-7.93E-06	0.905	0.905	-24.32	31.43
0.045	290040	-3.79E-04	0.994	0.994	-31.88	54.56
0.050	289580	3.60E-04	1.009	1.009	-32.86	37.61
0.055	279458	4.81E-05	1.020	1.020	-38.93	41.01
0.060	278626	-4.34E-04	1.073	1.073	-44.91	44.58
0.065	267010	2.85E-04	1.156	1.156	-46.69	74.87
0.070	251940	-7.29E-05	1.271	1.271	-39.92	53.5
0.075	243294	-1.19E-04	1.392	1.392	-75.88	64.79
0.080	251220	7.58E-04	1.458	1.458	-50.26	52.86
0.085	246958	5.05E-04	1.452	1.452	-51.39	57.52

In the next step, the best results of this analysis will be used as a starting point for the study of the effects of the correlation value on the output residuals.

## 3.2 Maplet matching minimum correlation

An important parameter regarding the extraction of optical observables is the value of normalized correlation which is found during the maplet matching technique. In this case, the correlation is performed between two pictures, such as one is rectified version of a picture of the asteroid and the other is a simulated top view of a maplet. The latter is obtained considering the corresponding photometric parameters and the computed photometric angles required to properly illuminate it in the attempt of matching the conditions of the corresponding rectified picture.

Depending on the minimum threshold value of correlation for which an observable can be extracted, we may have false positives or missed correlations. While a missed correlation translates simply into a missing observable for the final estimation procedure, a false positive will instead affect more seriously the results, since we are introducing to the OD setup a measurement with an incorrect uncertainty. In fact, if the maximum correlation value is too small, it is probable that the measurement is a false positive. However, that value becomes an observable nonetheless: in that case, it will be associated with

an uncertainty value which is far too optimistic, since it is computed on the basis of the spread of the correlation function around its maximum value. Therefore, for the purpose of estimation of the landmark positions, it is better to keep only the data which are not deceiving the algorithm with their unrealistic associated uncertainties, and that means to use only observables with a high correlation index.

While keeping all the other parameters constant, such as the maplet dimension (chosen to be 40  $m$ , from the preliminary results seen before) and minimum occupation factor (0.3), the behavior of the RMS of the residuals as a function of the normalized correlation coefficient is shown in Figure 3.8.

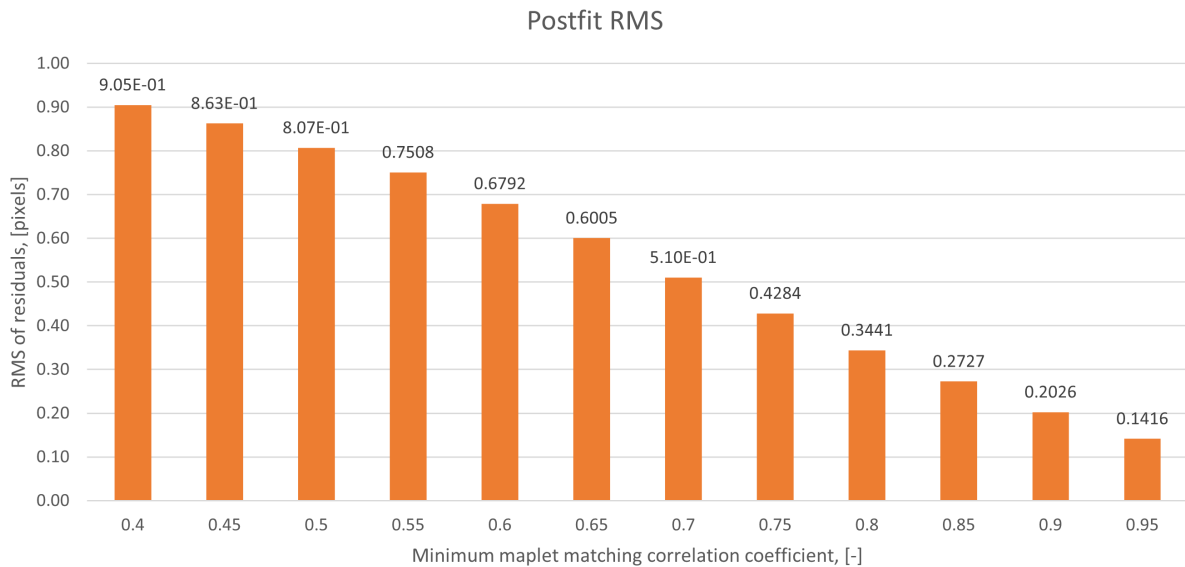


Figure 3.8: RMS of the postfit residuals as a function of the minimum maplet matching correlation value allowed.

In the plot there is an evident decreasing trend, where the RMS of the residuals improves, as the minimum correlation allowed to create an observable increases.

However, depending on the correlation chosen, there is also a different number of observables that are kept after filtering, and this is shown in Figure 3.9. Since the number of total observables is rapidly decreasing with the correlation coefficient, it is worth considering a new metric, which is the ratio of postfit residual's RMS and total number of observables, as depicted in Figure 3.10, in order to keep a larger number of observables for the next steps, while preserving a good performance provided by a sufficiently large correlation.

The gain in RMS associated with large values of minimum correlation (namely greater than 0.9) is associated with a much higher loss of total observables available. Since for the analysis we want to keep a number of observables larger than the values filtered with best minimum correlation, we will consider the point of minimum of the ratio (at 0.85

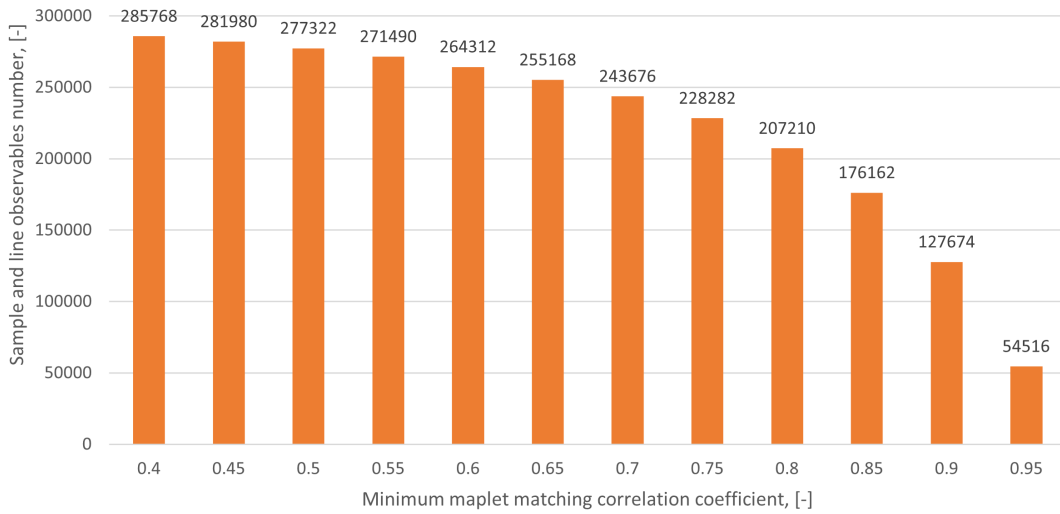


Figure 3.9: Total number of sample and lines observables as a function of the minimum maplet correlation allowed.

minimum correlation) as a starting point for the next analysis. At this point, we have the best compromise between total number of observables and output residuals quality, with a decrease of approximately 70% in terms of RMS of the residuals with respect to the starting value.

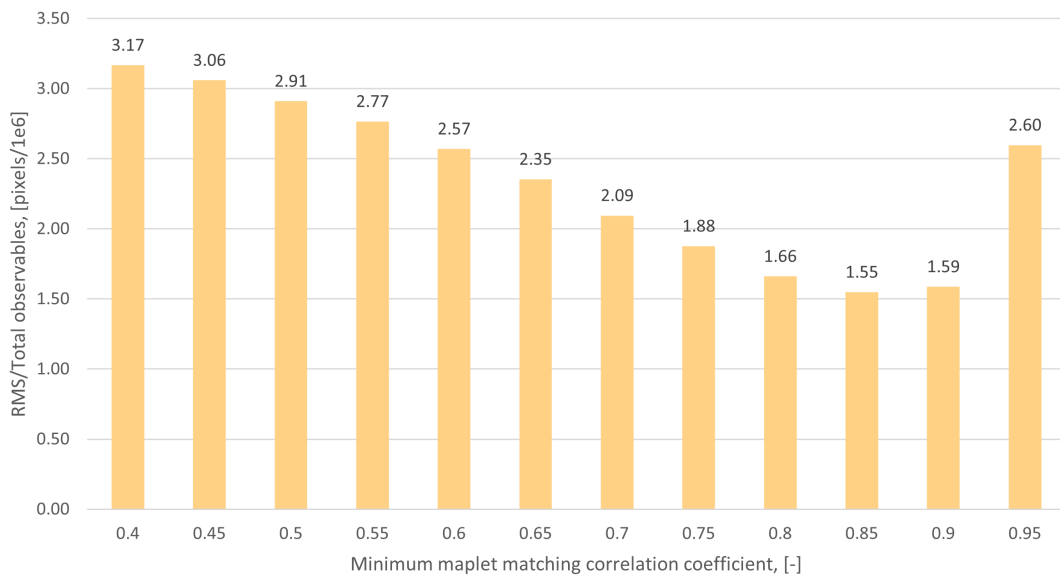


Figure 3.10: Ratio RMS and number of observables.

The profit (Figure 3.11) and postfit residuals (Figure 3.12), which are the outcome of the minimum normalized correlation value of 0.85, provide better statistical properties with respect to the starting point depicted in Figure 3.4 and Figure 3.5, which were characterized by a value of minimum correlation of only 0.4.

The prefit residuals are shown in Figure 3.11, and they are related to all the observables that could be extracted from all the images of the mission.

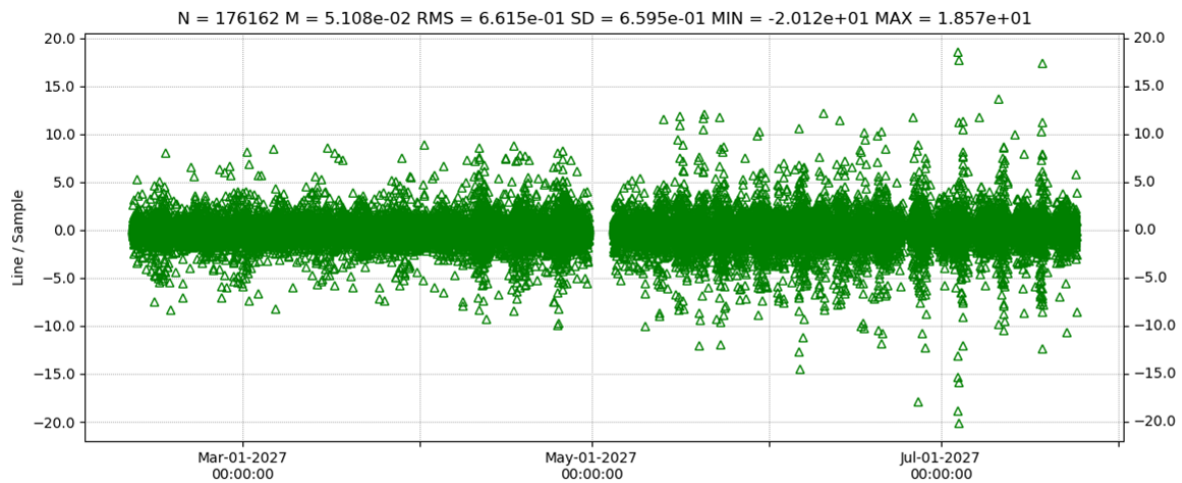


Figure 3.11: Prefit sample and line residuals, expressed in pixels, considering a maplet size of 40  $m$ , minimum maplet matching correlation allowed of 0.85, and minimum occupation of 0.3.

And the postfit residuals are shown in Figure 3.12.

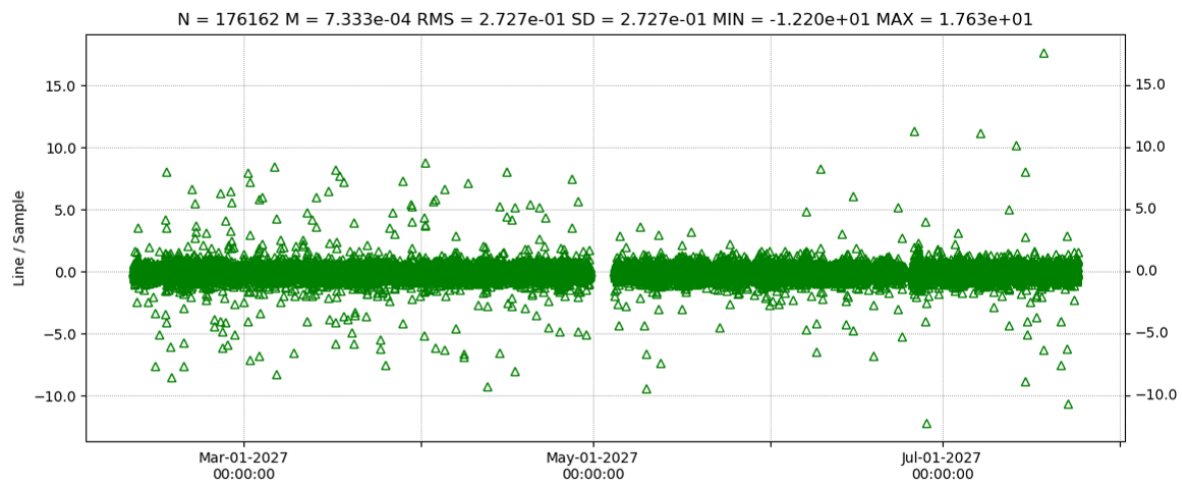


Figure 3.12: Postfit sample and line residuals, expressed in pixels, considering a maplet size of 40  $m$ , minimum maplet matching correlation allowed of 0.85, and minimum occupation of 0.3.

The residuals for the whole dataset of different minimum correlation values are reported in Appendix - Residuals at different minimum correlation for maplet matching.

In Table 3.3 the results for the prefit case are summarized.

Table 3.3: Prefit values based on maplet matching minimum correlation. Maplet size of 40  $m$ .

<b>min(Correlation)</b> [-]	<b>N</b> [-]	<b>Mean</b> [ <i>pixels</i> ]	<b>RMS</b> [ <i>pixels</i> ]	<b>SD</b> [ <i>pixels</i> ]	<b>MIN</b> [ <i>pixels</i> ]	<b>MAX</b> [ <i>pixels</i> ]
0.40	285768	5.02E-02	1.1390	1.1380	-24.73	31.24
0.45	281980	4.97E-02	1.1030	1.1020	-24.73	31.24
0.50	277322	4.84E-02	1.0570	1.0550	-24.73	31.24
0.55	271490	4.77E-02	1.0110	1.0090	-24.73	31.24
0.60	264312	4.80E-02	0.9521	0.9508	-23.04	31.24
0.65	255168	4.77E-02	0.8913	0.8901	-23.04	31.24
0.70	243676	4.75E-02	0.8238	0.8224	-20.83	20.63
0.75	228282	4.69E-02	0.7639	0.7625	-20.83	20.63
0.80	207210	4.97E-02	0.7030	0.7013	-20.12	19.23
0.85	176162	5.11E-02	0.6615	0.6590	-20.12	18.57
0.90	127674	6.04E-02	0.6429	0.6401	-18.85	18.57
0.95	54516	9.07E-02	0.6733	0.6672	-17.85	17.70

And in Table 3.4 the results related to the postfit.

Table 3.4: Postfit values based on maplet matching minimum correlation. Maplet size of 40  $m$ .

<b>min(Correlation)</b> [-]	<b>N</b> [-]	<b>Mean</b> [ <i>pixels</i> ]	<b>RMS</b> [ <i>pixels</i> ]	<b>SD</b> [ <i>pixels</i> ]	<b>MIN</b> [ <i>pixels</i> ]	<b>MAX</b> [ <i>pixels</i> ]
0.40	285768	-7.93E-06	0.9050	0.9050	-24.32	31.43
0.45	281980	6.55E-04	0.8626	0.8626	-24.35	31.44
0.50	277322	4.06E-04	0.8070	0.8070	-24.35	31.44
0.55	271490	5.68E-04	0.7508	0.7508	-24.36	31.45
0.60	264312	4.83E-04	0.6792	0.6792	-22.52	31.47
0.65	255168	5.00E-04	0.6005	0.6005	-22.48	31.47
0.70	243676	5.23E-04	0.5104	0.5104	-20.93	18.97
0.75	228282	4.10E-04	0.4284	0.4284	-20.90	18.78
0.80	207210	5.57E-04	0.3441	0.3441	-17.27	18.81
0.85	176162	7.33E-04	0.2727	0.2727	-12.20	17.63
0.90	127674	7.60E-04	0.2026	0.2026	-10.60	8.15
0.95	54516	1.58E-03	0.1416	0.1416	-16.53	14.90

### 3.3 Maplet matching minimum occupation

Once a simulated picture containing a maplet is reprojected to get the top view used for maplet matching, it is possible to have parts of the rectified maplet in shade, and it depends on the illumination conditions and local geometry. Therefore, it is important to have a minimum value of the maplet correctly lit, so that it becomes less probable that a correlation found is a false positive. In particular, this value is described by an occupation factor.

The occupation is defined as the ratio between the total number of lit cells and total considered cells during the correlation for maplet matching, which depends on the gaussian distribution introduced in the correlation function (the area of validity is a 3-sigma region based on the pixel uncertainty).

In the previous step regarding the analysis about the minimum correlation allowed, the fixed value of occupation used was 0.3 (corresponding to the 30% of the total considered surface). This will be the lowest value considered in this analysis, where we fixed the dimension of the maplet to 40  $m$  and the minimum correlation factor to 0.85. It should be noted that we can expect other improvements in terms of residuals by increasing the correlation factor. However, this gain is counterbalanced by the loss of many potentially good observables.

If we test all the higher values of occupation up to the maximum allowed, at 100% of occupation no observables are left, which means that at least some dark pixels (with no shading information) are always present in every landmark observation. This naturally derives from the raytracing model used for the image simulation, which does not provide multipath scattering and no pixels are partially lit when in full shade, giving the typical moon-surface-like look in which the shadows are pure black.

The results on the RMS of the postfit residuals as a function of the occupation ratio are depicted in Figure 3.13.

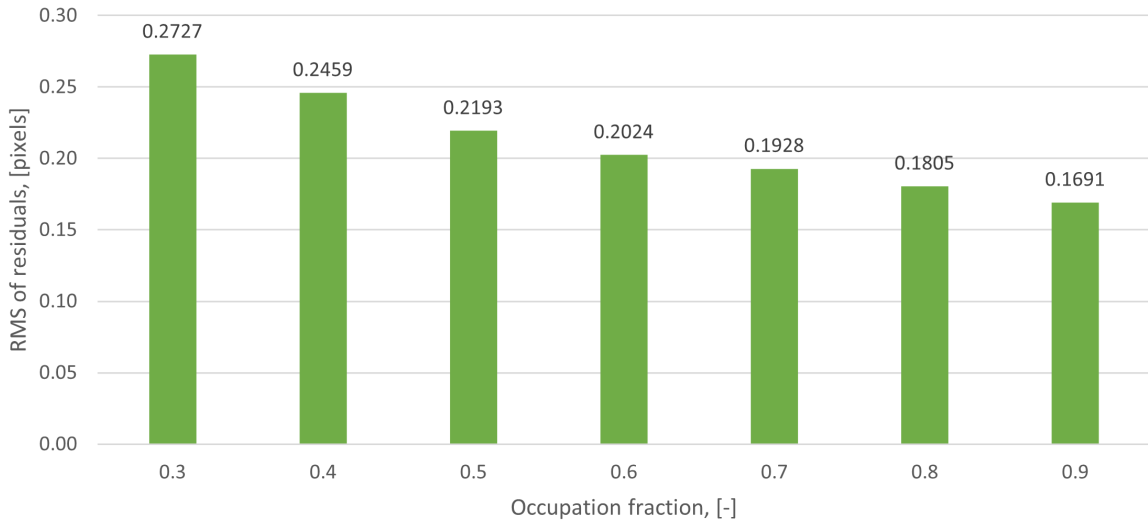


Figure 3.13: Postfit residuals as a function of the occupation factor. Maplet of 40  $m$  with 0.85 minimum maplet matching correlation is considered.

The prefit residuals are described in Table 3.5, and in Table 3.6 we can find the postfit.

Table 3.5: Prefit residuals varying the occupation factor.

<b>min(Occupation)</b> [-]	<b>N</b> [-]	<b>Mean</b> [pixels]	<b>RMS</b> [pixels]	<b>SD</b> [pixels]	<b>MIN</b> [pixels]	<b>MAX</b> [pixels]
0.3	176162	5.11E-02	0.661	0.659	-20.12	18.57
0.4	174116	5.29E-02	0.647	0.645	-20.12	18.57
0.5	171728	5.46E-02	0.633	0.631	-20.12	18.57
0.6	168606	5.74E-02	0.625	0.622	-20.12	18.57
0.7	164514	6.07E-02	0.612	0.609	-18.85	18.57
0.8	158388	6.52E-02	0.606	0.602	-18.85	18.57
0.9	147758	7.29E-02	0.590	0.586	-17.85	17.70

Table 3.6: Postfit residuals varying the occupation factor.

<b>min(Occupation)</b> [-]	<b>N</b> [-]	<b>Mean</b> [pixels]	<b>RMS</b> [pixels]	<b>SD</b> [pixels]	<b>MIN</b> [pixels]	<b>MAX</b> [pixels]
0.3	176162	7.33E-04	0.273	0.273	-12.20	17.63
0.4	174116	8.54E-04	0.246	0.246	-12.18	17.65
0.5	171728	8.46E-04	0.219	0.219	12.02	10.19

continued on next page

continued from previous page

0.6	168606	9.51E-04	0.202	0.202	-12.09	7.03
0.7	164514	1.05E-03	0.193	0.193	-12.09	4.96
0.8	158388	1.16E-03	0.180	0.180	-4.78	4.96
0.9	147758	1.25E-03	0.169	0.169	-4.77	3.27

As a difference with respect to the minimum correlation case, the total loss of observables is quite limited (with 0.9 of occupation ratio, we lose 16% of sample and line observables with respect to the reference case with 0.3 of occupation ratio). The improvement achievable by this filtering is shown in detail in Appendix - Residuals at different minimum occupation for maplet matching. Here we present the best case, which is related to the occupation ratio of 0.9, where the prefit residuals are depicted in Figure 3.14 and the postfit in Figure 3.15.

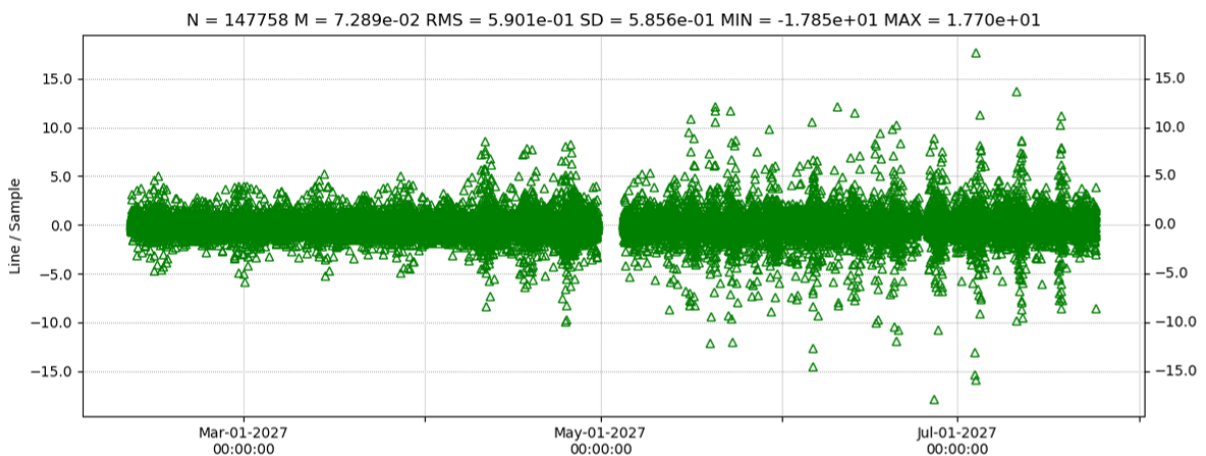


Figure 3.14: Prefit sample and line residuals, expressed in pixels, considering maplets of 40  $m$ , a minimum correlation of 0.85 and a minimum occupation of 0.9.

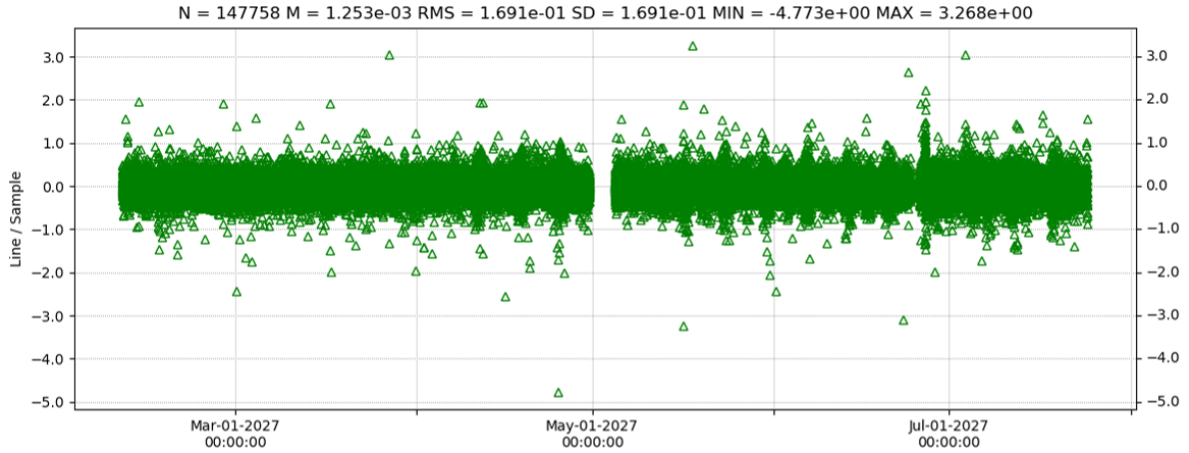


Figure 3.15: Postfit sample and line residuals, expressed in pixels, considering maplets of 40 m, a minimum correlation of 0.85 and a minimum occupation of 0.9.

This particular minimum value of occupation selected, equal to 0.9, provides an improvement to the RMS of the residuals of approximately 38% with respect to the standard case considered after the correlation analysis, with 0.3 of minimum occupation value. Therefore, by increasing the value of this filtering we are obtaining in general better performances.

To summarize, starting from an initial case with maplets of 40 m characterized by 285768 sample and line observables available, at the end of this filtering the total number dropped to 147758, which is 51% of the total amount available for that dimension of maplets.



# Chapter 4

## Conclusions

For deep-space missions towards small bodies, estimating the spacecraft trajectory relative to the target body is of primary importance. The orbit determination (OD) is usually performed through a combination of radiometric tracking, which provides very accurate measurement of the inertial spacecraft state with respect to the Earth, and optical observables that are extracted from the images captured by the onboard navigation cameras.

For OD simulations and covariance analysis, the optical observables, which are represented by the sample and line pixel coordinates of a target feature (e.g. the centroid of a body or its surface landmarks) are typically computed with simplified and often unrealistic assumptions, such that the measurements are affected by zero-mean gaussian white noise. Therefore, the purpose of this work is to improve the fidelity of the OD simulations by introducing more realistic optical observables.

To this extent, a pipeline for the extraction of optical observables, which was prepared by ESA Flight Dynamics team for the Rosetta mission, has been readapted for the Hera mission to the Didymos system. The modification of the ESA pipeline led to the creation of the proper optical observable inputs as if they were collected by the Hera Asteroid Framing Camera (AFC) while orbiting around the Didymos asteroid. Then, these optical observables are fed into an OD filter which is based on the MONTE software.

In more detail, the readapted ESA code is capable of closely mimicking how the optical observables are generated during the real mission. At first, we create a series of simulated pictures, starting with the same initial conditions used in the dynamical model, expressed in terms of positions and attitudes for all the involved bodies (the Hera camera, Didymos, and the Sun). Once all these pictures are created, they are processed to create a database of height maps, the maplets, in which the reconstructed geometry around a landmark is obtained. After proper image reprojection, these maplets are matched with the reprojected version of the simulated pictures, thus leading to the creation of optical observables, whose quality is dependent on different parameters involved in the process of maplet creation and maplet matching.

In our analysis, we show that the success of the stereophotoclinometry method in providing good quality optical observables depends on a proper choice of optimal parameters, expressed in terms of maplet dimension and parameters of the maplet matching, such as the correlation value and the occupation factor that each maplet has with respect to the reprojected image.

A sensitivity analysis has then been carried out by varying the list of considered parameters within the significative ranges of values for the Hera setup. The purpose of this preliminary analysis is to highlight the performance of the OD solution based on the quality of the residuals provided by the stereophotoclinometry method and also based on the reliability of the estimated parameters of the dynamical model and their associated covariances.

The results of this analysis indicate that the best performances can be obtained by considering maplets of small dimensions, which in the case of the Hera mission can be created only in the phases where Hera is sufficiently close to Didymos. This is due to the improved resolution that can be achieved with smaller maplets, since the total number of maplet cells is kept constant.

Another contributing factor is represented by the image correlation value, which represents the similarity of the image acquired by the camera with respect to an artificial one obtained starting from the maplet. By tuning this parameter, it is possible to further improve the quality of the observables (expressed in terms of RMS of the residuals) by about 70%, with respect to a case using a low value of minimum correlation allowed in the optical observable extraction. Furthermore, another 38% improvement to the RMS of the residuals (obtained from the optimal value of correlation found) can be achieved by constraining the values of the occupation parameter, which represents the fraction of pixels whose intensity level is above a certain threshold, thus excluding the pixels which are too dark to carry information about the slope content of the imaged region.

This preliminary study can be further improved with future works. The analysis of the effects provided by the creation of maplets with different subsets of images may be analyzed, for example by considering the pictures collected only during arbitrary phases of the mission, leading to a scenario that will mimic the ongoing results before the whole image dataset is available. The total number of collected images, the different pointing schemes, and the different timing distributions for capturing the pictures may also be addressed, in order to better understand how these values affect the final quality of the estimated dynamical parameters. Additionally, a study related to the input shape and albedo models may be addressed, considering how different terrain features and relative frequency distribution of craters, boulders, or smooth surfaces affect the process. In this way, the landmark distribution can be automatically selected with different methodologies with respect to the proposed one, taking into account the characteristics of the body surface. Other possible paths that can be taken are concerning the introduction of distortion

models for the camera, additional noise sources, or errors in the positions and attitudes of the involved bodies. An approach in the direction of artificial intelligence-assisted feature detection by means of convolutional neural networks may also be addressed, thus making the automatic selection of the initial guess values for the landmark positions more reliable. To conclude, the stereophotoclinometry is a useful technique that is capable of generating high-quality optical observables, thus providing to the OD an improvement of the reliability of the results. Depending on the mission case, in order to exploit the best capabilities of the method, a fine tuning of its parameters is required. In fact, this tuning will allow to find a sweet spot for which most false positives are avoided and such that the residuals have reduced RMS.



# Appendix

## Residuals at different maplet dimensions

If we consider maplets of different sizes, and all the other parameters fixed, which leads to a database of images common to all the cases depicted below, we have the following behavior in terms of profit residuals.

The other fixed parameters considered are:

- $\min(\textit{Correlation}) = 0.4$ .
- $\min(\textit{Occupation}) = 0.3$ .

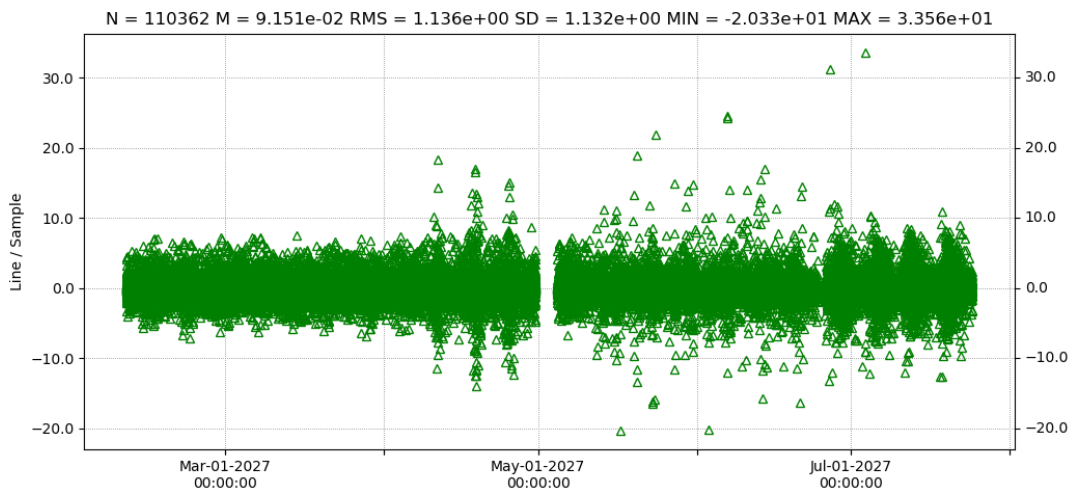
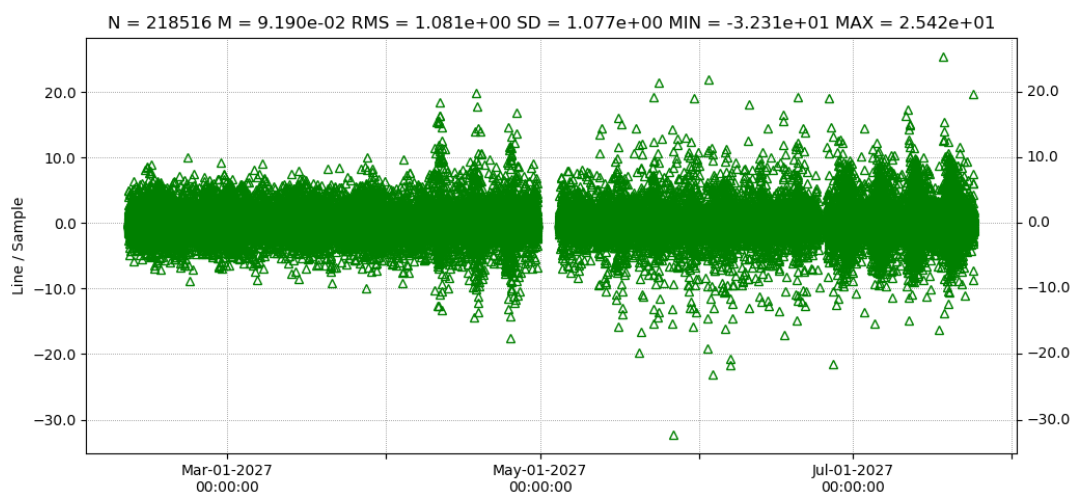
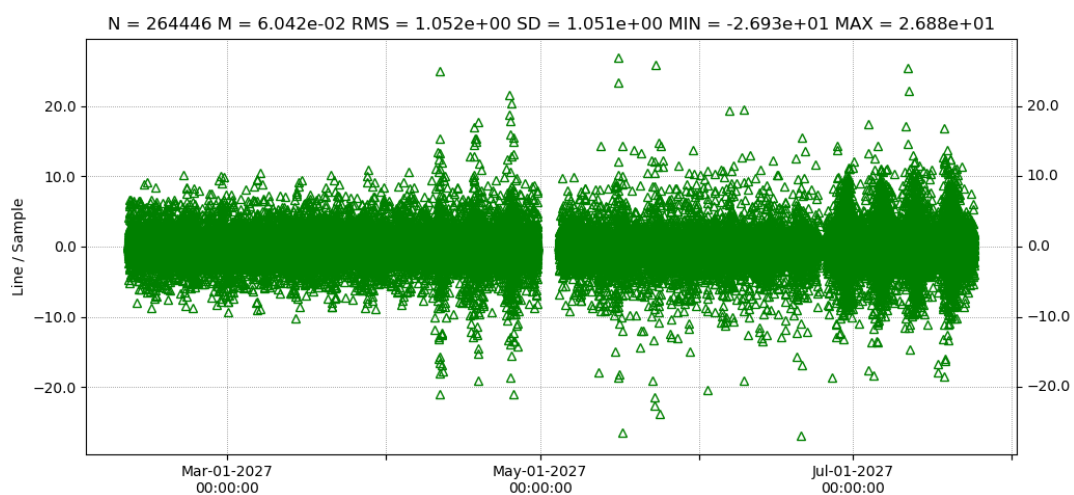
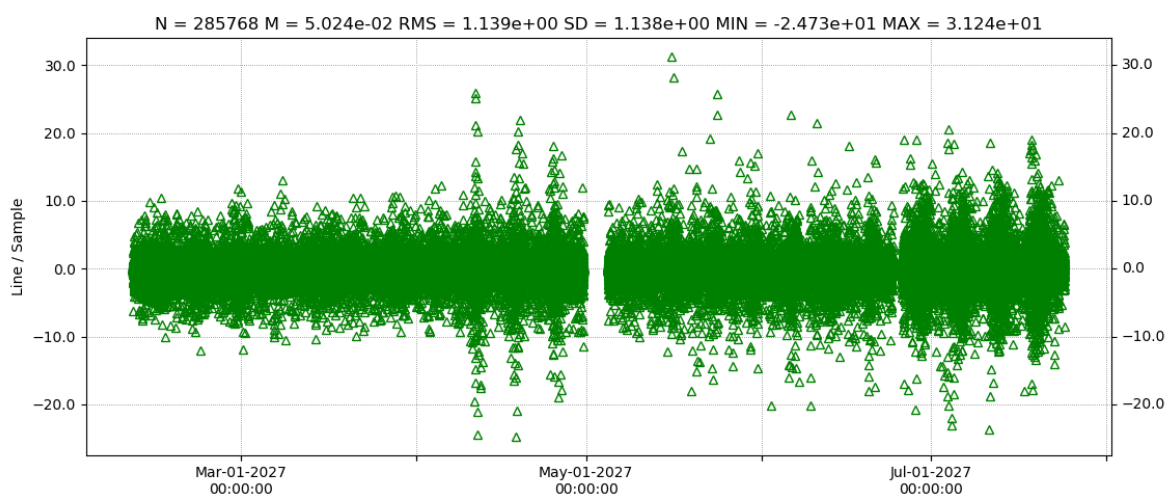


Figure 4.1: 25 m Maplet lateral side, profit.

Figure 4.2: 30 *m* Maplet lateral side, prefit.Figure 4.3: 35 *m* Maplet lateral side, prefit.Figure 4.4: 40 *m* Maplet lateral side, prefit.

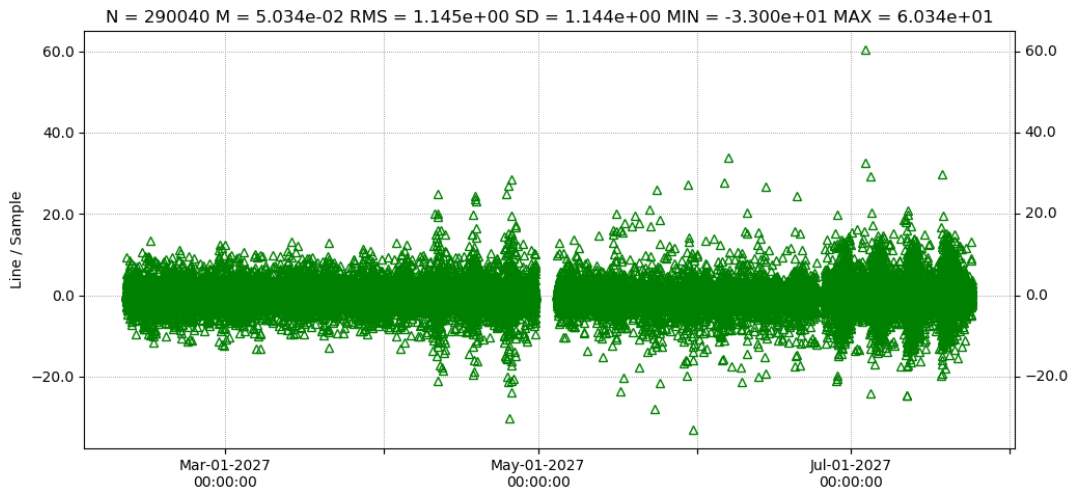


Figure 4.5: 45 *m* Maplet lateral side, prefit.

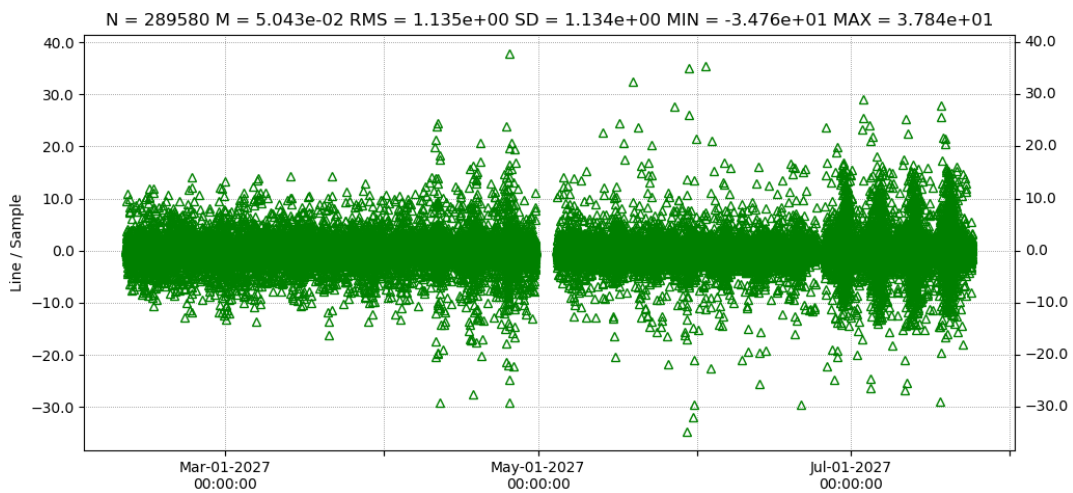


Figure 4.6: 50 *m* Maplet lateral side, prefit.

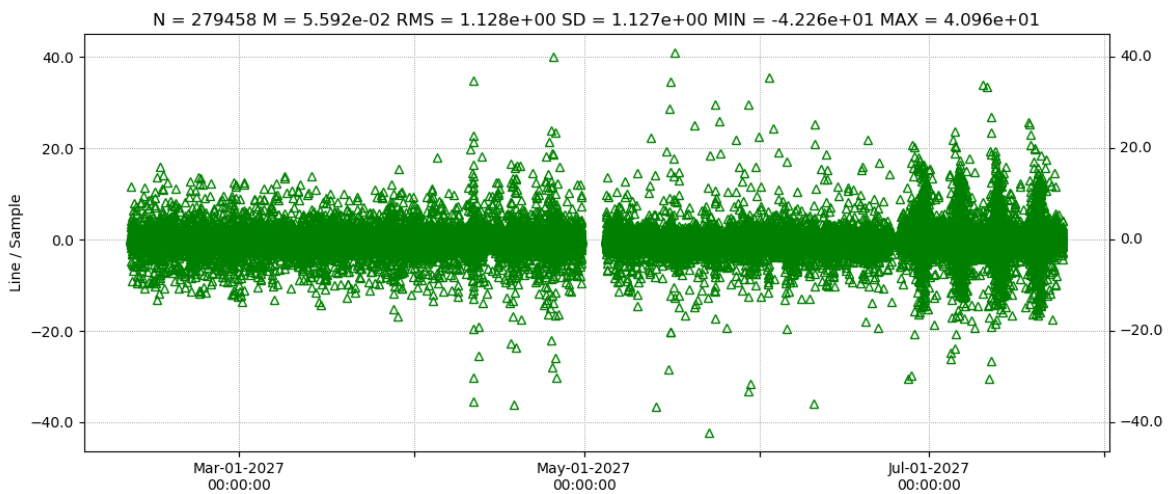
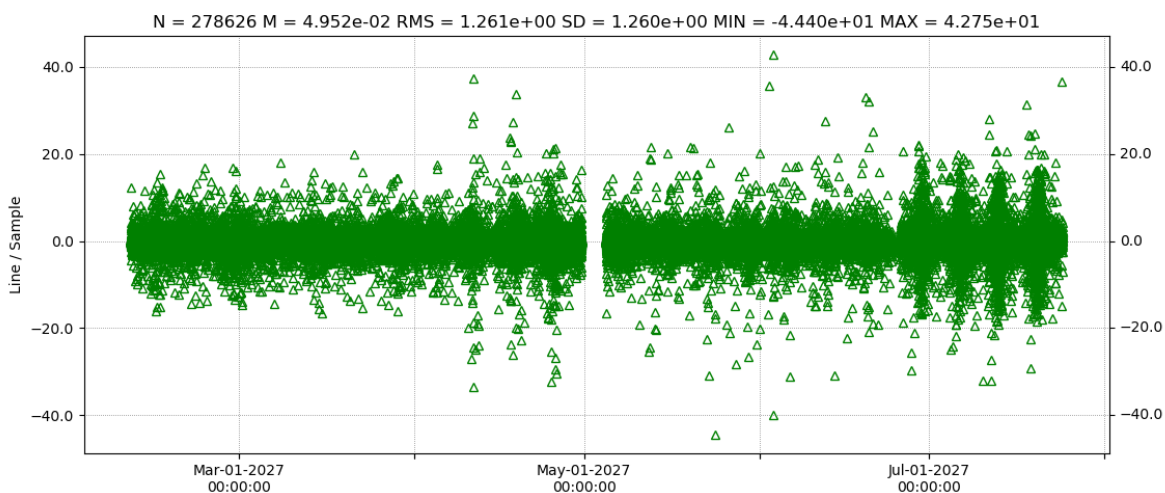
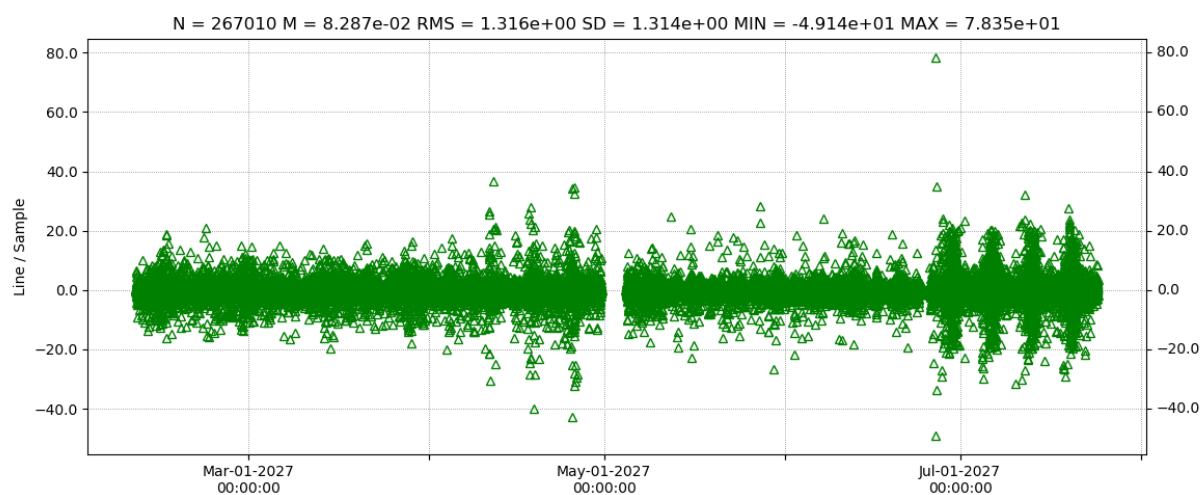
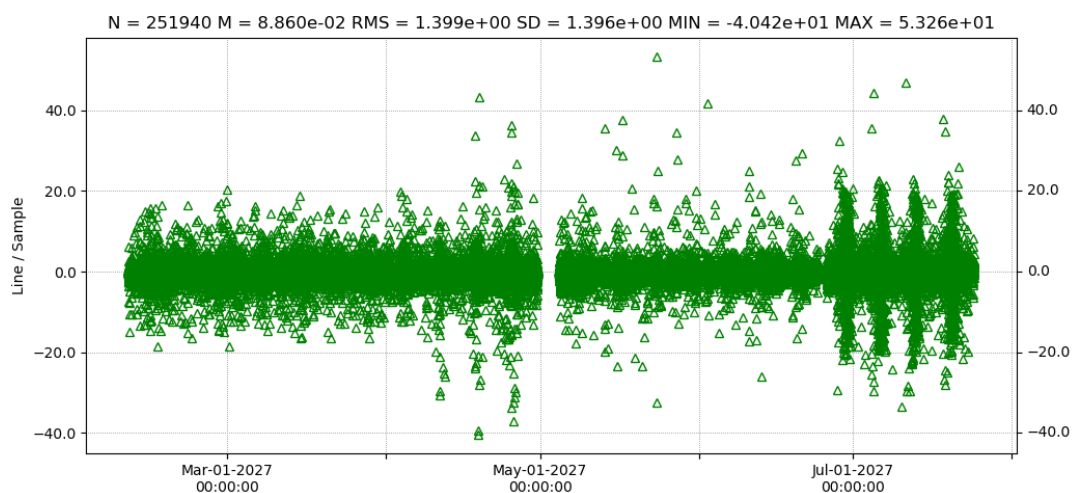


Figure 4.7: 55 *m* Maplet lateral side, prefit.

Figure 4.8: 60 *m* Maplet lateral side, prefit.Figure 4.9: 65 *m* Maplet lateral side, prefit.Figure 4.10: 70 *m* Maplet lateral side, prefit.

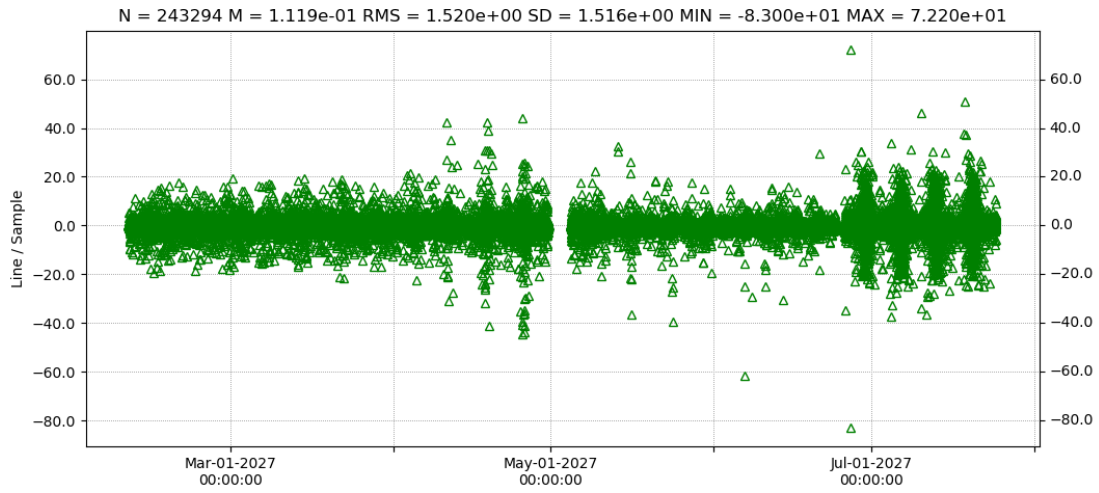


Figure 4.11: 75 *m* Maplet lateral side, prefit.

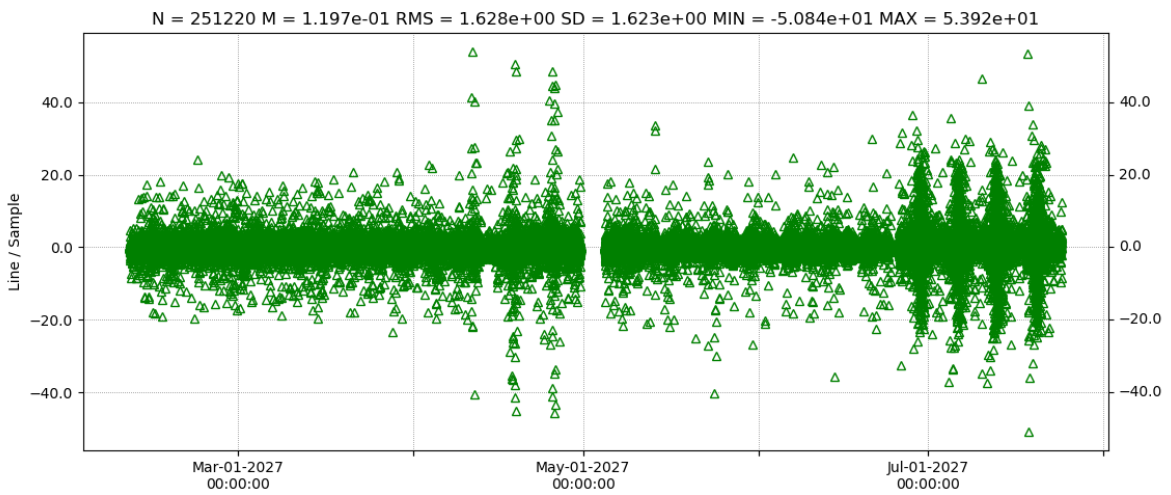


Figure 4.12: 80 *m* Maplet lateral side, prefit.

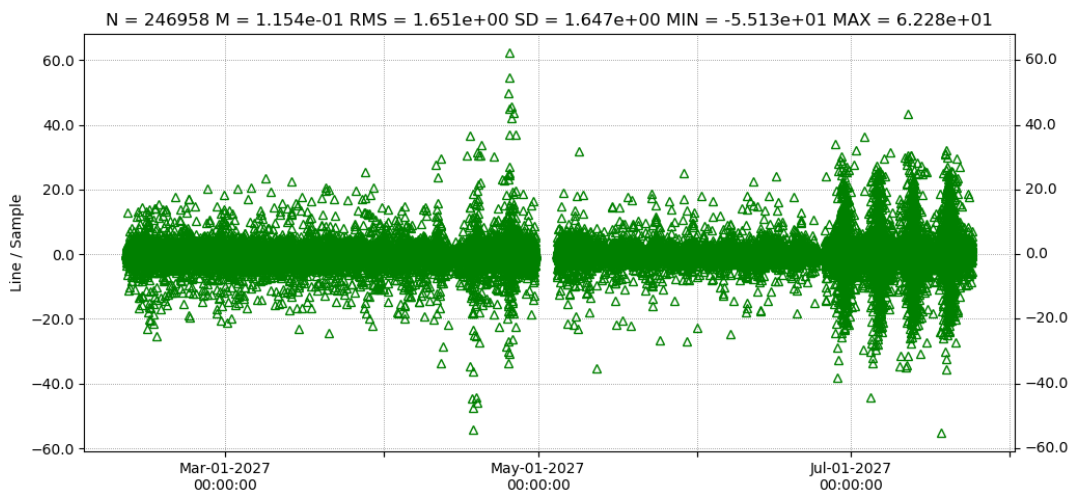


Figure 4.13: 85 *m* Maplet lateral side, prefit.

## Camera distances and maplet dimensions

Considering maplets of different sizes, for their creation it exists an optimal range of distances  $d$  which is (see Equation 2.17):

$$d = k \cdot \text{pixelMaplet} \cdot \frac{f}{\text{pixelCCD}}, \quad k \in \left[ \frac{1}{3}, 3 \right]$$

Where  $f$  is the focal length of the camera,  $\text{pixelMaplet}$  and  $\text{pixelCCD}$  are the physical dimensions of a maplet cell and the size of a pixel of the camera sensor, respectively. Here we collect, for convenience, the distances relative to each maplet dimension, considering the parameters of the AFC and maplets whose sizes are in the range from 25  $m$  to 85  $m$  with a step of 5  $m$ :

Table 4.1: AFC distances allowed for each maplet dimension.

Maplet size [ $m$ ]	Nominal distance [ $km$ ]	Minimum [ $km$ ]	Maximum [ $km$ ]
25	2.71	0.90	8.12
30	3.25	1.08	9.74
35	3.79	1.26	11.37
40	4.33	1.44	12.99
45	4.87	1.62	14.61
50	5.41	1.80	16.24
55	5.95	1.98	17.86
60	6.49	2.16	19.48
65	7.04	2.35	21.11
70	7.58	2.53	22.73
75	8.12	2.71	24.36
80	8.66	2.89	25.98
85	9.20	3.07	27.60

In the plots below we show how the pictures are distributed and filtered throughout the whole mission, based on the camera distance from the landmarks, here simplified as the distance from Didymos. The acquisition rate is set as per the nominal setup, with pictures taken every 2 hours, avoiding the beginning, end, and closest approach for each arc, when only radiometric observables are collected.

It should be noted that the considered nominal acquisition rate without any filtering based on distance would provide a total amount of 1624 pictures. No other filtering conditions (visibility, illumination, etc.) are considered.

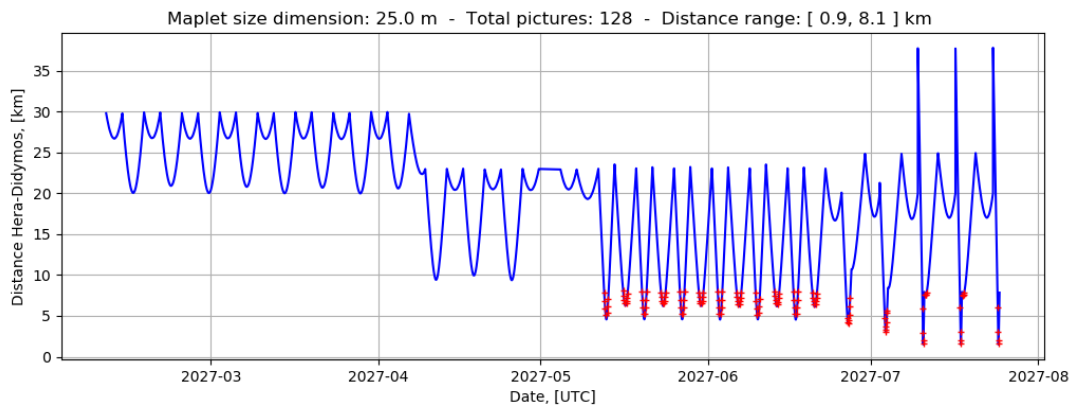


Figure 4.14: 25 m Maplet lateral side, 128 selected pictures.

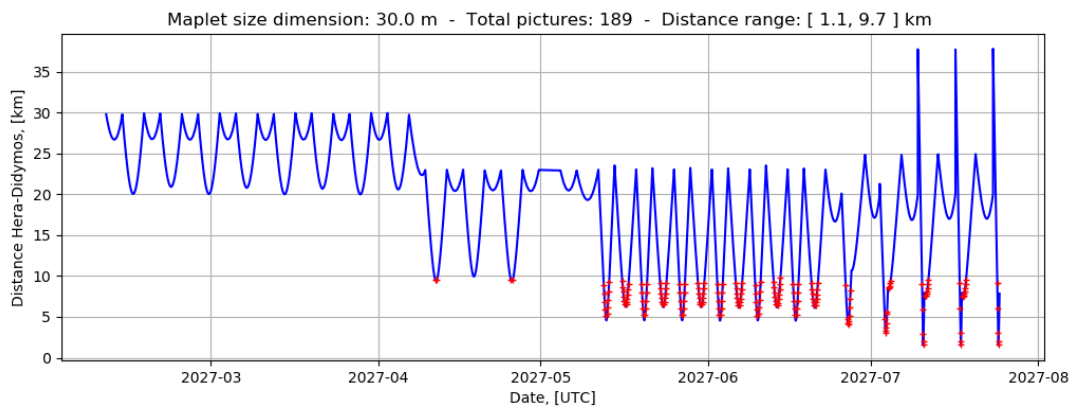


Figure 4.15: 30 m Maplet lateral side, 189 selected pictures.

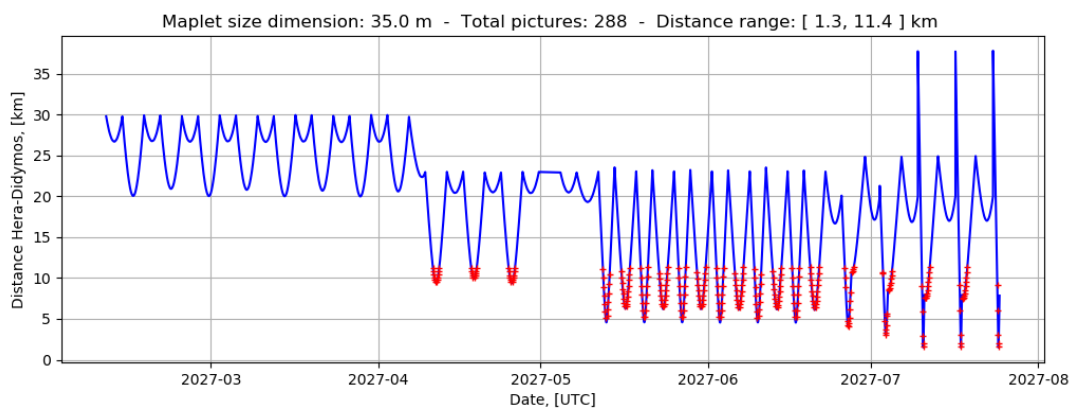
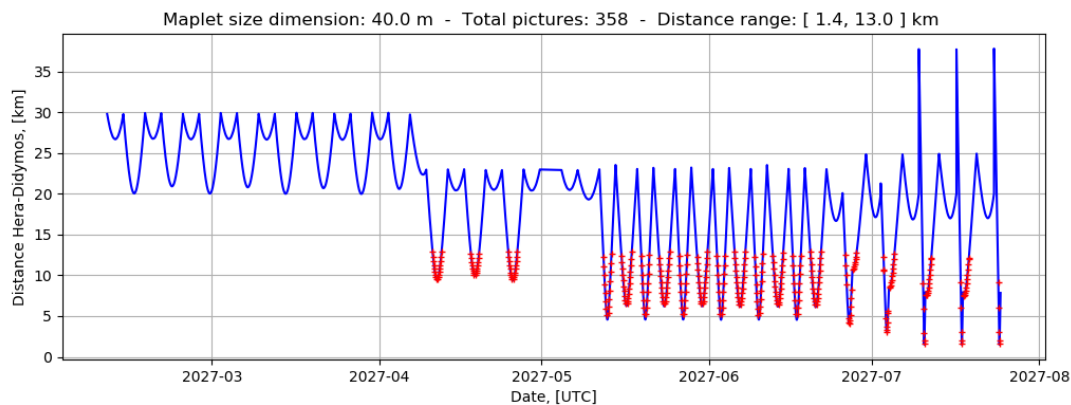
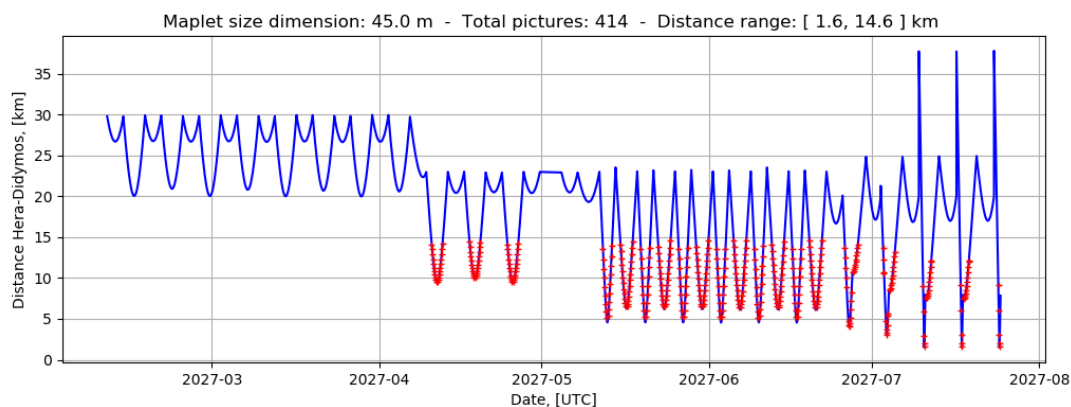
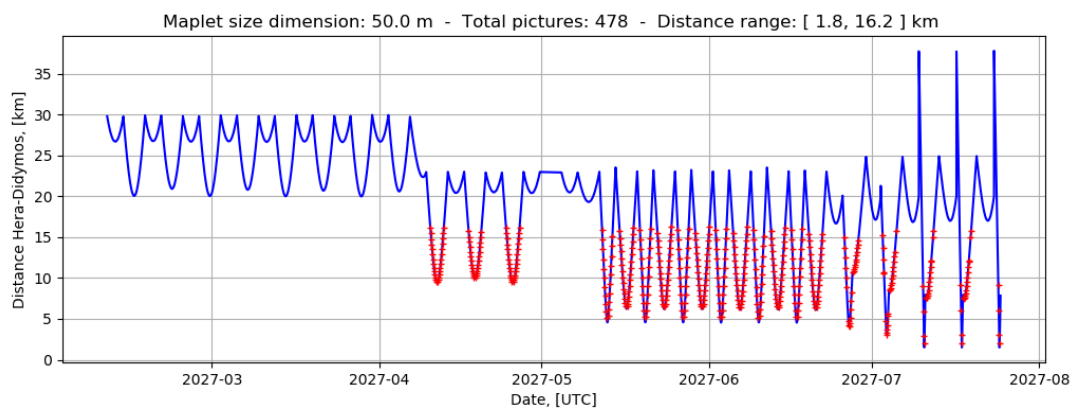


Figure 4.16: 35 m Maplet lateral side, 288 selected pictures.

Figure 4.17: 40 *m* Maplet lateral side, 358 selected pictures.Figure 4.18: 45 *m* Maplet lateral side, 414 selected pictures.Figure 4.19: 50 *m* Maplet lateral side, 478 selected pictures.

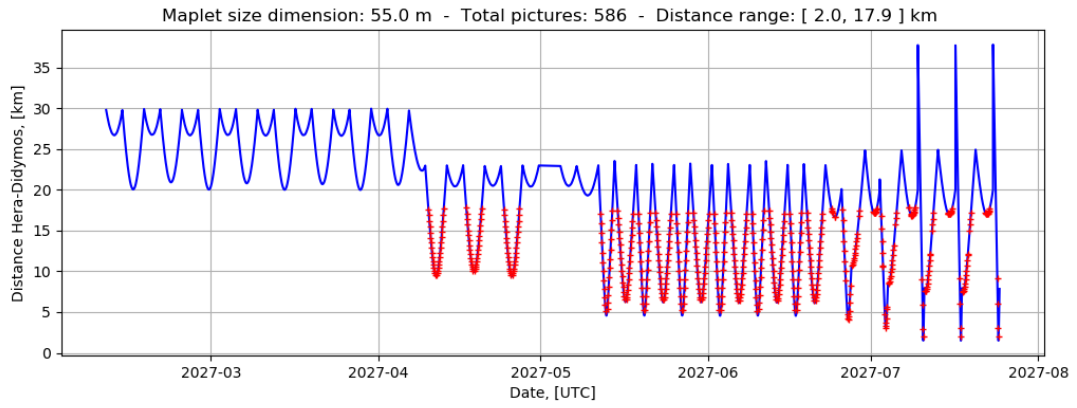


Figure 4.20: 55 m Maplet lateral side, 586 selected pictures.

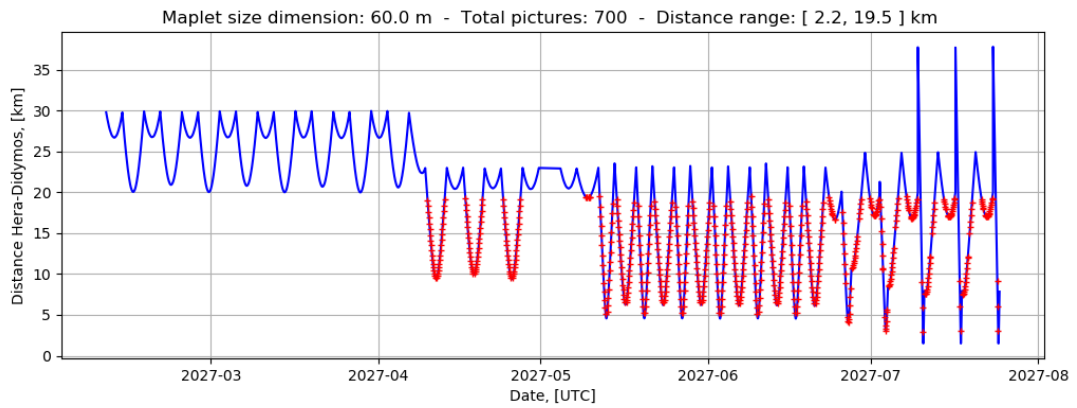


Figure 4.21: 60 m Maplet lateral side, 700 selected pictures.

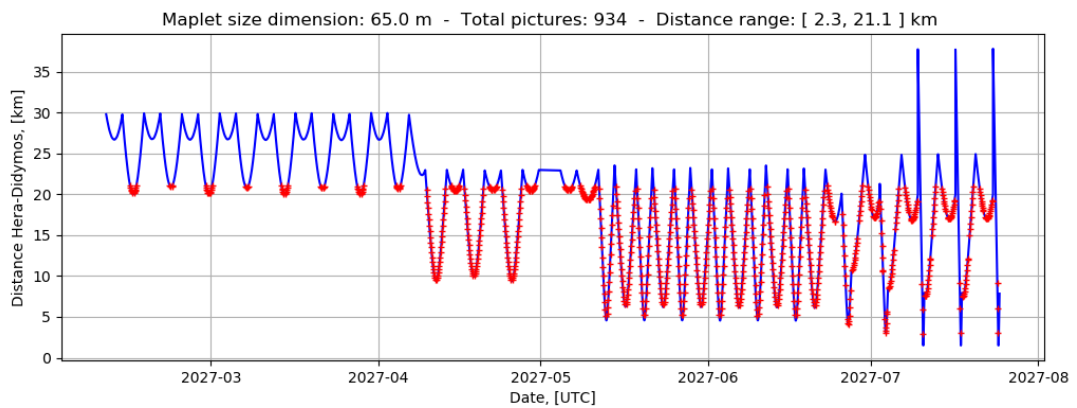


Figure 4.22: 65 m Maplet lateral side, 934 selected pictures.

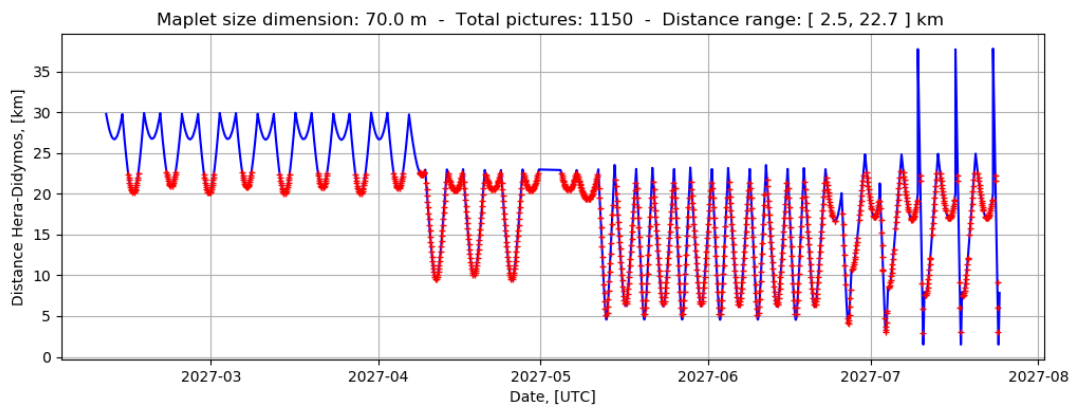


Figure 4.23: 70 *m* Maplet lateral side, 1150 selected pictures.

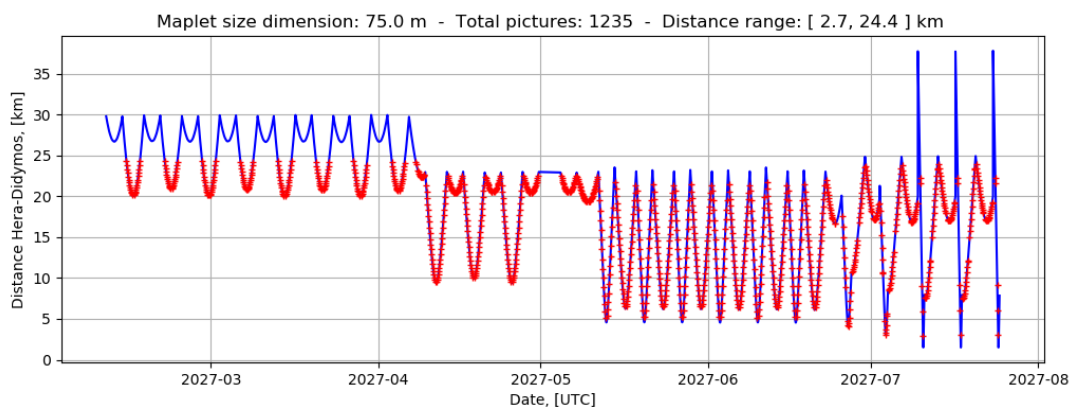


Figure 4.24: 75 *m* Maplet lateral side, 1235 selected pictures.

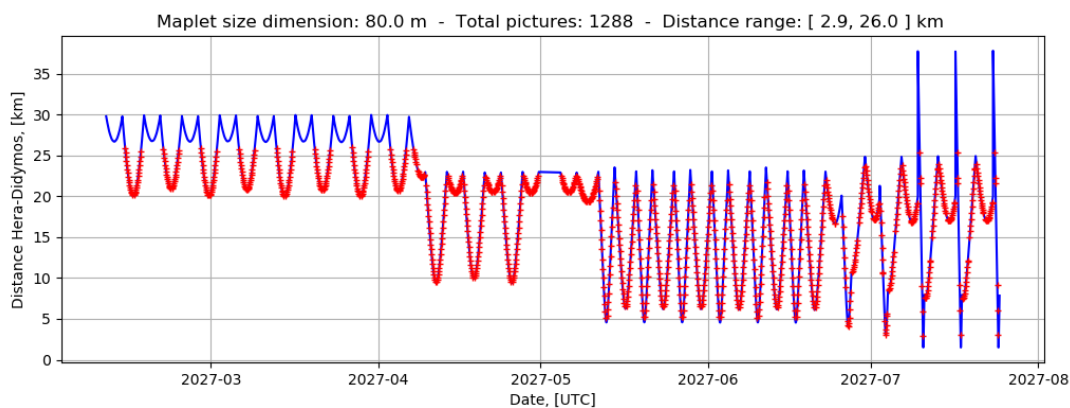


Figure 4.25: 80 *m* Maplet lateral side, 1288 selected pictures.

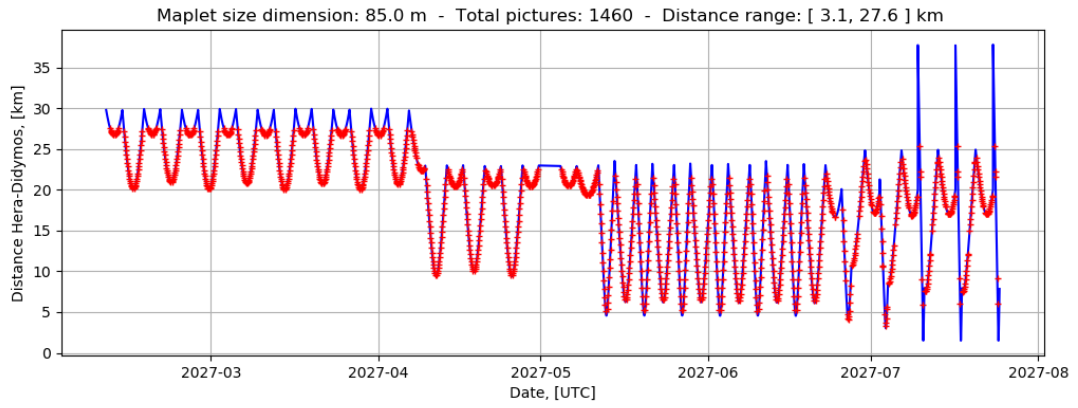


Figure 4.26: 85 m Maplet lateral side, 1460 selected pictures.

## Residuals at different minimum correlation for maplet matching

With a minimum value of maplet matching correlation allowed, it is possible to improve drastically the results of the residuals of the observables with their corresponding computed values.

Therefore, we can filter the optical observables of the maplet matching method based on the value of correlation found. The results show that the higher the correlation found, the more reliable are the observables.

The fixed parameters considered are:

- $Dimension = 40 m$ .
- $min(Occupation) = 0.3$ .

Below we show the prefit behavior based on the different values of correlation.

For **0.40 minimum maplet correlation, prefit**: see Figure 4.4.

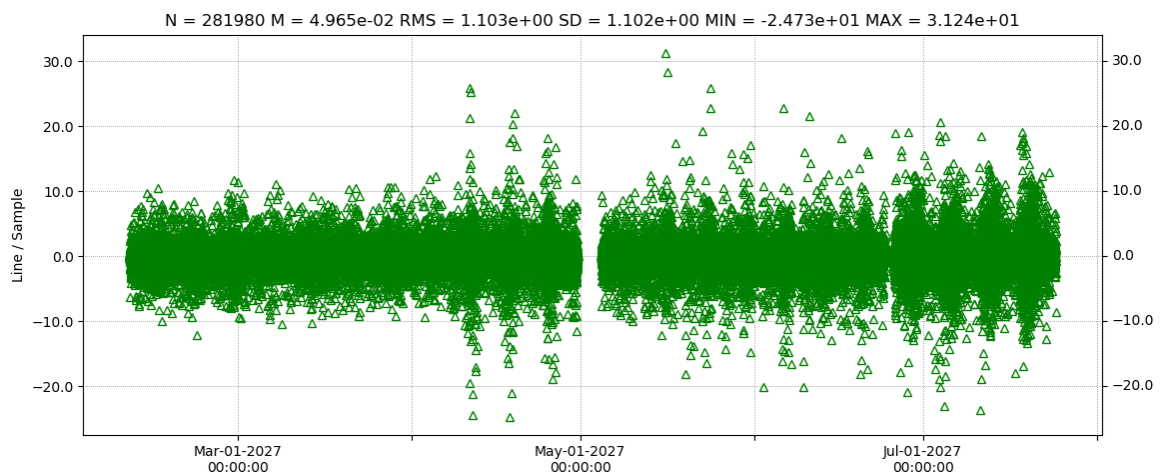


Figure 4.27: 0.45 minimum maplet correlation, prefit.

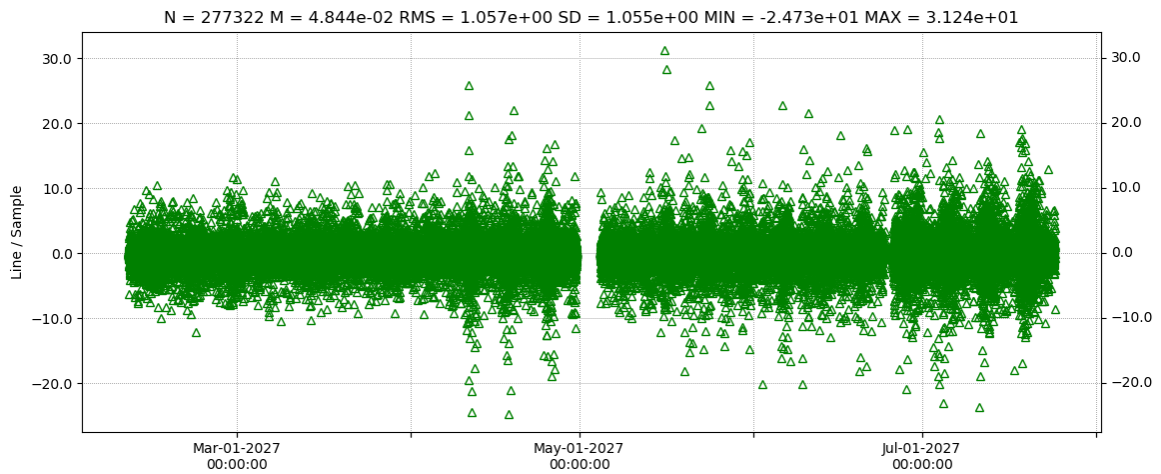


Figure 4.28: 0.50 minimum maplet correlation, profit.

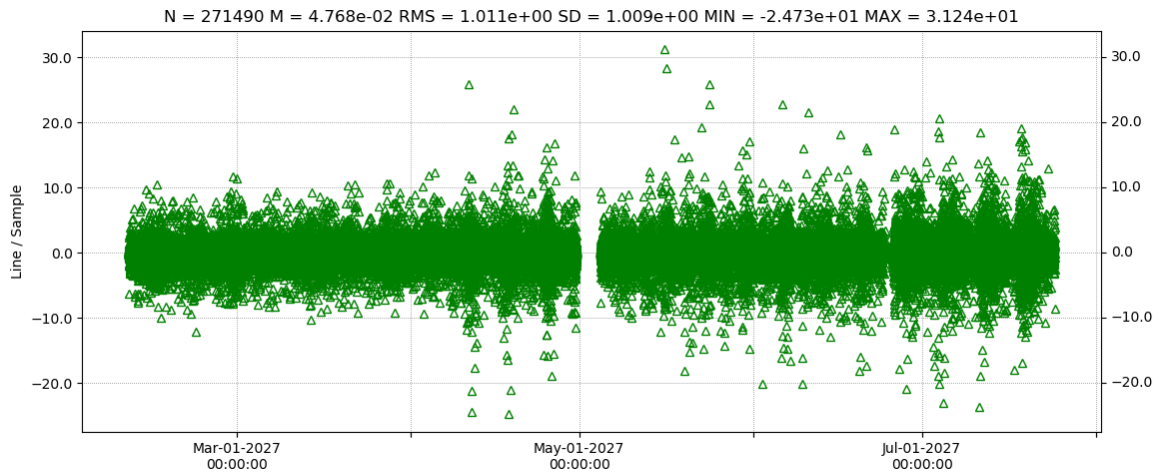


Figure 4.29: 0.55 minimum maplet correlation, profit.

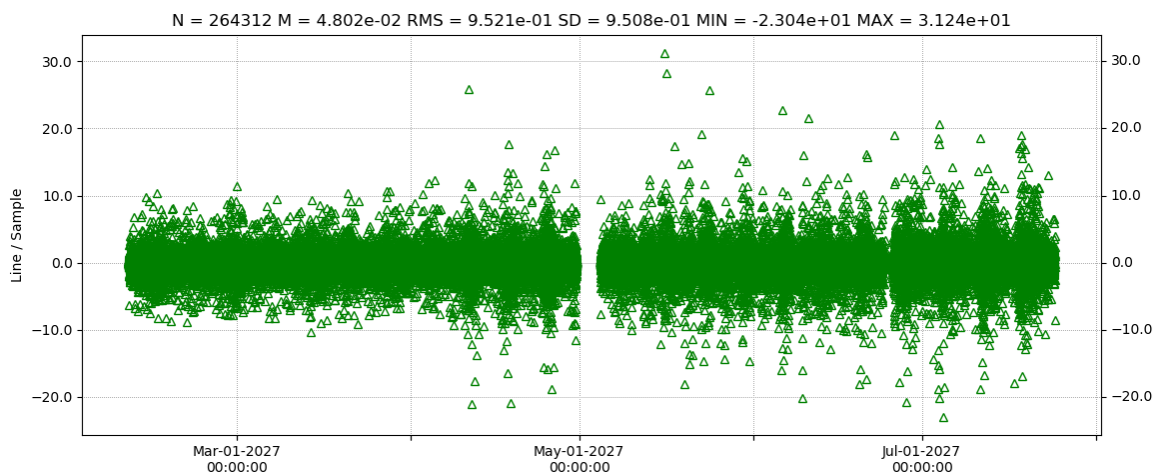


Figure 4.30: 0.60 minimum maplet correlation, profit.

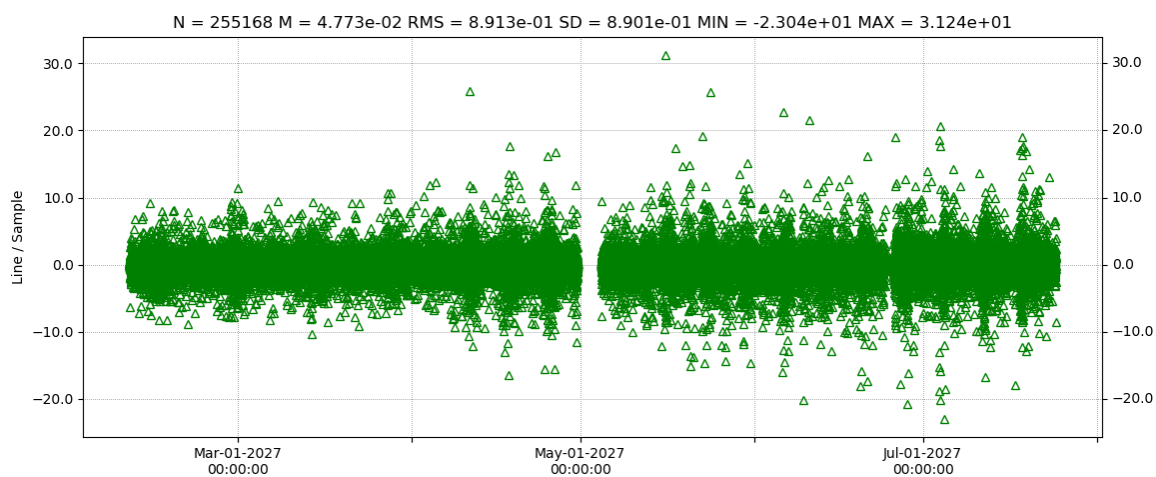


Figure 4.31: 0.65 minimum maplet correlation, profit.

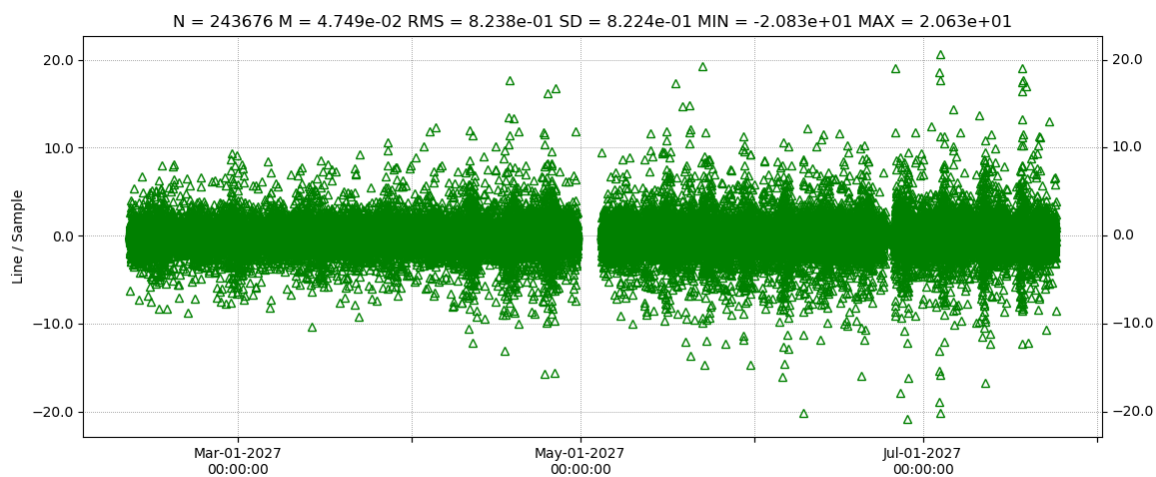


Figure 4.32: 0.70 minimum maplet correlation, profit.

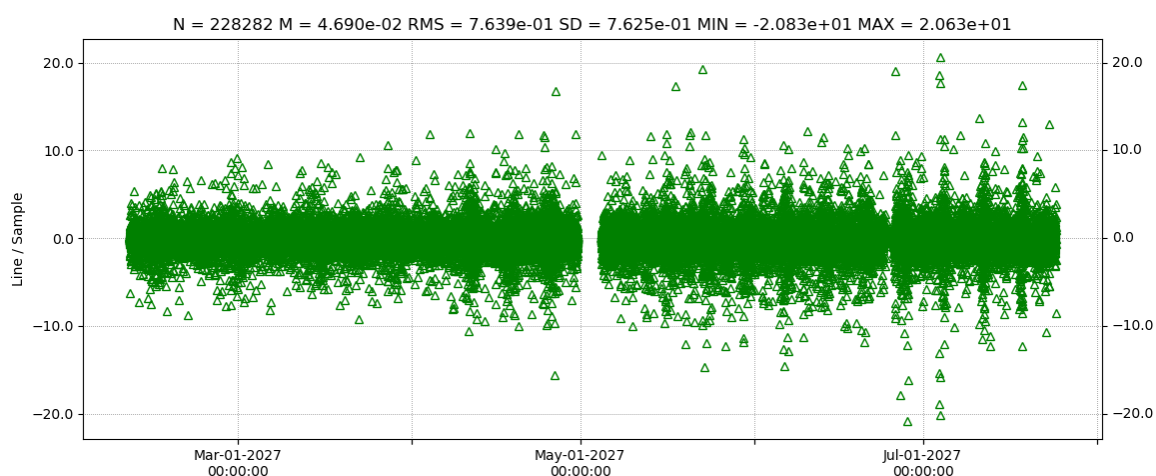


Figure 4.33: 0.75 minimum maplet correlation, profit.

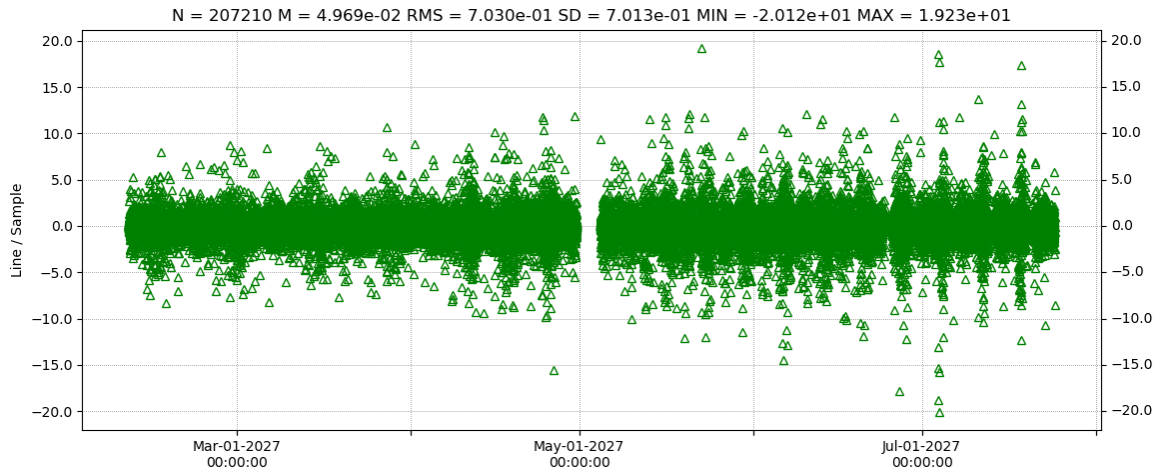


Figure 4.34: 0.80 minimum maplet correlation, profit.

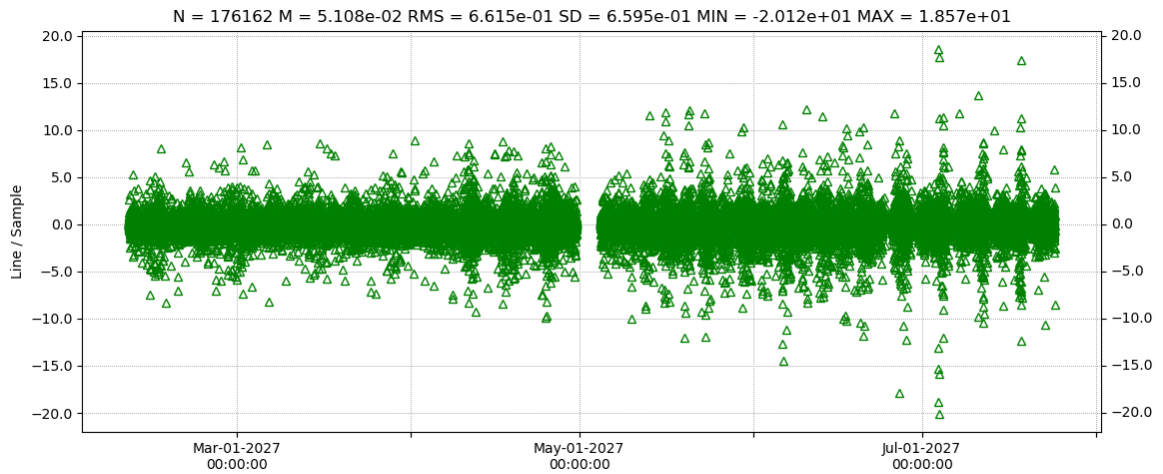


Figure 4.35: 0.85 minimum maplet correlation, profit.

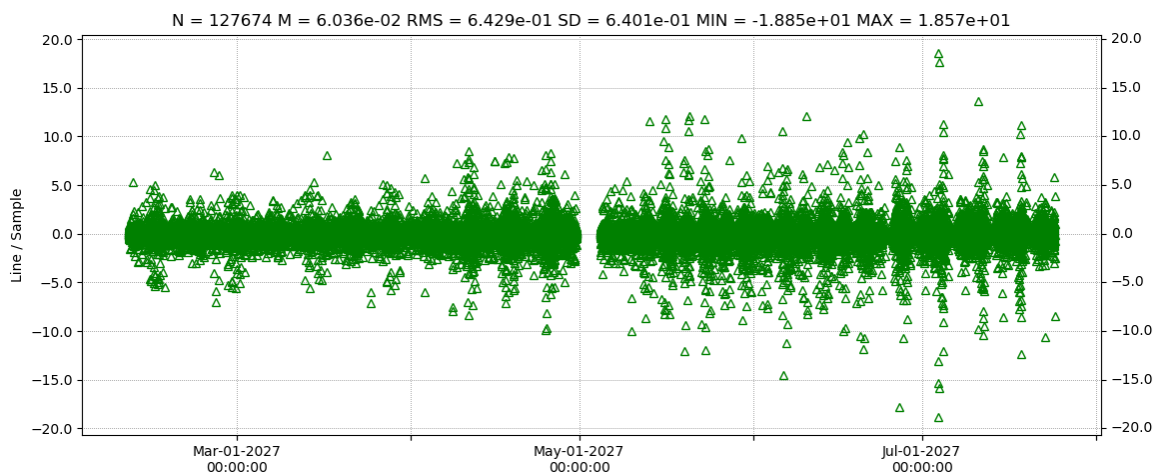


Figure 4.36: 0.90 minimum maplet correlation, profit.

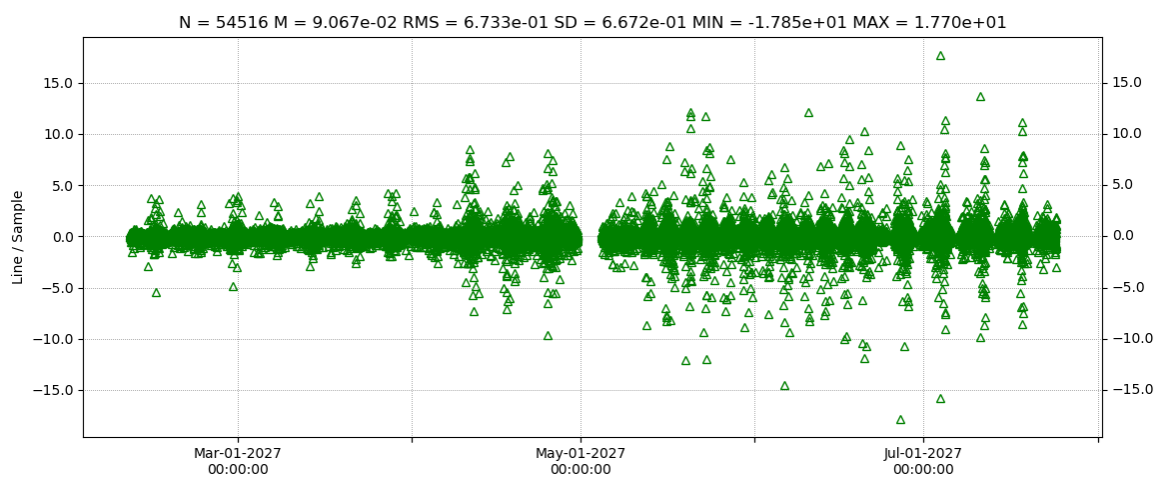


Figure 4.37: 0.95 minimum maplet correlation, prefit.

## Residuals at different minimum occupation for maplet matching

As it happens when increasing the minimum correlation value during maplet matching, also the occupation improves the resulting residuals. The occupation represents the fraction of the maplet which is not too dark (below threshold), thus best results are obtained when the image is well-lit and the correlation becomes more reliable as a consequence.

The fixed parameters considered are:

- $Dimension = 40 m$ .
- $min(Correlation) = 0.85$ .

Below we show the prefit behavior based on the different values of occupation. It should be noted that with a value of 1.0, no observables are left.

For **0.30 minimum maplet occupation, prefit**: see Figure 4.35.

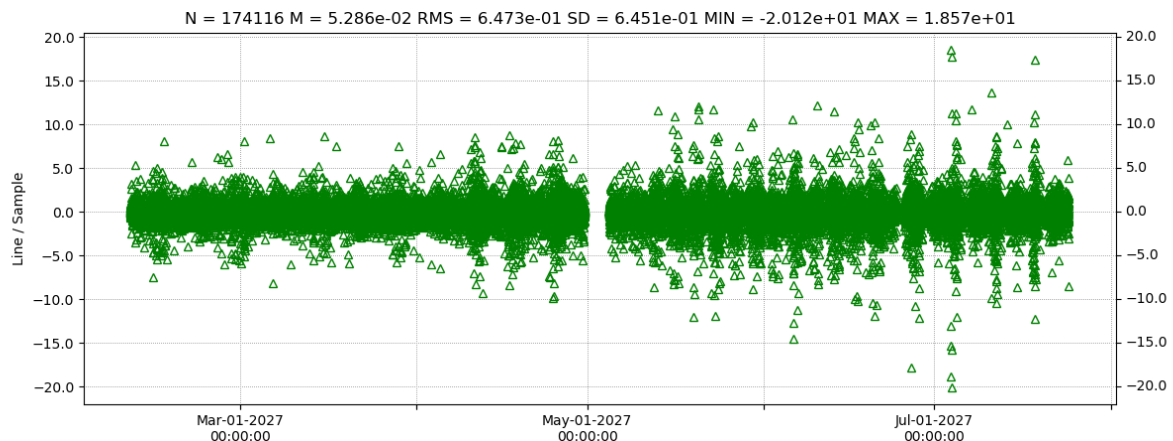


Figure 4.38: 0.40 minimum maplet occupation, prefit.

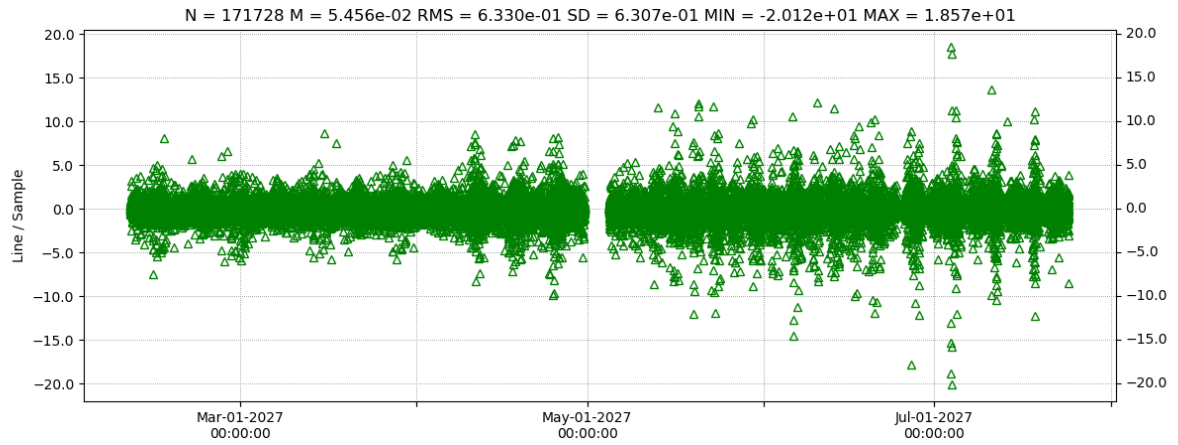


Figure 4.39: 0.50 minimum maplet occupation, profit.

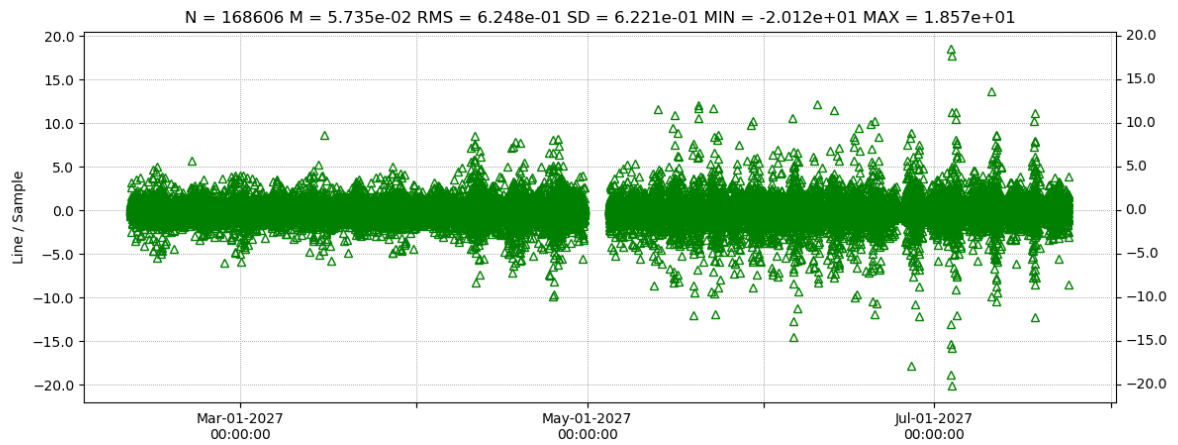


Figure 4.40: 0.60 minimum maplet occupation, profit.

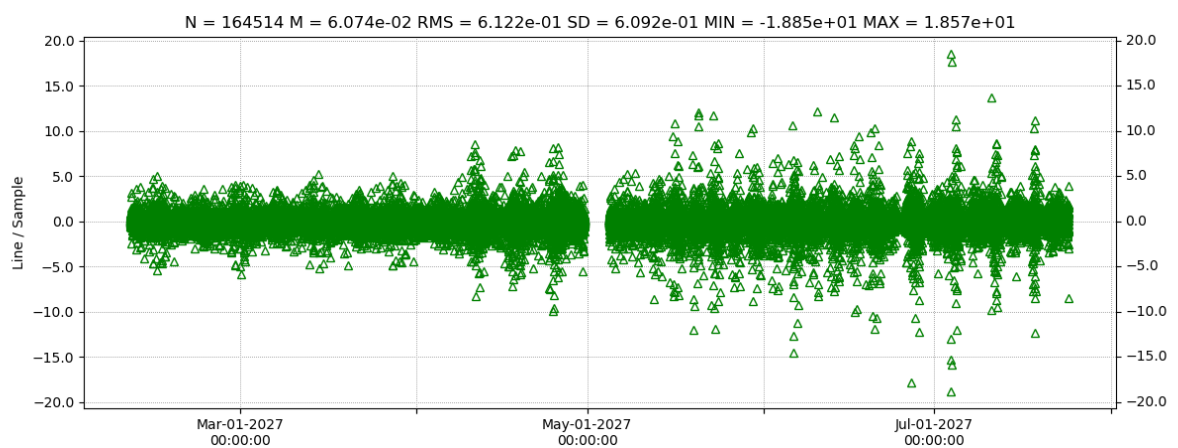


Figure 4.41: 0.70 minimum maplet occupation, profit.

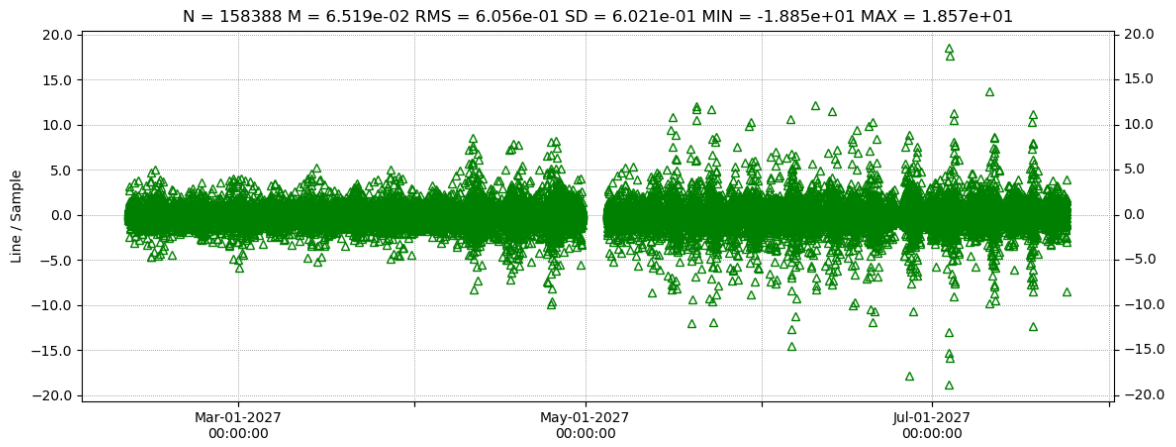


Figure 4.42: 0.80 minimum maplet occupation, profit.

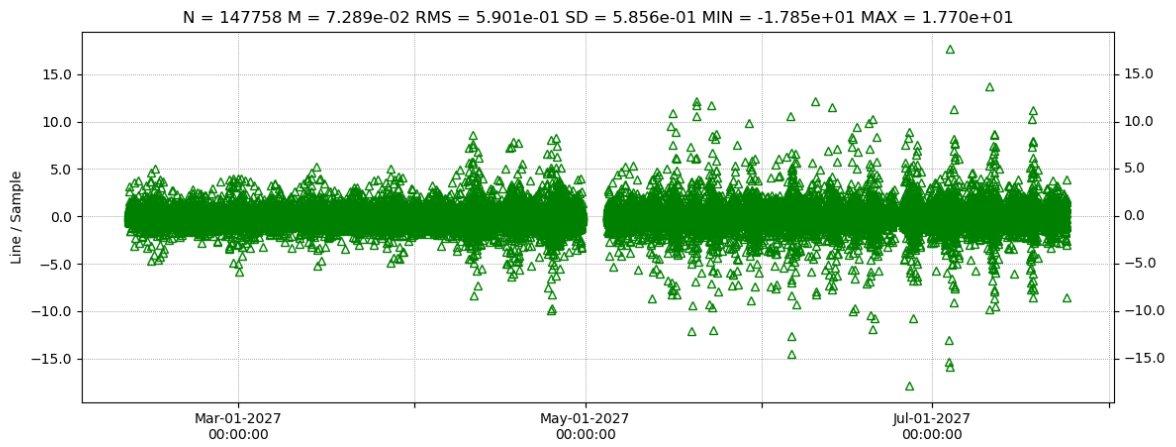


Figure 4.43: 0.90 minimum maplet occupation, profit.



# Open-source software used

This thesis extensively took advantage of open-source code and software (Geogebra [80], Blender [68], Diagrams.net [81], and different Python modules [67], [82], [83], [84], [85]-[86], [87]).

# List of Figures

Figure 1.1	Iterative orbit determination process. . . . .	5
Figure 1.2	Range two/three-way geometric description. . . . .	10
Figure 1.3	Delta-DOR configuration. . . . .	12
Figure 1.4	Dimorphos as seen by the DART spacecraft 11 seconds before im- pact. Source: <a href="https://dart.jhuapl.edu/Gallery">https://dart.jhuapl.edu/Gallery</a> , NASA/Johns Hopkins APL.	16
Figure 1.5	The Hera spacecraft and its instruments, source [1]. . . . .	18
Figure 1.6	Representation of the CMOS sensor mounted on Hera AFC. . . . .	22
Figure 1.7	The effect on the direction of momentum transfer among absorbed, reflected (specular), and diffused reflection. . . . .	26
Figure 2.1	Optical observables generation pipeline. . . . .	30
Figure 2.2	Low resolution Didymos reference model, best data available prior to the DART encounter. . . . .	32
Figure 2.3	Shape model with artificially augmented features. This comprises 786432 faces obtained by applying Perlin noise to the radial position of the shape model coordinates. . . . .	33
Figure 2.4	Height profile for the low-resolution shape model, expressed as dif- ference of the local surface position with respect to the mean radius. . . . .	34
Figure 2.5	Height profile for the augmented shape model. . . . .	34
Figure 2.6	The resulting Fibonacci Lattice on top of a spherical surface, using 200, 400, and 800 samples respectively. . . . .	35
Figure 2.7	A series of 1000 landmarks (in red), distributed as the Fibonacci Lattice and displaced on top of the surface of the augmented Didymos shape model. . . . .	36
Figure 2.8	Low and high resolution normal angular difference computed at the positions of 4000 test landmarks. . . . .	37
Figure 2.9	High level list of the geometric inputs required for the image simu- lation. . . . .	39
Figure 2.10	Hera-Didymos distance. . . . .	41
Figure 2.11	Hera-Dimorphos distance. . . . .	41
Figure 2.12	Nominal timeline setup for observable acquisition during a single arc.	42

Figure 2.13 Nominal timeline for picture acquisition (considering 4 arcs). Inside the visible gaps, only radiometric observables are intended to be collected.	43
Figure 2.14 Incidence ( $i$ ), emission ( $e$ ), and phase ( $\alpha$ ) angles for a reference surface.	43
Figure 2.15 Total number of images which satisfy the minimum filtering based on visibility and illumination conditions for each of the 4000 landmarks considered. The total available images before filtering were 3166.	45
Figure 2.16 The output of the photometric model, stored in a FITS file. Gray levels expressed in $DU$ .	50
Figure 2.17 Histogram of FITS file, with bin size of $2^{14}/500$ $DU$ . The maximum black value count (at 0 $DU$ ) exceeds the limit of the scale.	51
Figure 2.18 Maplet of a generic landmark, generated from a controlled series of fits files containing the same target under different illumination conditions.	52
Figure 2.19 Maplet creation pipeline.	53
Figure 2.20 Visibility constraint based on the relative position on the asteroid.	54
Figure 2.21 Visibility constraint with emission angle.	54
Figure 2.22 Filtering based on illumination conditions.	55
Figure 2.23 Minimum filtering based on photometric angles.	56
Figure 2.24 Mild filtering based on photometric angles.	56
Figure 2.25 Medium filtering based on photometric angles.	57
Figure 2.26 Strict filtering based on photometric angles.	57
Figure 2.27 Visibility constraint based on field of view.	58
Figure 2.28 Allowed range of distances to create a maplet with cell size $p$ .	59
Figure 2.29 Pinhole camera model and allowed maplet cell size.	60
Figure 2.30 Minimum filtering based on photometric angles, landmarks in FOV and camera at an optimal distance.	61
Figure 2.31 Mild filtering based on photometric angles, landmarks in FOV and camera at an optimal distance.	61
Figure 2.32 Medium filtering based on photometric angles, landmarks in FOV and camera at an optimal distance.	62
Figure 2.33 Strict filtering based on photometric angles, landmarks in FOV and camera at an optimal distance.	62
Figure 2.34 Pinhole reprojection of a point into the sensor pixel location.	64
Figure 2.35 Reprojected images of a landmark with different illumination conditions.	65
Figure 2.36 Classical photogrammetry technique to extract 3D location of a point from multiple pictures.	68
Figure 2.37 Maplet output of the method.	69

Figure 2.38 A maplet on the same scale as the original model used for initialization (in yellow). The superposed augmented version (in grayscale) was only used for the creation of the input images. . . . .	70
Figure 2.39 The created maplet (blue) and the corresponding region in the original high-resolution shape model (in gray). . . . .	70
Figure 2.40 From left to right, the image simulated from the high-resolution polyhedral model; a partial reconstruction of the original image using a sparse set of maplets; a simulated version with more maplets of larger size. . . . .	71
Figure 2.41 In yellow, all the landmark positions extracted from maplet matching, after being reprojected onto the original image. . . . .	73
Figure 3.1 Difference between each maplet coordinate with respect to the original reference high resolution shape model, along the radial direction. . . . .	75
Figure 3.2 RMS of the maplet errors in the radial direction with respect to the original reference high resolution shape model. . . . .	76
Figure 3.3 Maplets created with basic settings as a function of the maplet dimension. . . . .	78
Figure 3.4 Prefit sample and line residuals, expressed in pixels, for 40 $m$ sized maplets, filtered for a minimum normalized correlation coefficient of 0.4 and minimum occupation of 0.3 during maplet matching. . . . .	79
Figure 3.5 Postfit sample and line residuals, expressed in pixels, for 40 $m$ sized maplets, filtered for a minimum normalized correlation coefficient of 0.4 and minimum occupation of 0.3 during maplet matching. . . . .	80
Figure 3.6 RMS of all the postfit residuals (as both sample and line) from the estimated solve-for parameters. . . . .	81
Figure 3.7 In red, the pictures (nominal setup with $2 h$ interval) at an optimal distance for the creation of maplets whose lateral size is 40 $m$ . . . . .	81
Figure 3.8 RMS of the postfit residuals as a function of the minimum maplet matching correlation value allowed. . . . .	84
Figure 3.9 Total number of sample and lines observables as a function of the minimum maplet correlation allowed. . . . .	85
Figure 3.10 Ratio RMS and number of observables. . . . .	85
Figure 3.11 Prefit sample and line residuals, expressed in pixels, considering a maplet size of 40 $m$ , minimum maplet matching correlation allowed of 0.85, and minimum occupation of 0.3. . . . .	86
Figure 3.12 Postfit sample and line residuals, expressed in pixels, considering a maplet size of 40 $m$ , minimum maplet matching correlation allowed of 0.85, and minimum occupation of 0.3. . . . .	86
Figure 3.13 Postfit residuals as a function of the occupation factor. Maplet of 40 $m$ with 0.85 minimum maplet matching correlation is considered. . . . .	89

Figure 3.14 Prefit sample and line residuals, expressed in pixels, considering maplets of 40 $m$ , a minimum correlation of 0.85 and a minimum occupation of 0.9. . . . .	90
Figure 3.15 Postfit sample and line residuals, expressed in pixels, considering maplets of 40 $m$ , a minimum correlation of 0.85 and a minimum occupation of 0.9. . . . .	91
Figure 4.1 25 $m$ Maplet lateral side, prefit. . . . .	97
Figure 4.2 30 $m$ Maplet lateral side, prefit. . . . .	98
Figure 4.3 35 $m$ Maplet lateral side, prefit. . . . .	98
Figure 4.4 40 $m$ Maplet lateral side, prefit. . . . .	98
Figure 4.5 45 $m$ Maplet lateral side, prefit. . . . .	99
Figure 4.6 50 $m$ Maplet lateral side, prefit. . . . .	99
Figure 4.7 55 $m$ Maplet lateral side, prefit. . . . .	99
Figure 4.8 60 $m$ Maplet lateral side, prefit. . . . .	100
Figure 4.9 65 $m$ Maplet lateral side, prefit. . . . .	100
Figure 4.10 70 $m$ Maplet lateral side, prefit. . . . .	100
Figure 4.11 75 $m$ Maplet lateral side, prefit. . . . .	101
Figure 4.12 80 $m$ Maplet lateral side, prefit. . . . .	101
Figure 4.13 85 $m$ Maplet lateral side, prefit. . . . .	101
Figure 4.14 25 $m$ Maplet lateral side, 128 selected pictures. . . . .	103
Figure 4.15 30 $m$ Maplet lateral side, 189 selected pictures. . . . .	103
Figure 4.16 35 $m$ Maplet lateral side, 288 selected pictures. . . . .	103
Figure 4.17 40 $m$ Maplet lateral side, 358 selected pictures. . . . .	104
Figure 4.18 45 $m$ Maplet lateral side, 414 selected pictures. . . . .	104
Figure 4.19 50 $m$ Maplet lateral side, 478 selected pictures. . . . .	104
Figure 4.20 55 $m$ Maplet lateral side, 586 selected pictures. . . . .	105
Figure 4.21 60 $m$ Maplet lateral side, 700 selected pictures. . . . .	105
Figure 4.22 65 $m$ Maplet lateral side, 934 selected pictures. . . . .	105
Figure 4.23 70 $m$ Maplet lateral side, 1150 selected pictures. . . . .	106
Figure 4.24 75 $m$ Maplet lateral side, 1235 selected pictures. . . . .	106
Figure 4.25 80 $m$ Maplet lateral side, 1288 selected pictures. . . . .	106
Figure 4.26 85 $m$ Maplet lateral side, 1460 selected pictures. . . . .	107
Figure 4.27 0.45 minimum maplet correlation, prefit. . . . .	108
Figure 4.28 0.50 minimum maplet correlation, prefit. . . . .	109
Figure 4.29 0.55 minimum maplet correlation, prefit. . . . .	109
Figure 4.30 0.60 minimum maplet correlation, prefit. . . . .	109
Figure 4.31 0.65 minimum maplet correlation, prefit. . . . .	110
Figure 4.32 0.70 minimum maplet correlation, prefit. . . . .	110
Figure 4.33 0.75 minimum maplet correlation, prefit. . . . .	110

---

Figure 4.34	0.80 minimum maplet correlation, prefit. . . . .	111
Figure 4.35	0.85 minimum maplet correlation, prefit. . . . .	111
Figure 4.36	0.90 minimum maplet correlation, prefit. . . . .	111
Figure 4.37	0.95 minimum maplet correlation, prefit. . . . .	112
Figure 4.38	0.40 minimum maplet occupation, prefit. . . . .	113
Figure 4.39	0.50 minimum maplet occupation, prefit. . . . .	114
Figure 4.40	0.60 minimum maplet occupation, prefit. . . . .	114
Figure 4.41	0.70 minimum maplet occupation, prefit. . . . .	114
Figure 4.42	0.80 minimum maplet occupation, prefit. . . . .	115
Figure 4.43	0.90 minimum maplet occupation, prefit. . . . .	115

# List of Tables

1.1	Characteristics for the AFC. . . . .	21
1.2	Rotational parameters for the binary system. . . . .	24
1.3	Shape model parameters for the computation of the SRP acceleration in the Hera body fixed frame. . . . .	27
2.1	Obj data structure. . . . .	33
2.2	Timeline for observable collection during an arc. . . . .	42
2.3	Photometric angles' limits for different filtering levels. . . . .	55
3.1	Prefit values based on maplet dimension. Common maplet matching min- imum correlation allowed is 0.4. . . . .	82
3.2	Postfit values based on maplet dimension. Common maplet matching min- imum correlation allowed is 0.4. . . . .	83
3.3	Prefit values based on maplet matching minimum correlation. Maplet size of 40 <i>m</i> . . . . .	87
3.4	Postfit values based on maplet matching minimum correlation. Maplet size of 40 <i>m</i> . . . . .	87
3.5	Prefit residuals varying the occupation factor. . . . .	89
3.6	Postfit residuals varying the occupation factor. . . . .	89
4.1	AFC distances allowed for each maplet dimension. . . . .	102

# Bibliography

- [1] P. Michel, M. Küppers, A. C. Bagatin, B. Carry, S. Charnoz, J. de Leon, A. Fitzsimmons, P. Gordo, S. F. Green, A. Hérique, M. Juzi, Ö. Karatekin, T. Kohout, M. Lazzarin, N. Murdoch, T. Okada, E. Palomba, P. Pravec, C. Snodgrass, P. Tortora, K. Tsiganis, S. Ulamec, J.-B. Vincent, K. Wünnemann, Y. Zhang, S. D. Raducan, E. Dotto, N. Chabot, A. F. Cheng, A. Rivkin, O. Barnouin, C. Ernst, A. Stickle, D. C. Richardson, C. Thomas, M. Arakawa, H. Miyamoto, A. Nakamura, S. Sugita, M. Yoshikawa, P. Abell, E. Asphaug, R.-L. Ballouz, W. F. Bottke, D. S. Lauretta, K. J. Walsh, P. Martino, and I. Carnelli. The ESA Hera Mission: Detailed Characterization of the DART Impact Outcome and of the Binary Asteroid (65803) Didymos. *Planet. Sci. J.*, 3(7):160, July 2022.
- [2] W. M. Owen. Methods of optical navigation. In *AAS Spaceflight Mechanics Conference*, New Orleans, Louisiana, February 2011.
- [3] F. Castellini, D. Antal-Wokes, and R. P. de Santayana. Far approach Optical Navigation and Comet Photometry for the Rosetta Mission. In *25th International Symposium on Space Flight Dynamics ISSFD*, page 19, Munich, Germany, October 2015.
- [4] J. A. Christian. Optical Navigation Using Planet’s Centroid and Apparent Diameter in Image. *Journal of Guidance, Control, and Dynamics*, 38(2):192–204, February 2015.
- [5] J. Gil-Fernandez and G. Ortega-Hernando. Autonomous vision-based navigation for proximity operations around binary asteroids. *CEAS Space J*, 10(2):287–294, June 2018.
- [6] M. Pugliatti, V. Franzese, and F. Topputo. Data-Driven Image Processing for On-board Optical Navigation Around a Binary Asteroid. *Journal of Spacecraft and Rockets*, 59(3):943–959, May 2022.
- [7] W. M. Owen, T. C. Duxbury, C. H. Acton, S. P. Synnott, J. E. Riedel, and S. Bhaskaran. A brief history of Optical Navigation at JPL. In *31st Annual AAS Guidance and Control Conference*, Breckenridge, Colorado, February 2008. AAS Publications.

- [8] J. A. Christian. Accurate Planetary Limb Localization for Image-Based Spacecraft Navigation. *Journal of Spacecraft and Rockets*, 54(3):708–730, May 2017.
- [9] Y. Cheng, A. Johnson, L. Matthies, and C. Olson. *Optical Landmark Detection for Spacecraft Navigation*, volume 114. January 2003.
- [10] W. M. Owen, T. C. Wang, A. Harch, M. Bell, and C. Peterson. NEAR optical navigation at Eros. In *AAS/AIAA Astrodynamics Specialist Conference*, Quebec, Canada, July 2001.
- [11] D. G. Lowe. Distinctive Image Features from Scale-Invariant Keypoints. *International Journal of Computer Vision*, 60(2):91–110, November 2004.
- [12] H. Bay, A. Ess, T. Tuytelaars, and L. Van Gool. Speeded-Up Robust Features (SURF). *Computer Vision and Image Understanding*, 110(3):346–359, June 2008.
- [13] M. Calonder, V. Lepetit, C. Strecha, and P. Fua. BRIEF: Binary Robust Independent Elementary Features. In Kostas Daniilidis, Petros Maragos, and Nikos Paragios, editors, *Computer Vision – ECCV 2010*, Lecture Notes in Computer Science, pages 778–792, Berlin, Heidelberg, 2010. Springer.
- [14] E. Rublee, V. Rabaud, K. Konolige, and G. Bradski. ORB: An efficient alternative to SIFT or SURF. In *2011 International Conference on Computer Vision*, pages 2564–2571, November 2011. ISSN: 2380-7504.
- [15] S. Leutenegger, M. Chli, and R. Y. Siegwart. BRISK: Binary Robust invariant scalable keypoints. In *2011 International Conference on Computer Vision*, pages 2548–2555, Barcelona, Spain, November 2011.
- [16] S. Silvestrini, M. Piccinin, G. Zanotti, A. Brandonisio, I. Bloise, L. Feruglio, P. Lunghi, M. Lavagna, and M. Varile. Optical navigation for Lunar landing based on Convolutional Neural Network crater detector. *Aerospace Science and Technology*, 123:107503, April 2022.
- [17] D. A. Vallado. *Fundamentals of Astrodynamics and Applications*. Space Technology Library. Springer New York, 2007.
- [18] G. J. Bierman. *Factorization Methods for Discrete Sequential Estimation*. Dover Books on Mathematics. Dover Publications, Mineola, N.Y., 2006.
- [19] B. Schutz, B. Tapley, and G. H. Born. *Statistical Orbit Determination*. Elsevier Science, 2004.

- 
- [20] N. G. Dias, B. N. Arribas, P. Gordo, T. Sousa, J. Marinho, R. Melicio, A. Amorim, B. Livio, and P. Michel. HERA Mission LIDAR Mechanical and Optical Design. *IOP Conf. Ser.: Mater. Sci. Eng.*, 1226(1):012094, February 2022.
- [21] L. Rey, P. de Chateau-Thierry, L. Phalippou, C. Mavrocordatos, and R. Francis. SIRAL: the radar altimeter for CryoSat mission, under development. In *IEEE International Geoscience and Remote Sensing Symposium*, volume 3, pages 1768–1770, June 2002.
- [22] F. Santoli, F. Emiliano, C. Lefevre, D. M. Lucchesi, M. Lucente, C. Magnifico, A. Morbidini, R. Peron, and V. Iafolla. ISA, a High Sensitivity Accelerometer in the Interplanetary Space: Updates after the Near-Earth Commissioning Phase of Italian Spring Accelerometer. *Space Sci Rev*, 216(8):145, December 2020.
- [23] C. L. Thornton and J. S. Border. *Radiometric Tracking Techniques for Deep Space Navigation*. John Wiley & Sons, Inc., Hoboken, NJ, USA, January 2003.
- [24] CCSDS. *Pseudo-Noise (PN) Ranging Systems*. Recommendation for Space Data System Standards (Blue Book), CCSDS 414.1-B-3. CCSDS, Washington, DC, USA, 3rd edition, January 2022.
- [25] W. J. Riley. *Handbook of Frequency Stability Analysis*. National Institute of Standards and Technology, Washington, nist special publication 1065 edition, July 2008.
- [26] A. Kwok and D. K. Shin. *Frequency and Channel Assignments, 201, Rev. B*, volume DSN Telecommunications Link, Design Handbook, 810-005, Rev. E. California Institute of Technology, December 2009.
- [27] N. James, R. Abello, M. Lanucara, M. Mercolino, and R. Maddè. Implementation of an ESA delta-DOR capability. *Acta Astronautica*, 64(11):1041–1049, June 2009.
- [28] S. Bhaskaran, S. D. Desai, P. J. Dumont, B. M. Kennedy, G. W. Null, W. M. Jr. Owen, J. E. Riedel, S. P. Synnott, and R. A. Werner. Orbit Determination Performance Evaluation of the Deep Space 1 Autonomous Navigation System. In *Spaceflight Mechanics Meeting*, page 20, Monterey, CA, U.S.A., February 1998.
- [29] S. E. Hawkins, J. D. Boldt, E. H. Darlington, R. Espiritu, R. E. Gold, B. Gotwols, M. P. Grey, C. D. Hash, J. R. Hayes, S. E. Jaskulek, C. J. Kardian, M. R. Keller, E. R. Malaret, S. L. Murchie, P. K. Murphy, K. Peacock, L. M. Prockter, R. A. Reiter, M. S. Robinson, E. D. Schaefer, R. G. Shelton, R. E. Sterner, H. W. Taylor, T. R. Watters, and B. D. Williams. The Mercury Dual Imaging System on the MESSENGER Spacecraft. *Space Sci Rev*, 131(1):247–338, August 2007.

- [30] G. Cremonese, F. Capaccioni, M. T. Capria, A. Doressoundiram, P. Palumbo, M. Vincendon, M. Massironi, S. Debei, M. Zusi, F. Altieri, M. Amoroso, G. Aroldi, M. Baroni, A. Barucci, G. Bellucci, J. Benkhoff, S. Besse, C. Bettanini, M. Blecka, D. Borrelli, J. R. Brucato, C. Carli, V. Carlier, P. Cerroni, A. Cicchetti, L. Colanageli, M. Dami, V. Da Deppo, V. Della Corte, M. C. De Sanctis, S. Erard, F. Esposito, D. Fantinel, L. Ferranti, F. Ferri, I. Fikai Veltroni, G. Filacchione, E. Flamini, G. Forlani, S. Fornasier, O. Forni, M. Fulchignoni, V. Galluzzi, K. Gwinner, W. Ip, L. Jorda, Y. Langevin, L. Lara, F. Leblanc, C. Leyrat, Y. Li, S. Marchi, L. Marinangeli, F. Marzari, E. Mazzotta Epifani, M. Mendillo, V. Mennella, R. Mugnuolo, K. Muinonen, G. Naletto, R. Noschese, E. Palomba, R. Paolinetti, D. Perna, G. Piccioni, R. Politi, F. Poulet, R. Ragazzoni, C. Re, M. Rossi, A. Rotundi, G. Salemi, M. Sgavetti, E. Simioni, N. Thomas, L. Tommasi, A. Turella, T. Van Hoolst, L. Wilson, F. Zambon, A. Aboudan, O. Barraud, N. Bott, P. Borin, G. Colombatti, M. El Yazidi, S. Ferrari, J. Flahaut, L. Giacomini, L. Guzzetta, A. Lucchetti, E. Martellato, M. Pajola, A. Slemer, G. Tognon, and D. Turrini. SIMBIO-SYS: Scientific Cameras and Spectrometer for the BepiColombo Mission. *Space Sci Rev*, 216(5):75, August 2020.
- [31] F. Preusker, J. Oberst, J. W. Head, T. R. Watters, M. S. Robinson, M. T. Zuber, and S. C. Solomon. Stereo topographic models of Mercury after three MESSENGER flybys. *Planetary and Space Science*, 59(15):1910–1917, December 2011.
- [32] K. J. Becker, B. A. Archinal, T. Hare, R. L. Kirk, E. Howington-Kraus, M. S. Robinson, and M. R. Rosiek. Criteria for automated identification of stereo image Pairs. In *46th Lunar and Planetary Science Conference Abstracts*, Houston, U.S.A., March 2015.
- [33] R. W. Gaskell, O. S. Barnouin-Jha, D. J. Scheeres, A. S. Konopliv, T. Mukai, S. Abe, J. Saito, M. Ishiguro, T. Kubota, T. Hashimoto, J. Kawaguchi, M. Yoshikawa, K. Shirakawa, T. Kominato, N. Hirata, and H. Demura. Characterizing and navigating small bodies with imaging data. *Meteoritics & Planetary Science*, 43(6):1049–1061, 2008.
- [34] R. W. Gaskell. Optical navigation near small bodies. *Advances in the Astronautical Sciences*, 140:1705–1717, January 2011.
- [35] P. Michel, A. Cheng, M. Küppers, P. Pravec, J. Blum, M. Delbo, S. F. Green, P. Rosenblatt, K. Tsiganis, J. B. Vincent, J. Biele, V. Ciarletti, A. Hérique, S. Ulamec, I. Carnelli, A. Galvez, L. Benner, S. P. Naidu, O. S. Barnouin, D. C. Richardson, A. Rivkin, P. Scheirich, N. Moskovitz, A. Thirouin, S. R. Schwartz, A. Campo Bagatin, and Y. Yu. Science case for the Asteroid Impact Mission (AIM):

- 
- A component of the Asteroid Impact & Deflection Assessment (AIDA) mission. *Advances in Space Research*, 57:2529–2547, June 2016.
- [36] A. F. Cheng, A. S. Rivkin, P. Michel, J. Atchison, O. Barnouin, L. Benner, N. L. Chabot, C. Ernst, E. G. Fahnestock, M. Kueppers, P. Pravec, E. Rainey, D. C. Richardson, A. M. Stickle, and C. Thomas. AIDA DART asteroid deflection test: Planetary defense and science objectives. *Planetary and Space Science*, 157:104–115, August 2018.
- [37] R. P. Binzel, F. E. DeMeo, E. V. Turtelboom, S. J. Bus, A. Tokunaga, T. H. Burbine, C. Lantz, D. Polishook, B. Carry, A. Morbidelli, M. Birlan, P. Vernazza, B. J. Burt, N. Moskovitz, S. M. Slivan, C. A. Thomas, A. S. Rivkin, M. D. Hicks, T. Dunn, V. Reddy, J. A. Sanchez, M. Granvik, and T. Kohout. Compositional distributions and evolutionary processes for the near-Earth object population: Results from the MIT-Hawaii Near-Earth Object Spectroscopic Survey (MITHNEOS). *Icarus*, 324:41–76, May 2019.
- [38] S. P. Naidu, L. A. M. Benner, M. Brozovic, M. C. Nolan, S. J. Ostro, J. L. Margot, J. D. Giorgini, T. Hirabayashi, D. J. Scheeres, P. Pravec, P. Scheirich, C. Magri, and J. S. Jao. Radar observations and a physical model of binary near-Earth asteroid 65803 Didymos, target of the DART mission. *Icarus*, 348, September 2020.
- [39] A. S. Rivkin, N. L. Chabot, A. M. Stickle, C. A. Thomas, D. C. Richardson, O. Barnouin, E. G. Fahnestock, C. M. Ernst, A. F. Cheng, S. Chesley, S. Naidu, T. S. Statler, B. Barbee, H. Agrusa, N. Moskovitz, R. T. Daly, P. Pravec, P. Scheirich, E. Dotto, V. D. Corte, P. Michel, M. Küppers, J. Atchison, and M. Hirabayashi. The Double Asteroid Redirection Test (DART): Planetary Defense Investigations and Requirements. *Planet. Sci. J.*, 2(5):173, August 2021.
- [40] A. Cheng, H. Agrusa, B. Barbee, A. Meyer, T. Farnham, S. Raducan, D. Richardson, E. Dotto, A. Zinzi, V. Della Corte, T. Statler, S. Chesley, S. Naidu, M. Hirabayashi, J.-Y. Li, S. Eggl, O. Barnouin, N. Chabot, S. Chocron, G. Collins, R. Daly, T. Davison, M. DeCoster, C. Ernst, F. Ferrari, D. Graninger, S. Jacobson, M. Jutzi, K. Kumamoto, R. Luther, J. Lyzhoft, P. Michel, N. Murdoch, R. Nakano, E. Palmer, A. Rivkin, D. Scheeres, A. Stickle, J. Sunshine, J. Trigo-Rodriguez, J.-B. Vincent, J. Walker, K. Wünnemann, Y. Zhang, M. Amoroso, I. Bertini, J. Brucato, A. Cappanolo, G. Cremonese, M. Dallora, P. Deshapriya, I. Gai, P. Hasselmann, S. Ieva, G. Impresario, S. Ivanovski, M. Lavagna, A. Lucchetti, E. M. Epifani, D. Modenini, M. Pajola, P. Palumbo, D. Perna, S. Pirotta, G. Poggiali, A. Rossi, P. Tortora, M. Zannoni, and G. Zanotti. Momentum Transfer from the DART Mission Kinetic Impact on Asteroid Dimorphos. preprint, In Review, December 2022.

- [41] P. Tortora and V. Di Tana. LICIACube, the Italian Witness of DART Impact on Didymos. In *2019 IEEE 5th International Workshop on Metrology for AeroSpace (MetroAeroSpace)*, pages 314–317, June 2019.
- [42] F. Ferrari, V. Franzese, M. Pugliatti, C. Giordano, and F. Topputo. Preliminary mission profile of Hera’s Milani CubeSat. *Advances in Space Research*, 67(6):2010–2029, March 2021.
- [43] H. R. Goldberg, Ö. Karatekin, B. Ritter, A. Herique, P. Tortora, C. Prioroc, B. G. Gutierrez, P. Martino, and I. Carnelli. The Juventas CubeSat in Support of ESA’s Hera Mission to the Asteroid Didymos. In *33rd Annual AIAA/USU Conference on Small Satellites*, page 7, Logan, Utah, USA, August 2019.
- [44] T. Okada, T. Fukuhara, S. Tanaka, N. Sakatani, Y. Shimaki, T. Arai, H. Senshu, H. Demura, T. Kouyama, and T. Sekiguchi. Thermal Infrared Imager Onboard Hera to Observe S-Type Binary Asteroid Didymos. In *52nd Lunar and Planetary Science Conference*, March 2021.
- [45] M. Zannoni, G. Tommei, D. Modenini, P. Tortora, R. Mackenzie, M. Scoubeau, U. Herfort, and I. Carnelli. Radio science investigations with the Asteroid impact mission. *Advances in Space Research*, 62(8):2273–2289, October 2018.
- [46] S. Evans, W. Taber, T. Drain, J. Smith, H. Wu, M. Guevara, R. Sunseri, and J. Evans. MONTE: the next generation of mission design and navigation software. *CEAS Space J*, 10(1):79–86, March 2018.
- [47] M. Costa. SPICE for ESA Planetary Missions: geometry and visualization support to studies, operations and data analysis within your reach. In *2018 SpaceOps Conference*, SpaceOps Conferences. American Institute of Aeronautics and Astronautics, May 2018.
- [48] C. Acton, N. Bachman, B. Semenov, and E. Wright. A look towards the future in the handling of space science mission geometry. *Planetary and Space Science*, 150:9–12, January 2018.
- [49] HERA Didymos Reference Model. ESA-TECSP-AD-017258 Issue 5, Rev3, February 2020.
- [50] S. P. Naidu, S. R. Chesley, D. Farnocchia, N. Moskovitz, P. Pravec, P. Scheirich, C. Thomas, and A. S. Rivkin. Anticipating the DART Impact: Orbit Estimation of Dimorphos Using a Simplified Model. *Planet. Sci. J.*, 3(10):234, October 2022.
- [51] S. J. Ostro, J.-L. Margot, L. A. M. Benner, J. D. Giorgini, D. J. Scheeres, E. G. Fahnestock, S. B. Broschart, J. Bellerose, M. C. Nolan, C. Magri, P. Pravec, P. Scheirich,

- 
- R. Rose, R. F. Jurgens, E. M. De Jong, and S. Suzuki. Radar Imaging of Binary Near-Earth Asteroid (66391) 1999 KW4. *Science*, 314(5803):1276–1280, November 2006.
- [52] S. J. Ostro and R. Connelly. Convex profiles from asteroid lightcurves. *Icarus*, 57(3):443–463, March 1984.
- [53] P. Pravec, C. A. Thomas, A. S. Rivkin, P. Scheirich, N. Moskovitz, M. M. Knight, C. Snodgrass, J. de León, J. Licandro, M. Popescu, A. Thirouin, D. Föhring, C. O. Chandler, W. J. Oldroyd, C. A. Trujillo, E. S. Howell, S. F. Green, J. Thomas-Osip, S. S. Sheppard, T. L. Farnham, E. Mazzotta Epifani, E. Dotto, S. Ieva, M. Dall’Ora, R. Kokotanekova, B. Carry, and D. Souami. Photometric Observations of the Binary Near-Earth Asteroid (65803) Didymos in 2015–2021 Prior to DART Impact. *Planet. Sci. J.*, 3(7):175, July 2022.
- [54] M. C. Nolan, C. Magri, E. S. Howell, L. A. M. Benner, J. D. Giorgini, C. W. Hergenrother, R. S. Hudson, D. S. Lauretta, J.-L. Margot, S. J. Ostro, and D. J. Scheeres. Shape model and surface properties of the OSIRIS-REx target Asteroid (101955) Bennu from radar and lightcurve observations. *Icarus*, 226(1):629–640, September 2013.
- [55] R. S. Park, W. M. Folkner, J. G. Williams, and D. H. Boggs. The JPL Planetary and Lunar Ephemerides DE440 and DE441. *AJ*, 161(3):105, February 2021. Publisher: The American Astronomical Society.
- [56] S. R. Chesley, D. Farnocchia, and S. P. Naidu. Asteroid (65803) Didymos Ephemeris Delivery, JPL Solution 181. JPL IOM 392R-21-003, February 2021.
- [57] S. P. Naidu, S. R. Chesley, and D. Farnocchia. Updated orbit of Dimorphos, the satellite of binary near-Earth asteroid (65803) Didymos. JPL IOM 392R-21-004, February 2021.
- [58] M. A. Wieczorek and R. J. Phillips. Potential anomalies on a sphere: Applications to the thickness of the lunar crust. *Journal of Geophysical Research: Planets*, 103(E1):1715–1724, 1998.
- [59] *I. H. Lambert, Photometria sive de mensura et gradibus luminis, colorum et umbrae.* sumptibus vidvae Eberhardi Klett., Augustae Vindelicorum, Augsburg, 1760.
- [60] R. P. de Santayana, M. Lauer, P. Muñoz, and F. Castellini. Surface characterization and optical navigation at the Rosetta flyby of asteroid Lutetia. In *24th International Symposium on Space Flight Dynamics*, page 17, Laurel, Maryland, USA, May 2014.

- [61] A. S. Konopliv, S. W. Asmar, B. G. Bills, N. Mastrodemos, R. S. Park, C. A. Raymond, D. E. Smith, and M. T. Zuber. The Dawn Gravity Investigation at Vesta and Ceres. *Space Sci Rev*, 163(1-4):461–486, December 2011.
- [62] H. U. Keller, C. Barbieri, P. Lamy, H. Rickman, R. Rodrigo, K.-P. Wenzel, H. Sierks, M. F. A’Hearn, F. Angrilli, M. Angulo, M. E. Bailey, P. Barthol, M. A. Barucci, J.-L. Bertaux, G. Bianchini, J.-L. Boit, V. Brown, J. A. Burns, I. Büttner, J. M. Castro, G. Cremonese, W. Curdt, V. Da Deppo, S. Debei, M. De Cecco, K. Dohlen, S. Fornasier, M. Fulle, D. Germerott, F. Gliem, G. P. Guizzo, S. F. Hviid, W.-H. Ip, L. Jorda, D. Koschny, J. R. Kramm, E. Kührt, M. Küppers, L. M. Lara, A. Llebaria, A. López, A. López-Jimenez, J. López-Moreno, R. Meller, H. Michalik, M. D. Michelena, R. Müller, G. Naletto, A. Origné, G. Parzianello, M. Pertile, C. Quintana, R. Ragazzoni, P. Ramous, K.-U. Reiche, M. Reina, J. Rodríguez, G. Rousset, L. Sabau, A. Sanz, J.-P. Sivan, K. Stöckner, J. Tabero, U. Telljohann, N. Thomas, V. Timon, G. Tomasch, T. Wittrock, and M. Zaccariotto. OSIRIS – The Scientific Camera System Onboard Rosetta. *Space Sci Rev*, 128(1-4):433–506, May 2007.
- [63] R. P. de Santayana and M. Lauer. Optical measurements for Rosetta navigation near the comet. In *25th International Symposium on Space Flight Dynamics ISSFD*, page 19, Munich, Germany, October 2015.
- [64] J. Weirich, E. E. Palmer, M. G. Daly, O. S. Barnouin, K. Getzandanner, J. N. Kidd, C. D. Adam, R. Gaskell, and D. S. Laretta. Quality Assessment of Stereophotoclinometry as a Shape Modeling Method Using a Synthetic Asteroid. *Planet. Sci. J.*, 3(5):103, May 2022.
- [65] Á. González. Measurement of Areas on a Sphere Using Fibonacci and Latitude–Longitude Lattices. *Math Geosci*, 42(1):49–64, January 2010.
- [66] T. Möller and B. Trumbore. Fast, Minimum Storage Ray-Triangle Intersection. *Journal of Graphics Tools*, 2(1):21–28, January 1997.
- [67] P. Virtanen, R. Gommers, T. E. Oliphant, M. Haberland, T. Reddy, D. Cournapeau, E. Burovski, P. Peterson, W. Weckesser, J. Bright, S. J. van der Walt, M. Brett, J. Wilson, K. J. Millman, N. Mayorov, A. R. J. Nelson, E. Jones, R. Kern, E. Larson, C. J. Carey, Í. Polat, Y. Feng, E. W. Moore, J. VanderPlas, D. Laxalde, J. Perktold, R. Cimrman, I. Henriksen, E. A. Quintero, C. R. Harris, A. M. Archibald, A. H. Ribeiro, F. Pedregosa, and P. van Mulbregt. SciPy 1.0: fundamental algorithms for scientific computing in Python. *Nat Methods*, 17(3), March 2020.
- [68] Blender - a 3D modelling and rendering package.

- 
- [69] A. S. McEwen. Photometric functions for photoclinometry and other applications. *Icarus*, 92(2):298–311, August 1991.
- [70] L. B. Wolff. *Generalizing Lambert’s Law for smooth surfaces*, volume 1065. Springer Berlin Heidelberg, Berlin, Heidelberg, 1996.
- [71] W. D. Pence, L. Chiappetti, C. G. Page, R. A. Shaw, and E. Stobie. Definition of the Flexible Image Transport System ( *FITS* ), version 3.0. *A&A*, 524:A42, December 2010.
- [72] E. E. Palmer, R. Gaskell, M. G. Daly, O. S. Barnouin, C. D. Adam, and D. S. Lauretta. Practical Stereophotoclinometry for Modeling Shape and Topography on Planetary Missions. *Planet. Sci. J.*, 3(5):102, May 2022.
- [73] R. W. Gaskell. Landmark Navigation and target characterization in a simulated Itokawa encounter. In *Astrodynamics Specialists Conference*, Lake Tahoe, California, USA, 2005.
- [74] R. T. Daly, C. M. Ernst, O. S. Barnouin, R. W. Gaskell, E. E. Palmer, H. Nair, R. C. Espiritu, S. Hasnain, D. Waller, A. M. Stickle, M. C. Nolan, J. M. Trigo-Rodríguez, E. Dotto, A. Lucchetti, M. Pajola, S. Ieva, and P. Michel. Shape Modeling of Dimorphos for the Double Asteroid Redirection Test (DART). *Planet. Sci. J.*, 3(9):207, September 2022.
- [75] F. Scholten, K. Gwinner, T. Roatsch, K.-D. Matz, M. Wählisch, B. Giese, J. Oberst, R. Jaumann, and G. Neukum. Mars Express HRSC Data Processing – Methods and Operational Aspects. *Photogramm Eng Remote Sensing*, 71(10):1143–1152, October 2005.
- [76] C. C. Paige and M. A. Saunders. LSQR: An Algorithm for Sparse Linear Equations and Sparse Least Squares. *ACM Trans. Math. Softw.*, 8(1):43–71, March 1982.
- [77] J. P. Lewis. Fast Normalized Cross-Correlation. *Ind. Light Magic*, October 2001.
- [78] L. Di Stefano, S. Mattoccia, and F. Tombari. ZNCC-based template matching using bounded partial correlation. *Pattern Recognition Letters*, 26(14):2129–2134, October 2005.
- [79] J.-C. Yoo and T. H. Han. Fast Normalized Cross-Correlation. *Circuits Syst Signal Process*, 28(6):819–843, December 2009.
- [80] M. Hohenwarter. *GeoGebra - ein Softwaresystem für dynamische Geometrie und Algebra der Ebene*. PhD thesis, 2002.
- [81] JGraph. diagrams.net, draw.io, October 2022.

- [82] C. R. Harris, K. J. Millman, S. J. van der Walt, R. Gommers, P. Virtanen, D. Cournapeau, E. Wieser, J. Taylor, S. Berg, N. J. Smith, R. Kern, M. Picus, S. Hoyer, M. H. van Kerkwijk, M. Brett, A. Haldane, J. F. del Río, M. Wiebe, P. Peterson, P. Gérard-Marchant, K. Sheppard, T. Reddy, W. Weckesser, H. Abbasi, C. Gohlke, and T. E. Oliphant. Array programming with NumPy. *Nature*, 585(7825):357–362, September 2020.
- [83] A. M. Annex, B. Pearson, B. Seignovert, B. T. Carcich, H. Eichhorn, J. A. Mapel, J. L. F. von Forstner, J. McAuliffe, J. D. del Rio, K. L. Berry, K.-M. Aye, M. Stefko, M. de Val-Borro, S. Kulumani, and S. Murakami. SpiceyPy: a Pythonic Wrapper for the SPICE Toolkit. *Journal of Open Source Software*, 5(46):2050, February 2020.
- [84] J. D. Hunter. Matplotlib: A 2D Graphics Environment. *Computing in Science Engineering*, 9(3):90–95, May 2007.
- [85] W. McKinney. Data Structures for Statistical Computing in Python. *Proceedings of the 9th Python in Science Conference*, pages 56–61, 2010.
- [86] The pandas development team. pandas-dev/pandas: Pandas, November 2022.
- [87] The Astropy Collaboration, A. M. Price-Whelan, B. M. Sipócz, H. M. Günther, P. L. Lim, S. M. Crawford, S. Conseil, D. L. Shupe, M. W. Craig, N. Dencheva, A. Ginsburg, J. T. VanderPlas, L. D. Bradley, D. Pérez-Suárez, M. de Val-Borro, T. L. Aldcroft, K. L. Cruz, T. P. Robitaille, E. J. Tollerud, C. Ardelean, T. Babej, M. Bachetti, A. V. Bakanov, S. P. Bamford, G. Barentsen, P. Barmby, A. Baumbach, K. L. Berry, F. Biscani, M. Boquien, K. A. Bostroem, L. G. Bouma, G. B. Brammer, E. M. Bray, H. Breytenbach, H. Buddelmeijer, D. J. Burke, G. Calderone, J. L. Cano Rodríguez, M. Cara, J. V. M. Cardoso, S. Cheedella, Y. Copin, D. Crichton, D. DÁvella, C. Deil, É Depagne, J. P. Dietrich, A. Donath, M. Droettboom, N. Earl, T. Erben, S. Fabbro, L. A. Ferreira, T. Finethy, R. T. Fox, L. H. Garrison, S. L. J. Gibbons, D. A. Goldstein, Selena M. Gomez, R. Gommers, J. P. Greco, P. Greenfield, A. M. Groener, F. Grollier, A. Hagen, P. Hirst, D. Homeier, A. J. Horton, G. Hosseinzadeh, L. Hu, J. S. Hunkeler, Ž Ivezić, A. Jain, T. Jenness, G. Kanarek, S. Kendrew, N. S. Kern, W. E. Kerzendorf, A. Khvalko, J. King, D. Kirkby, A. M. Kulkarni, A. Kumar, A. Lee, D. Lenz, S. P. Littlefair, Z. Ma, D. M. Macleod, M. Mastropietro, C. McCully, S. Montagnac, B. M. Morris, M. Mueller, S. J. Mumford, D. Muna, N. A. Murphy, S. Nelson, G. H. Nguyen, J. P. Ninan, M. Nöthe, S. Ogaz, S. Oh, J. K. Parejko, N. Parley, S. Pascual, R. Patil, A. A. Patil, A. L. Plunkett, J. X. Prochaska, T. Rastogi, V. Reddy Janga, J. Sabater, P. Sakurikar, M. Seifert, L. E. Sherbert, H. Sherwood-Taylor, A. Y. Shih, J. Sick, M. T. Silbiger, S. Singanamalla, L. P. Singer, P. H. Sladen, K. A. Sooley, S. Sornarajah, O. Streicher, P. Teuben, S. W.

Thomas, G. R. Tremblay, J. E. H. Turner, V. Terrón, M. H. van Kerkwijk, A. de la Vega, L. L. Watkins, B. A. Weaver, J. B. Whitmore, J. Woillez, and V. Zabalza. The Astropy Project: Building an inclusive, open-science project and status of the v2.0 core package. *AJ*, 156(3):123, August 2018.